Dielectric Metasurfaces for Optical Wavefront Manipulation

Sajan Shrestha

Submitted in partial fulfillment of the

requirements for the degree of

Doctor of Philosophy

in the Graduate School of Arts and Sciences

COLUMBIA UNIVERSITY

2020

Abstract

Dielectric Metasurfaces for Optical Wavefront Manipulation

Sajan Shrestha

Metasurfaces are a novel class of optical devices, made up of an array of subwavelength scatterers that can allow unprecedented control of an optical wavefront. These devices can be fabricated using conventional nano and microfabrication processes en masse and have thin and lightweight form factor making them ideal for use in compact and miniaturized optical systems. In this thesis, I will first introduce the field of metasurfaces with a historical overview of the research and development in this field. Following the introductory section, I will demonstrate a design for broadband infra-red absorber based on the metasurface platform, demonstrating the ability of metasurface to control broad spectrum of light. Subsequently, optical wavefront engineering capability of metasurfaces is displayed by demonstration of multifunctional metasurface devices, including examples of multiwavelength metasurface lenses and holograms. An example of polarization multiplexed metasurface will also be discussed. As an extension of multiwavelength metasurface lens, a framework for correcting chromatic dispersion inherent in metasurface is presented. I will then demonstrate a strategy to design metalenses with broadband achromatic aberration correction for imaging applications and discuss fundamentals limitations on the extent of chromatic correction that can be achieved. This will lead to a section on multi-element metasurface design for correcting monochromatic aberration in addition to chromatic aberration for compact imaging systems. Finally, I will conclude the thesis with an outlook that points to application areas where metasurfaces, with their thin and light form factor are ideal alternative to replace many conventional optical devices.

Table of Content

List of Figures

Acknowledgement

First, I'd like to thank Prof. Nanfang Yu for the opportunity to be part of his group and conduct meaningful research for the last 5 years. He has been a great teacher and a role model. His curiosity and enthusiasm for science has been inspiring. I'm very grateful for his enthusiastic support and for giving me the freedom to pursue my own research ideas. He has always made himself available for mentoring and has created an environment that encourages his students to pursue challenging research ideas and to think out of the box. This has had a significant impact on my development as a scientist.

I'd like to thank Prof. Lipson, Prof. Gaeta, Prof. Zheng and Prof. Garcia for agreeing to be part of my defense committee and for taking the time out of their busy schedule to provide meaningful suggestions and feedback on my research.

I'd also like to thank Dr. Ming Lu and Dr. Aaron Stein from the Brookhaven National Laboratory (BNL) who have passed on their immense knowledge of nanofabrication processes to me and my colleagues and have been valuable resources and collaborators in our projects.

I have thoroughly enjoyed my time in this research group and the company of my colleagues. They have all been very kind and welcoming in sharing their thoughts and ideas. I'd especially like to thank Adam with whom I have had the pleasure of having countless stimulating discussions. Together we have shared the pains of making the long trips to brookhaven, staying up late inside the cleanroom and the overnight stays at their dorms. But I'll always remember the long trips back where we would bounce ideas of each other, some of which directly led to some of our most meaningful works. He has been a great colleague and I've learnt a great deal from him. I'd like to thank Myoung, Zhaoyi and Nan who were the first members of our group and have played a crucial role in establishing our lab and leading us with some really inspiring research. I'd also like

to thank Jyoti, Cheng-Chia, Michael, Stephanie, Gouzhen, Heqing and Xiaoyan who have been wonderful colleagues and friends.

Finally, I'd like to thank my parents for their unwavering support and belief in me. Being so far away must have been very difficult for them, but they have always made their presence felt. I would not be where I am today without the dedication and effort.

Chapter 1: Introduction

Metasurfaces are optically thin 2D surfaces composed of arrays of subwavelength scatterers that can be used to modify scalar and vector properties of incident electromagnetic field. Each unit of a metasurface, which we will call a meta-unit, interacts with an incoming optical wavefront and rescatters the light either resonantly or non-resonantly and can modify phase, polarization, spectrum etc. of the incoming wavefront. Various optical functionalities such as gratings, lenses, holograms, and absorbers can then be realized by carefully arranging meta-units with varying optical responses in periodic or aperiodic arrays. Further, a single metasurface can be designed to perform multiple optical functionality given the unprecedented level of control over the incident light, which most conventional optical elements cannot offer. Combined with its thin and light form factor and advances in CMOS nanofabrication techniques for mass manufacturing, metasurface platform is an ideal alternative to replace many conventional optical devices where reduction in size and weight are extremely important. It is for these reasons, in the recent years, this field has gathered much attention and several important advances in the area has been made due to its potential impact in real world applications.

1.1 Historical Development

The working principle of metasurfaces in the simplest form can be understood by the Huygens-Fresnel [1] principle, which states that every point in the wavefront is itself a source for spherical wavelets whose sum recreates the new wavefront. Metasurfaces are optical interfaces, which work by introducing spatially-varying phase delays to the optical wavefront. Such phase shifts are imparted by individual elements with subwavelength spacing that comprise a metasurface. The subwavelength spacing suppresses power coupling into unwanted diffraction channels and is a

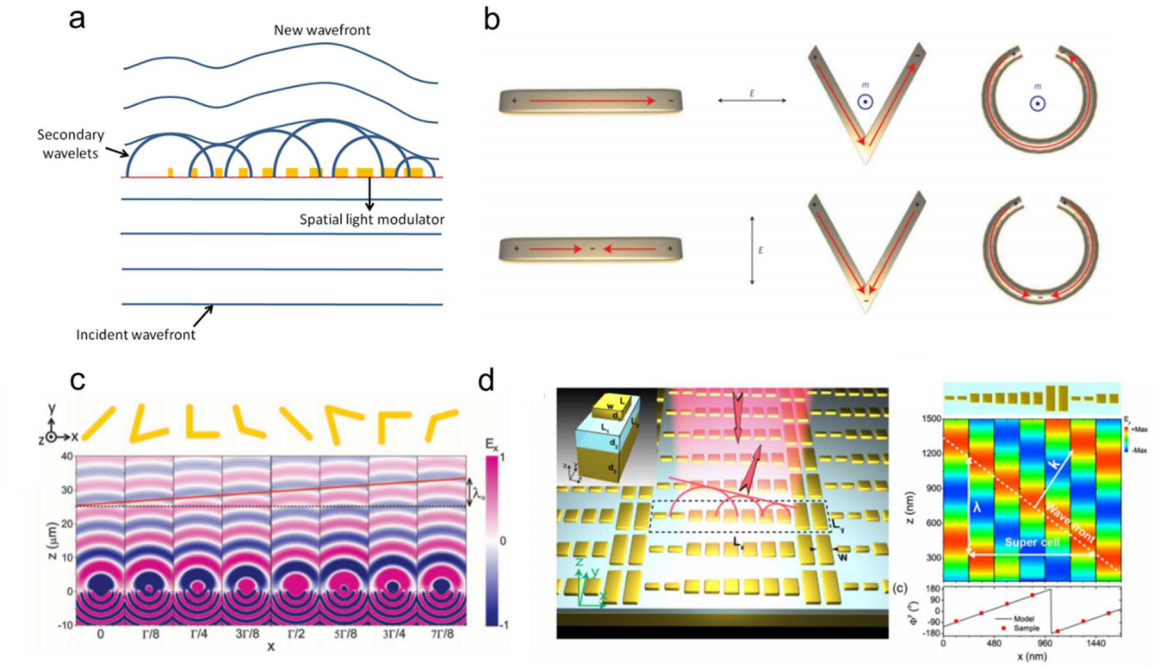

Figure 1.1: Metasurface operating principle. (a) Huygens-Fresnel principle. Input wavefront spatially modulated by subwavelength scatterers producing secondary wavefronts that form the new wavefront. (b) Different geometries of plasmonic antennas. Electric (red) and magnetic (blue) dipole moments produced due to the charge distribution of the plasmonic mode under incident electric field (adapted from [3]). (c) Anomalous refraction due to plasmonic metasurface (adapter from [2]). (d) Beam deflector based on plasmonic phased gradient surface (adapted from [22])

feature that differentiates metasurfaces from diffractive optical elements (DOEs). We can imagine these elements as the source of spherical wavelets each programmed with a specific temporal delay to engineer the incoming optical wavefront. Figure 1.1a shows a depiction of a metasurface interacting with a planewave and modifying the exiting wavefront. This concept is not a novel one and in fact one can argue that the origins of the optical metasurface can be found in the development of microwave antennas decades ago. The design principle of early plasmonics based metasurfaces [2,3] have much in common with their counterparts in the microwave community such as the Yagi-Uda [4,5] antenna and phased array antennas [6–8].

Modern micro and nanofabrication methods have made it possible to transfer the phased array concept from the microwave to the optical frequencies. Early examples of metasurfaces at optical frequencies utilized subwavelength thick metallic antennas predominantly based on noble metals [9] and are classed as plasmonic metasurfaces. These ultrathin devices are effectively

subwavelength array of metallic resonators whose response to the electromagnetic field are determined by their material and geometrical properties. When driven under time varying electromagnetic fields, these elements produce electrical and to a lesser extent magnetic polarizability corresponding to resonant modes supported by the structure. These plasmonic resonances can be understood as collective oscillation of conduction electrons in the metallic structure corresponding to the driving electromagnetic field and the restoring force generated due the displacement of these electrons from their equilibrium positions. These resonances display a characteristic π phase excursion over their resonant bandwidth and can have subwavelength localization due the large negative permittivity of the metals [10]. By tailoring the shape of these resonators, it possible to shift its resonance position and achieve different phase delays at the same frequency. Figure 1.1b shows some example geometries of plasmonic antennas and their responses to the driving electric field.

Early works using plasmonic metasurfaces demonstrated anomalous reflection and refraction based on phased gradient plasmonic antennas [2]. Subsequent works [11–16] have utilized similar methodologies to demonstrate metasurfaces with various optical functionalities using different geometries of the plasmonic scatterer. Plasmonic structures that interact with magnetic part of the electromagnetic spectrum have also gained significant interest, in particular split ring resonators [17,18] based metasurfaces. A significant interest in the field of negative index metasurfaces and metamaterials [19,20] are due in part by the accessibility of control of magnetic polarizability of plasmonic scatterers. A more detailed exploration of such devices is beyond the scope of this work. Figure 1.1(c, d) shows examples of plasmonic metasurface based optical elements.

Despite the planar and subwavelength thick form factor of plasmonic metasurfaces, their widespread adoption has failed to materialized due the inherent metallic losses resulting in poor

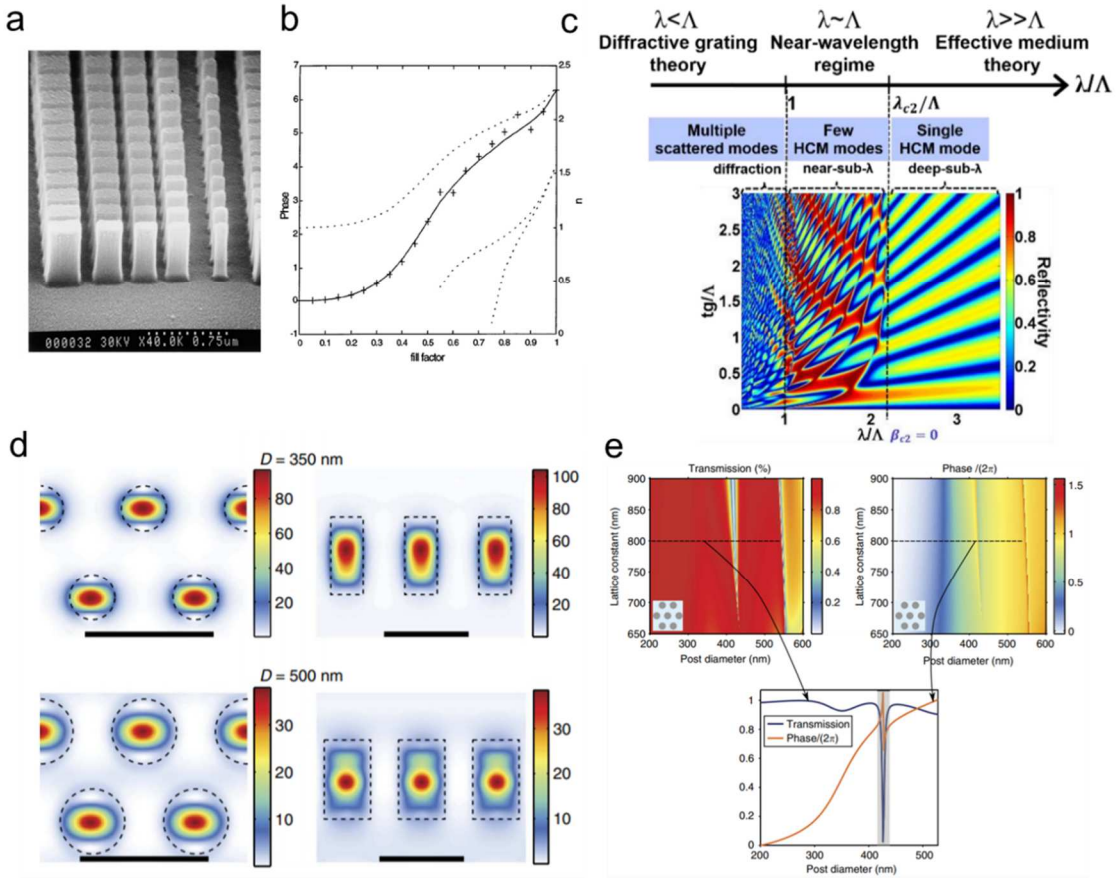

Figure 1.2: Effective medium and high contrast arrays based metasurfaces. (a) Scanning electron micrograph of fabricated TiO2 based binary blazed grating. (b) Phase (crosses and solid line) and effective index (dotted lines) as a function of fill factor (diameter) of TiO2 pillar with square cross-section. For fill factor of less than 50% only single mode is allowed (a,b adapted from [23]). (c) 3 unique operating regimes of metasurfaces as a function of ratio of wavelength to lattice period (adapted from [31]). (d) Magnetic energy density with amorphous silicon nanopillars of different diameters at wavelength of 1550nm. Scale bar: 1μm. (e) Transmission and phase response as a function of post diameter and lattice constant (d,e adapted from [29]).

efficiencies. Recent works [21,22] have demonstrated higher efficiencies using novel plasmonic flatforms but they are limited to devices that work in reflection mode only. This has led the metasurface community to turn to dielectric based meta-units. These metasurfaces are thicker (0.5 to 1 λ) than their plasmonic counterparts and are made up of high index dielectric materials that maybe encapsulated in lower index materials. These high index dielectric materials are generally entirely transparent in the operating range of the metasurface or exhibit very low loss. The individual meta-unit structure is generally single level to ease the fabrication process by adopting binary

lithography masks. Using dielectric materials, recent works have demonstrated metasurfaces with a multitude of optical functionalities with significantly higher efficiencies when compared to similar devices based on plasmonic structures. The following section will highlight these works based on the type of dielectric metasurface they are derived from.

1.2 Types of Dielectric Metasurfaces

Spatially varying phase shift using dielectric scatterers have been realized in different ways. In this section, they are primarily classified by the mechanism by which each element produces such a phase shift.

1.2.1 Effective Medium Theory

This type of metasurface was first demonstrated [23,24] more than two decades ago and was then referred to as blazed binary subwavelength gratings. Early demonstrations of these devices reported larger diffraction efficiencies when compared to conventional grating elements. Composed of TiO2 nanopillars in a subwavelength lattice, each element of the grating operates as single mode waveguide by imposing a structural cutoff on its dimension. By tailoring the waveguide cross-section (or fill fraction), its effective index can be changed as seen in Fig 1.2b. The phase response of each element is then proportional to the propagation phase accumulated as light travels within the pillar with a characteristic waveguide mode index. Thus, nanopillars of different diameters can impart different amount of phase shifts. The polarization independent operation, the nanopillar cross-section must be symmetrical. Asymmetric cross-sections will result in birefringent effective index response and therefore the metasurface will generally not be polarization independent. However, such birefringent response can be leveraged to create geometric phase based metasurfaces, which will be discussed shortly as well as polarization multiplexed metasurfaces [25,26]. This working principle is somewhat analogous to that of a homogenous medium with tailored effective indices based on varying fill fraction provided only a single mode is allowed to propagate within the nanopillar. As such, a simple thin-film interference model can be

used to calculate the transmission and reflection coefficients of a nanopillar given its mode index and thickness to account for complex interactions at the interfaces between the nanopillar and the surrounding. It is reported [27] however, that the blazed binary subwavelength gratings are more efficient than a conventional effective medium based grating with continually varying refractive index due to strong localization of light due to the waveguiding effect in the nanopillars. Such localization is stronger in materials of high index [28–30] due to the better confinement of light inside the waveguides. This is crucial for validity of local phase approximation as strongly confined modes have reduced coupling with their neighbors and therefore their phase response is less sensitive to the lattice period of the metasurface and their neighbors. This results in larger efficiencies for high index contrast dielectric metasurfaces when compared to low index contrast material platforms.

1.2.2 High Contrast Arrays

This type of metasurface is similar to the one discussed above but the nanopillars do not operate as a single mode waveguide and allow for a few high order modes to propagate within them. This results in complex modal interactions at the interface of the nanopillars with its substrates resulting in multiple resonances. Figure 1.2c shows different operating regimes of a periodic dielectric nanopillar array based on the effective wavelength i.e. ratio of operating wavelength to the lattice period. The map shows 3 unique operating regimes [31], where the optical response of such an array displays varying amount of modal interferences. When the operating wavelength is much larger than the lattice period, the response is very similar to effective medium type response discussed above, since only one mode is allowed to propagate. We can therefore observe fabry-perot like response in the reflectance response as a function of effective thickness of the metasurface. The other extreme is the operation in the diffractive regime that is when the wavelength is smaller than the lattice period resulting in propagation of large number of modes within the nanopillars and scattering into multiple diffraction orders. The third region of operation lies between the ones discussion above, where only a few waveguides mode is allowed to propagate resulting in resonant responses as seen in the reflectance map. The resonant effects

allow for much sharper 0 to 2π phase recursion [28,29] for a lower thickness of nanopillars when compared to the effective medium response discussed above. The resulting field distribution due to modal interactions are still highly confined within the high index material allowing for the use of local phase approximation as seen in Fig. 1.2c [29], where magnetic energy density within nanopillars of two different diameters are shown. Appropriate choice of thickness and lattice period can be chosen for a design wavelength to populate a library with very high transmission (or reflectance) and 0 to 2π phase shift by varying nanopillar diameter as seen in Fig 1.2d [29]. Such libraries are generated using computation electromagnetics routines such as rigorous coupled mode theory (RCWA) or finite difference time domain (FDTD) solver simulating each individual nanopillar with periodic boundary condition.

High contrast arrays have been recently used to demonstrate highly efficient optical devices including subwavelength thick lenses in the visible [32–34] and near-infrared [29], large angle deflectors [35] and holograms [36]. Efficiencies of over 80% have been routinely reported for different devices using this platform.

1.2.3 Geometric Phase Based Metasurface

Another mechanism of introducing spatially varying phase delay utilizes the so called "Pancharatnam-Berry" [37–39] phase. The phase shift is the result of the rotation of the polarization state around a closed loop on the Poincarè sphere. The phase shift between the initial and the final state is equal to half the solid angle traced out by the closed path. Generally, the polarization state of the incident light is inverted with circularly polarized incident light changing handedness in transmission and keeping the same handedness when reflecting off of a geometric phase metasurface. This phase shift is often known as geometric phase as the phase shift is induced by varying a geometric parameter, in particular the orientation of a birefringent scatterers fast (or slow) axis relative a predefined axis. This type of phase shift does not change significantly with wavelength, which allows for broadband performance. Metasurfaces based on geometric phase have been used to demonstrate multiple optical functionalities using plasmonic antennas [21,40].

Here we discuss the use of dielectric elements for implementing geometric phase based metasurfaces for improved efficiency.

As mentioned earlier, geometric phase shift is implemented using birefringent elements. The simplest form of dielectric element is a high index rectangular nanopillar, which operates much in the same way as polarization independent nanopillars we have discussed in the previous section but with different effective mode index along its two axes. Light polarized along the extraordinary and ordinary axes of these nanopillars accumulate different phase delay. Therefore, we can realize an optical retarder by appropriately choosing a thickness of such a birefringent element. More rigorously, we can quantify how an input state is transformed by the action of such an element using the Jones matrix [41] formalism as

$$|\psi_o\rangle = R(-\alpha)\begin{bmatrix} A_o e^{ik_o n_o H} & 0 \\ 0 & A_e e^{ik_e n_e H} \end{bmatrix} R(\alpha)|\psi_i\rangle \qquad (1.1)$$

where ψ_i and ψ_o are input and output polarization jones vector in x-y basis. $R(\alpha)$ is a 2 by 2 rotation operator that takes a unit vector it by α. The action of the birefringent element is represented by the 2 by 2 matrix whose main diagonal represents its amplitude and phase response to light polarized along the ordinary (o) and extraordinary (e) axes. The phase accumulated is simple the propagation phase accrued along the element thickness (H). As described before, the phase shift is experienced by the portion of light that is converted to the polarization orthogonal to the incident light. If we consider starting with right hand circularly polarized incident light then the response of the element can be seen if we detect only left hand circular polarized light at the output using a polarization filter. The signal detected at the output can be derived as [42]

$$S = \langle -|\Gamma(-\alpha)M\Gamma(\alpha)|+\rangle = i\sin\left(\frac{k_0 H(n_o - n_e)}{2}\right)\exp\left(i\left(\frac{k_0 H(n_o + n_e)}{2} + 2\alpha\right)\right) \qquad (1.2)$$

where $|+\rangle$ and $|-\rangle$ represent right and left circularly polarization jones vector. The amplitude response then is determined by the argument of the sine term, which is the degree of birefringence of the element and the phase is determined by the average propagation phase of light within the nanopillar and geometric term 2α determined by its orientation angle. A phase shift of -2α is imparted if the handedness of the incident polarization is flipped. For maximum conversion

efficiency, the obvious choice of degree of birefringence is setting $k_0 H(n_o - n_e) = \pi$, which represents a half-wave plate retarder. However, in general any arbitrary value can be chosen which represents partial conversion of polarization state and therefore a lower amplitude response. Figure 1.3a shows an array of nanopillars with varying rectangular cross-sections representing degree of structural birefringence and orientation angles which represents the geometric phase. From Fig. 1.3b we can see that degree of birefringence controls the latitude and the orientation angle controls the longitude of the path polarization state of light take as it travels from one pole to the other for circularly polarized incident light. This geometric control of the dielectric nanopillar structure allows for a method to simultaneously impart amplitude and phase response to a circularly polarized light. Such a metasurface has been recently [42] used to demonstrate highly efficient phase and amplitude holograms that can produce very high-fidelity reconstruction of desired electromagnetic field distributions. This degree of freedom can be transformed to impose two completely independent spatially varying phase mask [25,43] to two orthogonal polarization states of light.

It is clear that geometric phase based metasurface have additional degree of control over the incident light when compared to the polarization independent high contrast arrays and have been used to successfully demonstrate highly efficient optical devices [32,36,44]. But such additional degree of control comes at the cost its polarization dependent behavior and addition of analyzing polarizers and waveplates in the optical setups and therefore taken into considering when using this type of metasurfaces.

1.2.4 Huygens Metasurface

Huygens metasurfaces are physically realizable form of Huygens surfaces [45] which is composed of ideal point sources of light with radiation pattern resembling crossed electric and magnetic dipoles. Electric dipoles radiate symmetrically on either side of the surface that is to say that the sign of the electric field is same on both sides while the magnetic dipoles radiate with electric field with opposite side on either side of the surface. This results in cancellation of reflection of the incident plane wave exciting a Huygens surface due the interference of electric fields of

opposite signs resulting in unity transmission when the strengths of electric and magnetic dipole resonance are equal and no other losses mechanism exists [46]. Figure 1.3(c,d) shows amplitude and phase response when electric and magnetic dipole resonance of equal strengths are spectrally aligned. Without any additional loss channel, unity transmission is observed across the aligned dipole resonances and a phase excursion of 2π is also observed instead of the usual π shift across the resonance. The 2π phase shift is crucial because it allows such a surface to impart spatially varying phase by tuning the geometry of the elements producing such resonances. Such surfaces have been realized in the microwave frequencies [47] and have also been demonstrated in optical frequencies using resonant plasmonic elements [48] albeit with reduced efficiencies due to the intrinsic losses of metals. High index dielectric nanoresonators can be geometrically tuned to host spectrally aligned electric and magnetic dipole resonances and behave as ideal Huygens surfaces without any intrinsic material loss channels. Figure 1.3e shows electric and magnetic field distribution for an electric and magnetic modes hosted in a dielectric nanodisc that satisfies the Huygens condition. Experimental demonstration of such a metasurface has been reported [46] recently in the near-infrared. Spatially varying phase masks can be implemented by tuning the nanodisc diameters, which allows for realizing highly efficient optical devices. An additional advantage of dielectric Huygens metasurfaces over the high contrast arrays discussed is that the nanoresonators used in the former can be of smaller thicknesses since the phase response of Huygens metasurfaces is entirely due to resonant effects. This allows for relaxation of fabrication requirements. However, since due to the reliance on resonant effects, this type of metasurface is very sensitive to nearest-neighbor coupling effects. Therefore, sharp phase gradients are difficult to implement since that would require neighbors with marked geometric differences. In addition to this, slight deviation from the reference angle of incidence shifts the resonance and destroys the unity transmission property. This can be observed in Fig. 1.3f. Hence, this platform has not been widely adopted compared to the high contrast array, which has been the primary form of dielectric metasurface implemented.

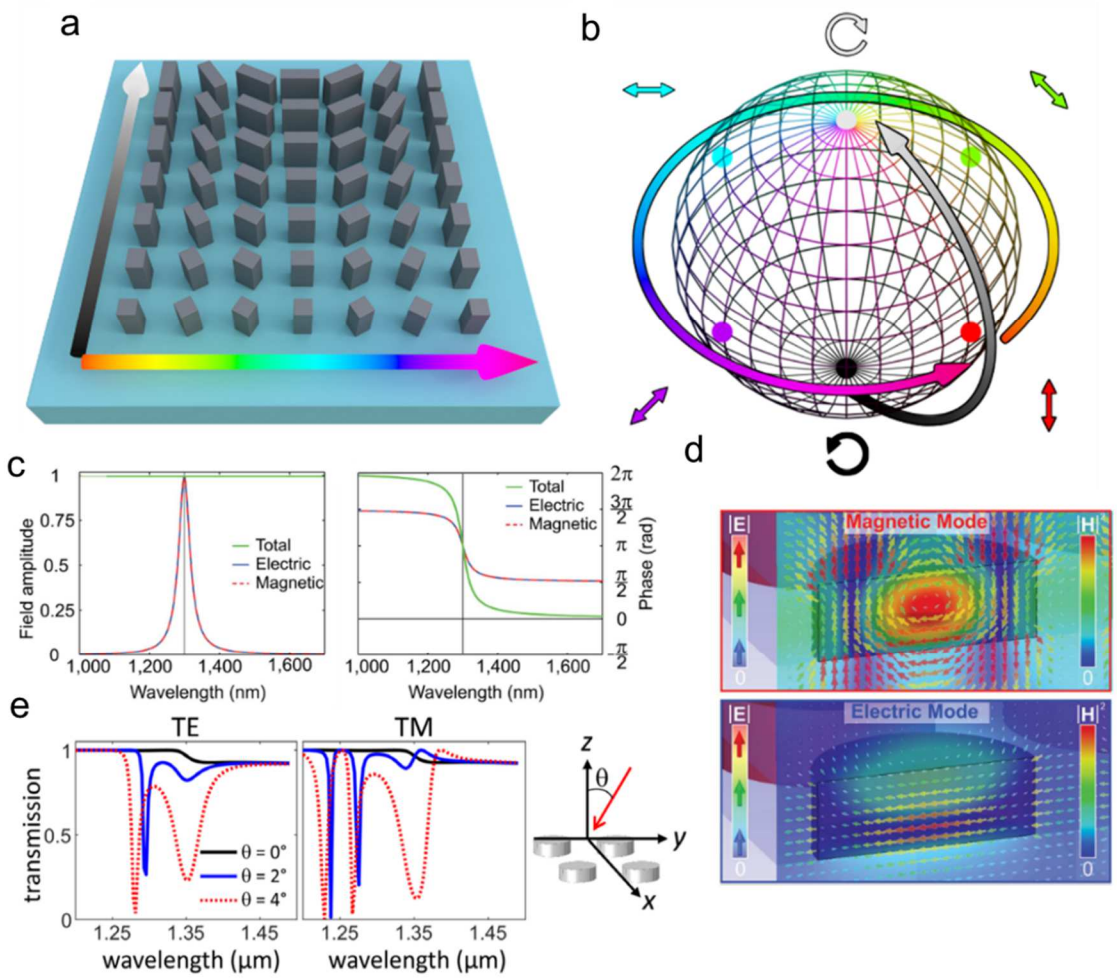

Figure 1.3: Geometric and Huygens metasurfaces. (a) Birefringent nanopillar for implementing geometric metasurfaces. Degree of birefringence (amplitude response) shown by black to white arrow and orientation angle (phase response) shown by the coloured arrow. (b) Mapping of responses from (a) to the Poincarè sphere. Degree of birefringence maps to latitude and orientation angle maps to longitude (adapted from [42]). (c) Amplitude and phase response of ideal Huygens source showing unity transmission and 2π phase excursion across spectrally aligned electric and magnetic dipole resonances. (d) Electric field (arrows) and magnetic field (colormap) distribution for magnetic and electric mode in a nanodisc resonator (c,d adapted from [46]). (e) Deviation from ideal performance of a dielectric Huygens metasurface for off normal incidence (adapted from [34]).

1.3 Thesis outline

The following chapters will discuss design methodology of meta-unit elements to achieve various optical functionality. In particular, chapter 2 will demonstrate a metasurface device

demonstrating broadband absorption of optical wavefront using novel material platform. Chapter 3 will discuss multi-wavelength control of light using multiplexing techniques using dielectric materials. Chapter 4 then demonstrates the concept of structural engineering of meta-units for dispersion control allowing a unique solution to chromatic aberration correction in metalenses. Approaches and applications of multi-element metasurfaces are then discussed in chapter 5 with a demonstration of a metalens triplet correcting for monochromatic and chromatic aberration simultaneously. Finally, I conclude this thesis with the summary of my research and a short discussion on future outlook of adoption of metasurface based optical devices for real world application.

Chapter 2: Broadband Metasurfaces

The material in this chapter is reproduced from [49].

Ability to control broad spectrum of light is crucial for many applications. One such application is that of electromagnetic absorbers, which find use in elements like thermal emitters and sensors. In this chapter, ability of a single layer metasurface to interact with broadband light is demonstrated with an infrared absorber with absorption bandwidth spanning more than an octave.

2.1 Broadband Metasurface Absorber

Metamaterials have been designed to achieve a wide range of functionalities. Metamaterial absorbers are of particular interest for various applications such as infrared detectors, emissivity coatings, and photovoltaic cells. Various metamaterial platforms have been demonstrated to achieve perfect absorption and several attempts have been made to extend the absorption bandwidth of such devices. We demonstrate a broadband infrared absorber using an asymmetric Fabry−Perot cavity consisting of a monolithically fabricated two-layer metasurface. Superoctave optical absorption is achieved by tailoring the structure of the metasurface layers and the thickness of the cavity. The device yields absorptance of over 80% from λ = 4−16 μm, while maintaining the performance over a wide range of incident angles. In contrast to most metamaterial absorbers, our metasurface layers are made of customized indium tin oxide (ITO), conferring the advantage of CMOS compatibility compared to previous approaches using noble metals.

Metamaterials and metasurfaces have generated great interest as tools for studying novel electromagnetic phenomena and have been used to demonstrate a wide range of functionalities, [50] such as wavefront engineering, [51–53] optical modulation, [54,55] and perfect absorption. Metamaterial-based electromagnetic absorbers in particular have applications in solar

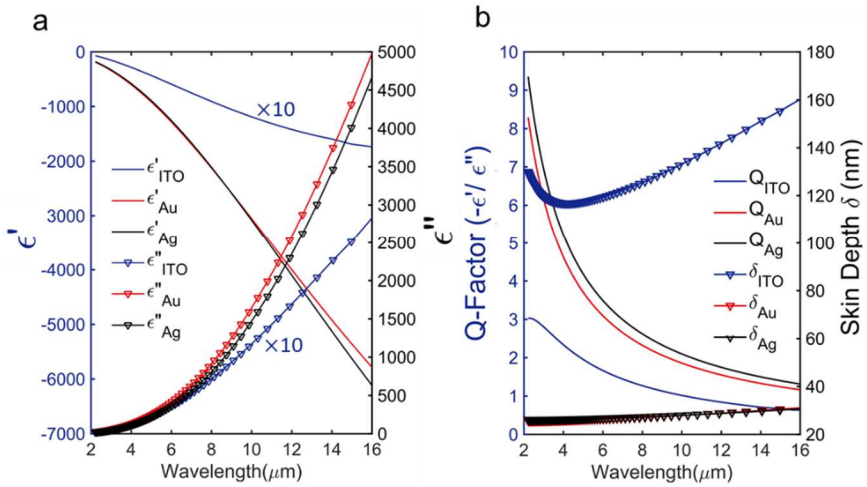

Figure 2.1: Optical properties of ITO compared to Au and Ag. (a) Real and Imaginary parts of permittivities (b) Quality factor and Skin depth comparison between tailored ITO material and noble metals (Au,Ag).

energy harvesting, [56–58] thermal imaging and sensing, [59–62] and thermal emissivity control. [63–66] Toward these ends, metamaterial platforms have been pursued to achieve near perfect absorbers in the solar spectrum, [57,67–69] as well as in the infrared [70,71] and terahertz [72] spectral ranges. Most metamaterial absorbers utilize inherent losses in plasmonic [73] nanostructures to produce large absorption. Plasmonic scatterers embedded in dielectric layers have been reported [74,75] to achieve large absorption enhancement by trapping incident solar radiation. Similarly, coupling light into surface plasmon polaritons in structured metallic films is known to induce large absorption. [76] Tapering a stack of alternative metal and dielectric films produces broadband absorption via excitation of slow light modes. [77,78] Strong local field enhancement in subwavelength plasmonic nanoresonators with tailored electric and magnetic resonances is the most widely used approach to enhance absorption and even achieve near-unity absorption. This platform allows for great flexibility in realizing polarization and incidence angle insensitive absorbers for different wavelength ranges. [70,71,79–82]

While various perfect absorbers utilizing plasmonic nanoresonators have been demonstrated, it is difficult to maintain large absorption over a broad wavelength range due to the limited bandwidth of plasmonic resonances. Multiband absorption [83,84] has been demonstrated

by combining different types of plasmonic resonators within a subwavelength unit cell, but the overall bandwidth of absorption is limited by the ability to pack different resonators within a subwavelength period. Multilayered structures[36,37] have been proposed as a solution to this problem, but fabrication of such structures is tedious and designs that can be realized with simpler nanofabrication methods are generally preferred. To that end, a planar structured plasmonic surface optimized by a genetic algorithm to overlap multiple resonances over a chosen wavelength range has been demonstrated [87] to achieve near-unity absorption over an octave bandwidth and maintained over a wide range of incidence angles.

We report here an alternative strategy that, from first principles, can achieve large absorbance over a superoctave bandwidth by replacing metallic plasmonic elements with nanostructures made of an engineered indium tin oxide (ITO). This material platform is chosen for its tunability of optical response and CMOS compatibility. Our broadband absorbers consist of two Babinet-complementary metasurface layers made of ITO and separated by a dielectric spacer. Each metasurface layer acts as a mirror of a Fabry−Perot cavity. By designing the spectral phase response of the two mirrors in conjunction with the thickness of the cavity, we designed and experimentally demonstrated super broadband absorbers working over more than one octave bandwidth in the midinfrared. ITO has been proposed as an alternative plasmonic material in the near-infrared [9] for various applications [88–90] and recently in the mid-infrared band as well. By varying the growth and annealing conditions, its optical properties can be tuned to achieve a negative real part (ϵ') and a small imaginary part (ϵ'') of the dielectric permittivity in the infrared wavelengths. [91,92] The ratio of the real to the imaginary part of dielectric permittivity, which is often used as a figure of merit to determine the quality factor of localized surface plasmon resonance (LSPR) in plasmonic materials, is much larger for noble metals than that for ITO [9] in the near-infrared, and remains slightly greater than that of ITO in the mid-infrared. This leads to a weaker but broader extinction spectrum for plasmonic scatterers made of ITO as compared to those made of noble metals. Figure 2.1(a,b) shows a comparison of the real and imaginary parts of dielectric permittivity of noble metals (Au and Ag) and the tailored ITO material we used in our metasurfaces. While both the real and imaginary parts of the permittivity are significantly larger for

noble metals, the LSPR quality factor of the noble metals is only larger than that of ITO by a factor of ~2.

Another key material property that must be considered is the optical loss. The plasmonic losses accrued depend on the extent of penetration of light into a material, which is quantified by the skin depth, $\delta \equiv \frac{\lambda}{2\pi \mathrm{Im}[n]}$, where n is the complex refractive index. The skin depth of the noble metals is compared with that of our ITO material in Fig. 2.1b, which shows that electromagnetic waves can penetrate through more than 100 nm of our ITO material but are limited to less than 30

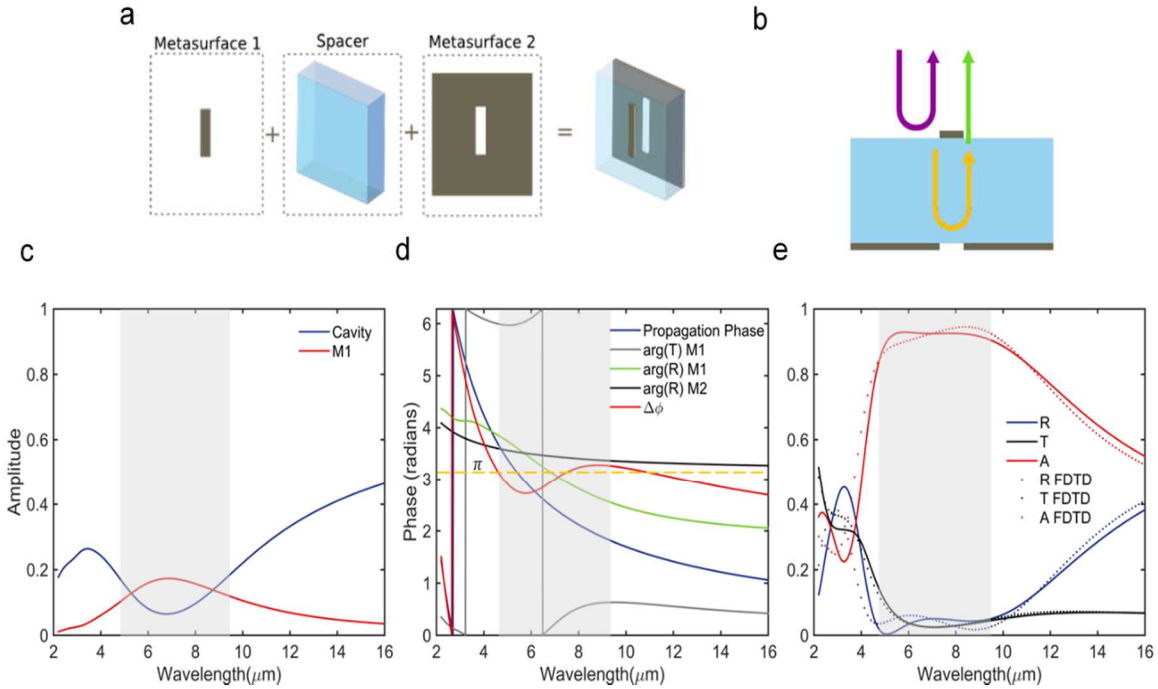

Figure 2.2: Modelling the metasurface as an asymmetric Fabry-Perot cavity. (a) The metasurface consists of a 2D subwavelength periodic array of lossy rod antennas separated from its Babinet inverse by a dielectric spacer. (b) Overall reflection is approximately the sum of the direct reflection from M1 and the reflection of light during a single round-trip pass through the FP cavity. (c) Amplitudes of the two reflected components as illustrated in (b). The amplitudes are comparable within the shaded wavelength range. (d) The phase difference, Δϕ, between the two reflected components as illustrated in (b). It is roughly π within the shaded wavelength range. (e) Comparison of reflectance, transmittance and absorptance spectra predicted by the analytical model for the asymmetric Fabry-Perot cavity (Eqs. 2.1-2.3) and those by FDTD simulations. Shaded region represents the wavelength range over which high absorption is achieved due to a strong destructive interference between the two reflected components.

nm in the noble metals. Therefore, despite having much smaller ϵ″, due to the larger skin depth, ITO causes more absorption losses of infrared light, while the noble metals reflect most of the

incident infrared light. Thus, by tailoring the growth parameters, [93] in particular, balancing the values of ϵ' and ϵ'', we can realize a material platform that can produce broad resonances with large absorption.

The ITO thin films were deposited using RF magnetron sputtering in a Denton Discovery 18 confocal-target system, with an ITO (99.99% purity) target placed in argon atmosphere at room temperature. [94] The base pressure was 1.0 × 10−7 Torr and the argon gas flow was kept at 12 sccm. The sputtering power was fixed at 200 W, and the thickness of the deposited ITO thin films was measured to be 100 nm. We performed postdeposition annealing of ITO in N2 at 250°C for 60 min to tune the optical dispersion of ITO, which was then characterized using a mid-infrared ellipsometer (see Supplementary section 2.1 for details). The tunability of ITO optical dispersion with respect to sputtering power and post annealing conditions is shown in Supplementary section 2.2A.

Broadband absorption in ITO has been reported before [95] by utilizing enhanced light matter interactions at epsilon-near-zero (ENZ) wavelengths for a stack of thin films of ITO, each with a different ENZ wavelength. [96] However, this requires excitation in an attenuated total reflection configuration and the absorption occurs only around the ENZ wavelengths (1.3− 1.9 μm). In contrast, we use a coating of ITO operating well above the ENZ wavelength, which therefore does not rely on the field enhancement associated with the ENZ condition and hence can achieve enhanced absorption over a significantly larger wavelength range by utilizing a structured ITO metasurface.

In this paper, we report a super broadband metamaterial absorber with absorptance values of over 75% spanning from λ = 4 to 16 μm. We achieve large absorbance across the entire band using a resonant cavity based on a dual-layer metasurface. Two lossy ITO metasurface mirrors enclose a dielectric spacer forming a Fabry−Perot (FP) cavity. By tailoring the electromagnetic

response of the metasurface mirrors and thickness of the cavity, we produce cavity resonances that satisfy the destructive interference condition for reflected waves over a large bandwidth.

Figure 2.2a depicts three layers that form the asymmetric FP cavity. Metasurface 1 (M1) is a two-dimensional array of rod antennas; its Babinet inverse, Metasurface 2 (M2) forms the second mirror. Together they enclose a dielectric spacer of thickness d and effective index n_{eff}. Each meta-unit that makes up these metasurfaces are deeply subwavelength and optically thin. Additionally, the two metasurface layers are assumed to operate independently (i.e., there is negligible near-field coupling due to the spacing between them). Hence, we can treat these layers as optically thin interfaces with tailored optical responses. The reflection and transmission coefficients of the resulting cavity are respectively given by [97]

$$r = \frac{r_1 + (t_1 t_1' - r_1 r_1') r_2' e^{-i\delta}}{1 - r_1' r_2' e^{-i\delta}} \tag{2.1}$$

and

$$t = \frac{t_1 t_2' e^{-\frac{i\delta}{2}}}{1 - r_1' r_2' e^{-i\delta}} \ , \tag{2.2}$$

where $\delta = \frac{4\pi n_{eff} d cos\theta}{\lambda}$, $r_1(t_1)$ and $r_2(t_2)$) are the reflection (transmission) coefficients of M1 and M2, respectively. The primes represent the coefficients when the direction of propagation is reversed. Overall absorptance,

$$\mathrm{A} = 1 - |t|^2 - |r|^2 \tag{2.3}$$

can be calculated by obtaining properties of the constituent layers by using finite-difference time-domain (FDTD) simulations. A similar treatment of metamaterials as an assembly of multiple metasurfaces has been reported previously. [98]

The designs of the metasurfaces are aimed at suppressing overall reflection and transmission. Direct reflection from M1 and the reflection from the FP cavity represent the two channels contributing to the overall metamaterial reflection as shown in Fig. 2.2b. We employ a basic design principle aiming to maximize the bandwidth over which the destructive interference

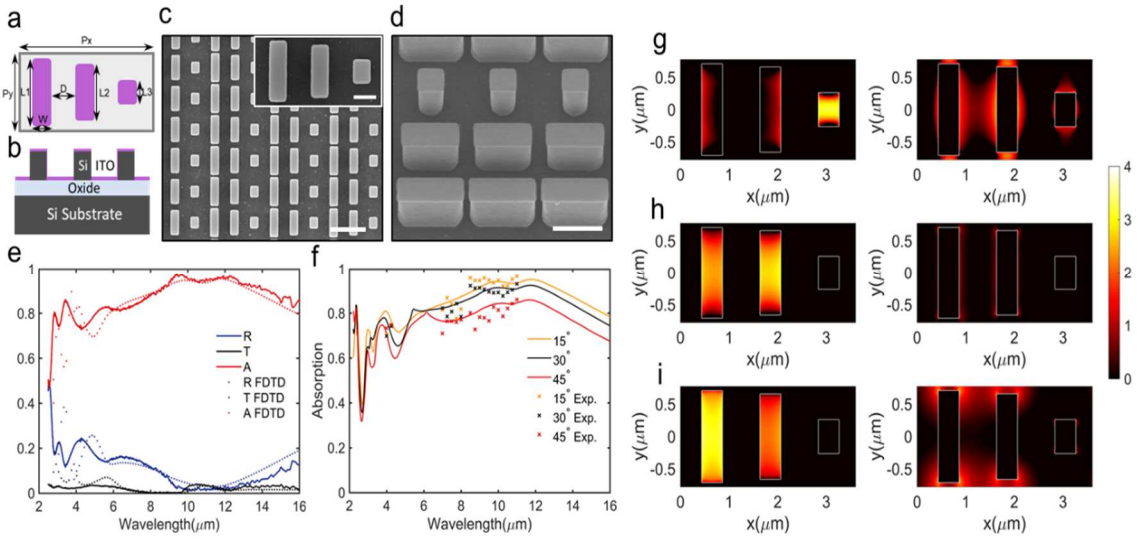

Figure 2.3: Design and performance of a broadband polarization-dependent infrared metasurface absorber. (a) Top view of the unit cell of the metasurface. (b) Cross-sectional view of the unit cell of the metasurface. (c) SEM image of a fabricated device (Scale bar: 2000 nm). Inset: one-unit cell (scale bar: 500 nm). (d) SEM image taken at an oblique angle of the fabricated device (scale bar: 1000 nm). (e) Measured and simulated reflection, transmission, and absorption spectra of the metasurface absorber. (f) Simulated and measured absorption spectra at different incident angles. (g−i) Spatial distributions of absorbed optical power on the plane of M1 (left) and M2 (right) at λ = 4, 6.25, and 10 μm, respectively.

condition occurs: when the electromagnetic waves corresponding to the two paths are equal in amplitude and out of phase. We calculate the absorption spectrum of a metasurface consisting of an array of ITO rod antennas (length of 1400 nm, width of 400 nm, and thickness of 100 nm) as M1, its Babinet inverse as M2, and a dielectric spacer (thickness of 1400 nm and refractive index of 1) using our model and compare it with FDTD simulation of the same structure. The exclusion of loss in the dielectric spacer (which is present in the final device to be shown later) is found to make little difference in the analytically calculated spectrum, which demonstrates that the primary loss mechanism is due to M1 and M2. The transmittance through the device is small because M2 acts as an excellent mirror. Figure 2.2c shows analytically calculated amplitudes of the direct reflection from M1 and the reflection from the FP cavity (assuming a single round-trip pass through the cavity). Figure 2.2d shows the phase difference between these two components, given by $\Delta\phi = \arg(r1) - [\arg(t1) + 2\pi n_{eff} \mathrm{d}/\lambda + \arg(r2)]$.

The highlighted region in Fig. 2.2c represents the wavelength range where the amplitudes of the two reflected components are comparable, while their phase difference is close to π. This will lead to strong destructive interference at the reflection port and, as a result, large absorption over the corresponding bandwidth. This is confirmed by our analytical model (eqs 2.1−2.3) and FDTD simulations, which are presented in Fig. 2.2e. The model successfully reproduces reflection, transmission, and absorption spectra obtained from FDTD simulations, of the combined metamaterial, validating the description of the device as an asymmetrical FP cavity.

We apply our understanding of the broadband absorption process to design a device with large absorptance spanning multiple octaves in the mid-infrared. We overlap resonances of multiple ITO antennas of different lengths, each antenna supporting a different resonance wavelength, and a correspondingly different wavelength range over which the destructive interference condition can be satisfied. Figure 2.3a shows a single period of the unit cell of a polarization dependent absorber with all the design parameters. This design is based on three antennas of different lengths and is a simple extension of the one based on a single antenna discussed above. The cross-section of the unit cell illustrated in Fig. 2.3b shows that M1 and M2 are separated by an array of silicon nanopillars with subwavelength periodicity, acting as the dielectric spacer. The metasurface is fabricated on a Silicon on Insulator (SOI) chip, which has a 2.2 μm buried oxide layer and a 1.4 μm device layer. This design allows us to fabricate both the ITO rod antenna array (M1) and its Babinet inverse (M2) with a single lithographic and etch step followed by deposition of a thin film of ITO and post deposition annealing processes (see Methods, Nanofabrication). While the array of silicon nanopillars is an unconventional choice for a spacer, it can be modeled as a dielectric slab with an effective index due to the deep subwavelength size of the constituent elements. While not shown in Fig. 2.3b, the side walls of the pillars are covered with ITO due to the conformal nature of the sputtering method used. This fact is taken into account in our numerical simulations. The device parameters are determined by optimization using FDTD simulations to obtain large absorptance in the wavelength range of 4−16 μm. Keeping the thickness of the ITO layer to be 100 nm, we simulate single antennas of various lengths, widths, periodicities, and spacings between its Babinet inverse. For the polarization-dependent design, we search for a single antenna element that achieves the

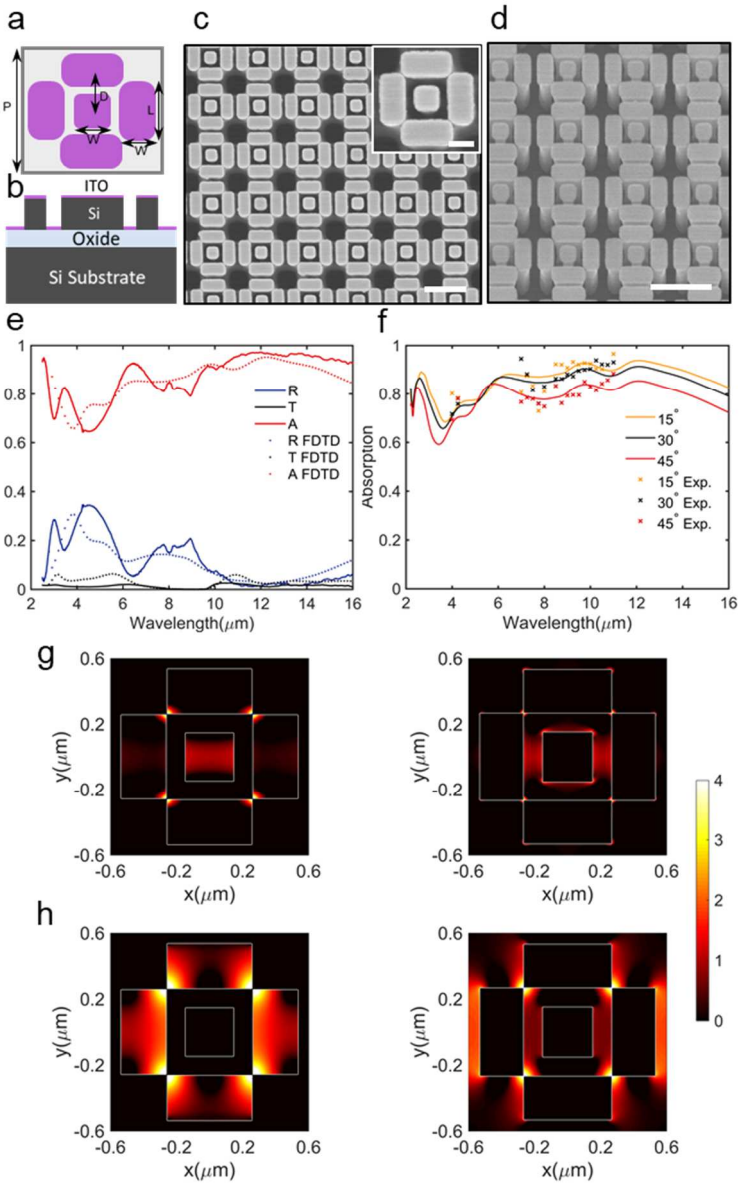

Figure 2.4. Design and performance of a broadband polarization-independent infrared metasurface absorber. (a) Top view of the unit cell of the metasurface. (b) Cross-sectional view of the unit cell of the metasurface. (c) SEM image of a fabricated device (scale bar: 1000 nm). Inset: one unit cell (scale bar: 300 nm). (d) SEM image taken at an oblique angle of a fabricated device (scale bar: 1000 nm). (e) Measured and simulated reflection, transmission, and absorption spectra of the metasurface absorber. (f) Simulated and measured absorption spectra at different incident angles. (g, h) Spatial distributions of absorbed optical power on the plane of M1 (left) and M2 (right) at λ = 5.96 and 12 μm, respectively. Polarization of incident light is along y-axis.

largest absorption over the largest possible bandwidth using FDTD simulations. We then supplement the first antenna by adding additional antennas of different lengths to increase

absorption in the wavelength ranges where the absorption provided by the first antenna is weak, while keeping the cavity spacing fixed. Since the cavity spacing has been fixed, the absorption produced due to destructive interference resulting from these new antennas at various wavelengths might not be complete, leading to a slightly lower values of absorption. Using this very simple scheme, we arrive at a three-element unit cell with lengths, L1 = 1450 nm, L2 = 1250 nm, L3 = 550 nm, widths, W = 400 nm, interantenna gap, D = 700 nm, periods Px = 3600 nm, and Py = 1550 nm, and cavity spacing of 1400 nm (Fig. 2.3a). SEM images of the fabricated device are shown in Fig. 2.3(c,d).

We measure the reflection (R) and transmission (T) spectra of fabricated devices using Fourier Transform Infrared (FTIR) spectroscopy and calculate the absorption spectra defined by eq 3. Both the reflection and transmission measurements are carried out at normal incidence with linear polarization in the direction along the antenna rod. The results of FTIR measurements are plotted in Fig. 2.3e along with the corresponding results obtained from FDTD simulations. We observe super broadband absorptance of over 75% across the entire wavelength range of 4−16 μm, a two-octave span across the spectral region corresponding to thermal radiation. We also fabricate and characterize periodic arrays of the individual antennas that compose the polarization-dependent metasurface absorber. The resulting spectra (see Fig. 2.2A2) clearly show broad resonances centered at λ = 6, 10, and 13 μm supported by the arrays of antennas with length of 550, 1250, and 1450 nm, respectively, with a good agreement with FDTD simulations. But the overall bandwidth of large absorption is limited around these resonance peaks unlike the broadband operation shown by the multiplexed design in Fig. 2.3a.

We calculate spatial distributions of absorbed power per unit volume, $P_{abs} \propto |E|^2 \epsilon''$, and the results are shown in Fig. 2.3(g−i). We observe that absorption on the M1 layer (ITO rods) is larger than that on the M2 layer (ITO apertures). This is expected since the M2 layer is not specifically designed to be resonant at any wavelength and acts mostly as a mirror. We also observe that light with longer wavelengths is primarily absorbed by longer antennas and that the largest absorption occurs at the edges of the antenna rods.

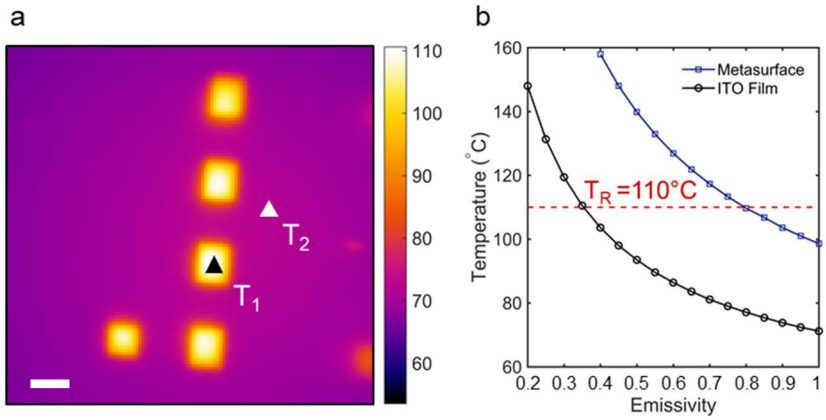

Figure 2.5: Emissivity measurements using a thermal camera. (a) Magnified thermal image of devices where T1 and T2 representing temperatures of the metasurface absorber and the unpatterned ITO film, respectively. Scale bar: 200 μm. (b) T1 and T2 as a function of emissivity.

We conduct FDTD simulations to investigate absorption as a function of incidence angle. Figure 2.3f shows that broadband high absorption is retained for incident angles of up to 30° and absorptance starts to decrease at an incident angle of 45°. We have validated these numerical simulations with measurements in the wavelength range of 4−11 μm (see Supplementary section 2.1 for details).

Using the same design principles, we also demonstrate a polarization-independent absorber. The unit cell of the metasurface is shown in Fig. 2.4a and consists of two types of rod antennas arranged symmetrically with the following parameters: L = 520 nm, W = 300 nm, D = 400 nm, and P = 1200 nm. The vertical cross-section of the unit cell is shown in Fig. 2.4b, where the cavity spacing is again 1400 nm. Fig. 2.4(c,d) show SEM images of a fabricated device. Figure 2.4(g,h) shows the spatial distributions of absorbed power of the polarization-independent unit cell at λ = 4 and 12 μm, respectively. We see strong absorption around the region where the horizontal and vertical antennas meet for both wavelengths on both the M1 and M2 planes. The central square antenna primarily absorbs light of shorter wavelengths. Unlike the polarization-dependent design, the power absorbed in the M2 layer is comparable to that absorbed in the M1 layer. Measured spectra of the polarization-independent metasurface absorber are shown in Fig. 2.4e. In this case, we use unpolarized light as the source of illumination. We observe a large absorption of greater than 80% over the entire wavelength range of 6−16 μm. The overall performance of the fabricated

device agrees with FDTD simulations, and we attribute the discrepancy in the position of some resonances to fabrication errors. Similar to the polarization-dependent unit cell, this design maintains broadband high absorptance for incident angles of up to 30° as shown by FDTD simulations and experiment in Fig. 2.4f. Note that we obtain such performance without using complex optimization schemes for the design and complicated device fabrication techniques.

We further investigate the thermal emissivity of the fabricated metasurface absorbers using a thermal camera. Emissivity of samples can be obtained by heating the samples with a reference material with known emissivity. At thermal equilibrium, the temperature reported by the thermal camera must be the same for both materials, which serves as a method to solve for the emissivity of the unknown sample. Note that, for accurate measurements of sample temperature, external contributions (i.e., ambient thermal radiation reflected from metasurface absorbers and thermal radiation generated by imaging optics) must be subtracted from the total thermal radiation impinging on the camera sensor (see Supplementary section 2.1 and Fig. 2.2S3a for details).

The thermal images of the devices heated to 150°C are shown in Fig. 2.5a (see Fig. 2.2S3b for thermal images of samples at room temperature) where the metasurface absorbers are the regions with bright yellow coloration. Thermal image of the reference (see Fig. 2.2S3c) material (black electrical tape) gives us a reference temperature (TR) of 110 °C. Figure 2.5b shows plots of calculated temperature as a function of emissivity for spots on the metasurface absorber (T1) and the ITO thin film surrounding it (T2) in Fig. 2.5a. The emissivity values that return TR are the correct value of emissivity for the two spots. We observe from the figure that emissivity of our metasurface absorbers is >0.8 and that of the unpatterned ITO film is around 0.3. These values agree qualitatively with absorptance values retrieved from the FTIR measurements. In conclusion, we have experimentally demonstrated superbroadband metasurface infrared absorbers based on engineered ITO that maintain large absorptance and broadband performance over a wide range of incidence angles. The engineered optical properties of ITO enable the creation of metasurfaces that have broad antenna resonances. We developed an asymmetric Fabry−Perot model to describe the operation principle of our absorbers as a pair of metasurfaces acting as a broadband cavity. Results of the model agree well with FDTD simulations. We used the simulation results to optimize

the unit cell of the metasurface absorber and experimentally achieved over 80% absorptance in the entire 4−16 μm wavelength range, a significant improvement over similar works reported previously. Using FDTD simulations, we showed that this performance is maintained for a wide range of incidence angles (±30°). We have thus successfully demonstrated an alternative method of achieving super broadband absorbers of infrared light using ITO with engineered optical properties. Using thermal imaging techniques, we also obtained thermal emissivity of our fabricated devices. Our approach opens up new possibilities of realizing active optoelectronic devices operating in the mid-infrared such as active thermal emitters and imaging sensors that can be fabricated using CMOS compatible techniques.

Supplementary Section 2.1: Methods and Supplementary Information

Numerical Simulations. Finite Difference Time Domain (FDTD) simulations of various unit cell designs were carried out using Lumerical FDTD Solutions. We used periodic boundary conditions in x and y and perfectly match layer (PML) in z for all simulations. Material properties obtained from mid-IR ellipsometry (IR-VASE) were used to simulate the tailored ITO material films. The Palik library was used to simulate the dispersion of the Silicon and Silicon Dioxide. We obtained reflection(R) and transmission (T) spectrum from the simulations of the unit cells and calculated the absorption using the relation A = 1 - T - R.

To obtain absorptance at non-normal incidence, Broadband Fixed Angle Source Technique (BFAST) is used in the FDTD simulation, which removes the wavelength dependence of injection angle from the simulation.

Angular Reflectivity Measurements. The Fourier Transform Infrared (FTIR) spectroscopy system we used for measurement at normal incidence cannot perform similar measurements at non-normal incidence. We built a separate setup for those measurements, which uses a tunable Quantum Cascade Laser (QCL) as the source. The laser (MIRcat – 1400, Daylight Solutions) has three

tunable QCLs operating in the wavelength range of 3.94 – 4.39 μm, 6.89 – 9 μm, and 7.96 – 11 μm, respectively. We are therefore limited from conducting angular measurements beyond 11 μm. The light from the laser is focused onto the sample using an off-axis parabolic mirror of an effective focal length of 50 mm. The sample is mounted on a stage capable of rotating about a central axis. The reflected light is measured using a power meter (Ophir Optronics Solutions).

Nanofabrication. The metamaterial absorber was fabricated on a silicon on insulator substrate with the device layer of 1400nm and a buffered oxide layer of 2200nm. Double layer PMMA 495K A4 and 950 A2 were spun on the chip at 4000rpm for 60secs and baked at 180°C for 8 and 2 minutes, respectively. The unit cell patterns were defined on the resist layer using JEOL JBX-6300FS electron beam lithography system. After development of the resist in 3:1 Iso-propyl Alchohol (IPA) : De-ionized water (DI) solution for 2 minutes, 40nm of chromium was evaporated on it using electron beam evaporation and followed by lift-off in Remover PG. The pattern was finally transferred to silicon by inductively coupled plasma etching in a mixture of SF_6 (40sccm) and O_2 (16sccm) at -100°C. The chromium hard mask was wet etched in Transene. Finally, 100nm of ITO was deposited using RF magnetron sputtering in a Denton Discovery 18 confocal-target system, with ITO (99.99% purity) target in Ar atmosphere at room temperature. The property of the deposited ITO was then tuned by post-deposition annealing using a Mellen thermal furnace at 250°C for 1 hour in nitrogen atmosphere.

Characterization. ITO films grown under various growth and post-annealing conditions were characterized using a mid-infrared J. A. Woollam variable angle spectroscopic ellipsometer (VASE). The reflection and transmission spectroscopic measurements were carried out using Bruker Scientific Vertex 70v Fourier transform infrared spectrometer equipped with a globar source and a liquid-nitrogen-cooled Mercury Cadmium Telluride (MCT) detector (λ=2.5-16 μm).

For emissivity characterization, fabricated devices were imaged using a thermal camera (FLIR T640) equipped with a Germanium zoom-in lens. A Zinc Selenide (ZnSe) lens (Thorlabs) with 0.42 NA was used between the sample and the camera for magnification.

The total thermal radiation received by the camera is given by:

$$W_{tot} = \tau\epsilon_s\sigma\mathrm{T_s^4} + \tau(1-\epsilon_s)\sigma\mathrm{T_a^4} + (1-\tau)\sigma T_{lens}^4, \qquad (2.1S1)$$

where ϵ_s is emissivity of the sample, T_s, T_a, T_{lens} are, respectively, temperatures of the sample, ambient, and ZnSe lens; σ is the Stefan–Boltzmann constant; τ is the power transmissivity of thermal radiation through the ZnSe lens and is taken to be 0.8. The first term on the righthand side of Eq. (2.1S1) represents thermal radiation generated by the sample and transmitted through the ZnSe lens; the second term represents ambient thermal radiation reflected by the sample; the third term represents thermal radiation from the ZnSe lens itself. The camera reports temperature of the sample by solving $\mathrm{T_s}$ from the above equation, that is:

$$T_S = \left[\frac{\frac{W_{tot}}{\sigma} - \tau(1-\epsilon_s)\mathrm{T_a^4} - (1-\tau)\mathrm{T_{lens}^4}}{\epsilon_s\tau}\right]^{\frac{1}{4}} \qquad (2.1S2)$$

We used the following three steps to derive the emissivity of our samples.

Step 1: Experimentally obtain $\mathrm{T_a}$

The primary contribution to the ambient radiation is thermal radiation generated by the thermal camera, because of its close proximity to the sample. Therefore, we shall not take lab ambient temperature 25˚C as $\mathrm{T_a}$. To experimentally determine Ta, we used a flat silver mirror as the sample and place it on a hot plate set to 150˚C. The camera was focused onto the surface of the mirror. The latter has near-zero emissivity; therefore, the reading of the thermal camera only has two contributions:

$$W_{Ag\_mirror} = \tau\sigma\mathrm{T_a^4} + (1-\tau)\sigma T_{lens}^4. \qquad (2.1S3)$$

We measured $\mathrm{T_{lens}}$ to be 35˚C and the reading from the thermal camera gives us $\mathrm{T_a}$:

$$T_a = \left[\frac{W_{Ag_{mirror}}}{\sigma\tau} - \frac{(1-\tau)}{\tau}T_{lens}^4\right]^{\frac{1}{4}}. \quad (2.1S4)$$

Step 2: Experimentally obtain T_s

We replaced the silver mirror from the hot plate with our sample. A piece of black electrical tape with an emissivity of ϵ_{tape}=0.97 was attached to the top surface of this sample. We assumed that eventually the tape reaches the same temperature as that of the sample, T_s. T_a obtained from Step 1 was input into the camera, which calculates T_s (see Fig. 2.2S3c) using an equation similar to Eq. (2.1A2):

$$T_S = \left[\frac{\frac{W_{tape}}{\sigma} - \tau\left(1-\epsilon_{tape}\right)\mathrm{T_a^4} - (1-\tau)\mathrm{T_{lens}^4}}{\epsilon_{tape}\tau}\right]^{\frac{1}{4}}. \quad (2.1S5)$$

Step 3: Experimentally obtain ϵ_{meta}, emissivity of the metasurface absorbers

We input a series of ϵ_{meta}, ranging from 0.2 to 1.0, into the thermal camera, which produces a corresponding series of temperature using:

$$T_S = \left[\frac{\frac{W_{meta}}{\sigma} - \tau(1-\epsilon_{meta})\mathrm{T_a^4} - (1-\tau)\mathrm{T_{lens}^4}}{\epsilon_{meta}\tau}\right]^{\frac{1}{4}}. \quad (2.1S6)$$

The value of ϵ_{meta} that yields the same temperature as that of the black tape, T_s, obtained in Step 2, should be the real thermal emissivity of the metasurface device (Fig. 2.5b).

Supplementary Section 2.2S. Supporting figures for broadband metasurface absorber

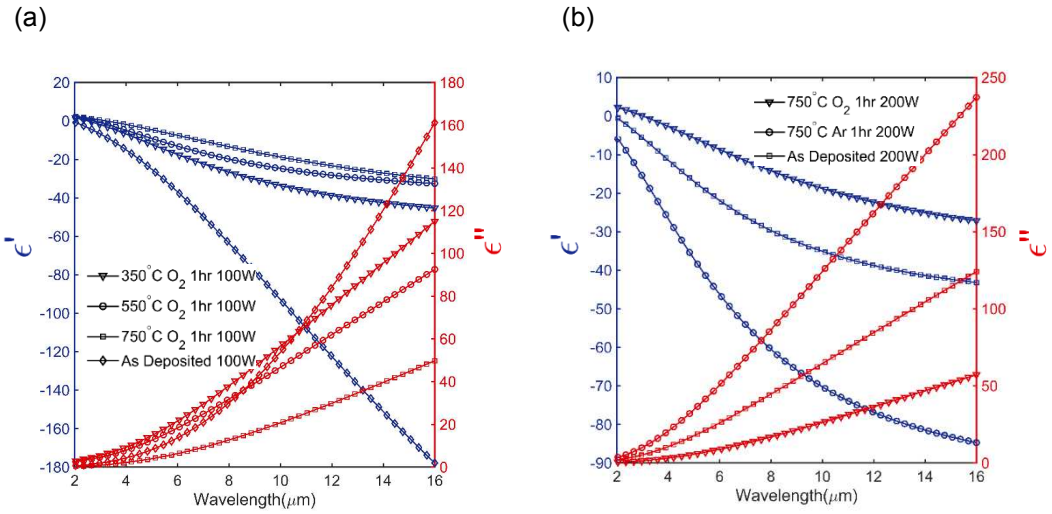

Figure 2.2S1: Tailoring optical properties of ITO. (a) The comparison of real and imaginary dielectric permittivity of ITO under different annealing temperature for a duration of 1 hour and sputtering power set to 100 W. (b) The comparison of real and imaginary dielectric permittivity of ITO annealed to 750C in oxygen and argon atmosphere for a duration of 1 hour and sputtering power set to 200 W.

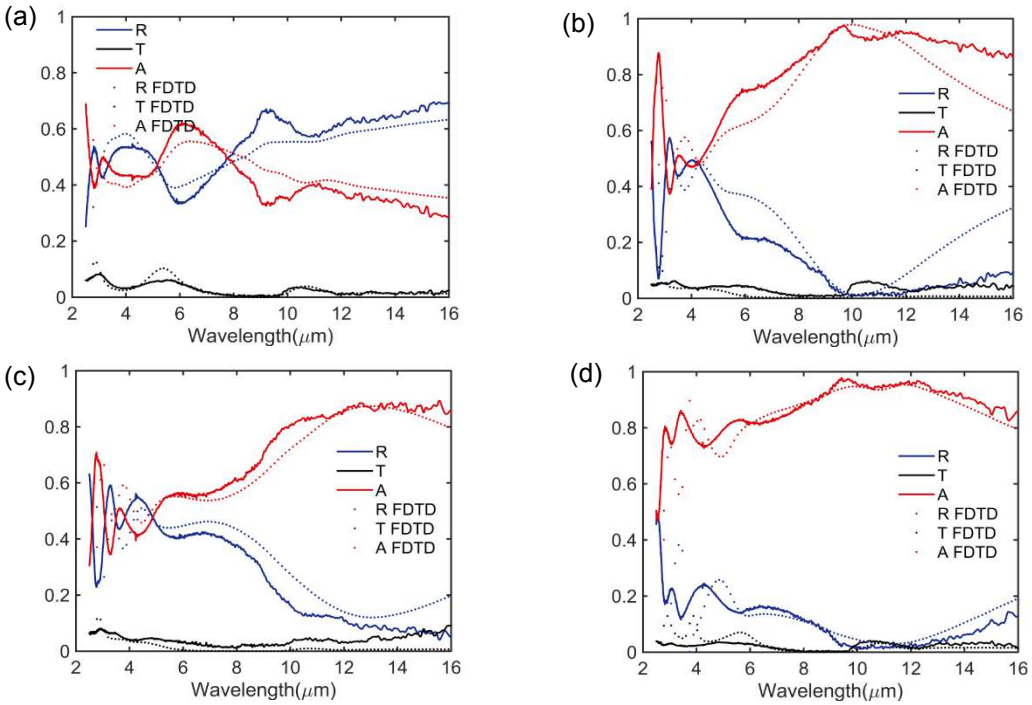

Figure 2.2S2: Measured responses of periodic array of individual rods that form the polarization dependent broadband absorber (a,b,c) Simulated and measured reflection, transmission and absorbance of periodic arrays of nanorods with length 550, 1250 and, 1450 nm respectively each with height of 1400 nm. (d) The corresponding measured and simulate responses of the combined structure as seen in Fig. 2.3.

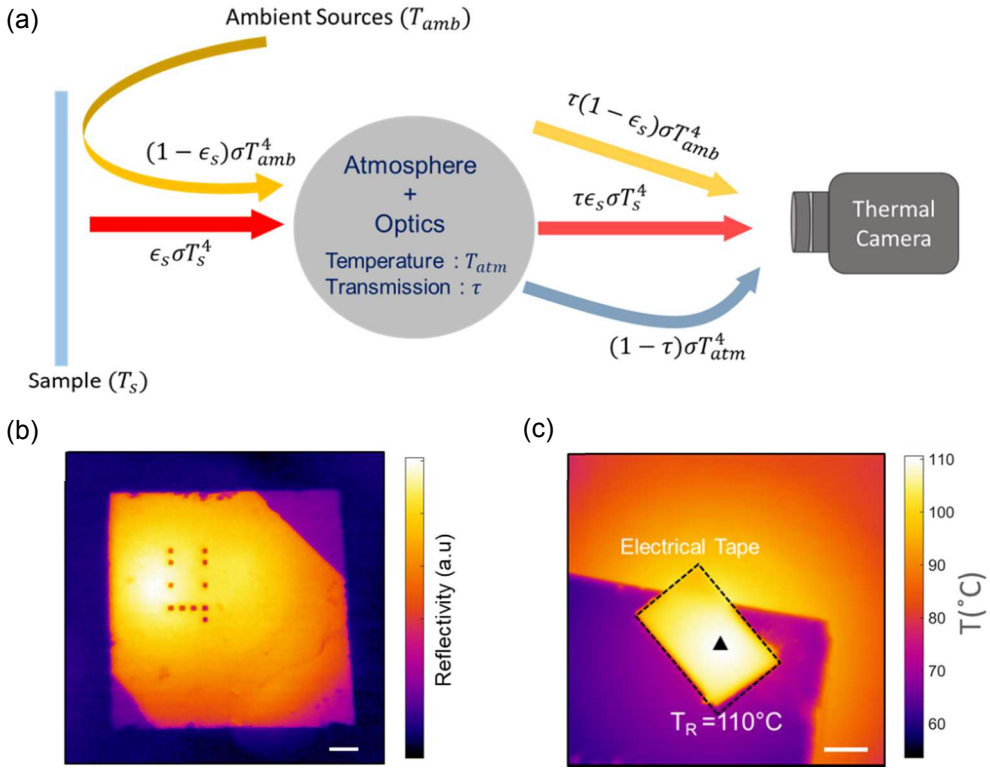

Figure 2.2S3. Emissivity measurements using thermal camera. (a) Contribution to the total thermal radiation impinging on the thermal camera. To obtain the actual temperature of the sample, contribution to the thermal radiation from ambient sources via reflection and the background radiation from the atmosphere must be subtracted. (b) Reflected ambient thermal energy from the fabricated chip at room temperature. The darker square spots are the metasurface absorbers. This shows the reduced reflection of the absorbers when compared to the surrounding unpatterned ITO thin film (bright yellow). Scale bar: 1mm. (c) Thermal image of black electrical tape attached to the chip used as a reference material with known emissivity. Scale bar: 1mm.

Chapter 3: Multifunctional Metasurfaces

This chapter introduces design frameworks made possible by metasurfaces for control of multiple parameter of the incoming optical wavefront. In particular, optical devices that can simultaneously impart independent phase/amplitude masks at multiple wavelengths will be explored. These multiwavelength metasurfaces can be realized via different strategies. Recent reports have utilized spatial [99,100], angular [101,102] or polarization [25,103] multiplexing to achieve lenses and holograms at 2 or more wavelengths simultaneously. In following sections, I will demonstrate strategies to achieve an RGB metasurface lens, an RGB phase and amplitude hologram using a doublet and explore degrees of freedoms available in geometric phase metasurfaces to design polarization encoded metasurfaces.

3.1 Multiwavelength Metasurfaces

Realizing broadband metasurfaces is a challenging task. It demands arbitrary control of both spatial and spectral responses from metaunits. Given the degrees of freedom available in meta-unit design, such arbitrary responses cannot be realized. That is to say, meta-units can only provide a limited range of phase vs wavelength response. However, metasurfaces can be designed to address optical functionality at a few specific wavelengths even with these limited spectral responses for some specific optical functionality like lensing. Such devices can be useful for applications where the source of light is generally narrowband. To realize such a multiwavelength metasurfaces, utilizing all the design space available to populate metaunit library responses is crucial. In particular for dielectric metasurfaces, such responses are particularly limited for metaunits that behave like effective mediums as the spectral responses of these type of metaunits provide dispersive response that is similar to material dispersion. Resonant metaunits on the other hand can provide a wider variety of responses due to nature of phase excursion around resonant peaks. However, for transmissive metasurfaces, such metaunits also display dips in amplitude near these resonances, hence such a strategy is only preferable for reflective type metasurfaces. An example of such a multifunctional metasurface in reflection has been reported recently [104] using

guided mode resonances. In the following section, I will present a demonstration of a metasurface RGB lens operating in transmission mode in the visible that utilizes dispersion engineering to achieve the multiwavelength functionality.

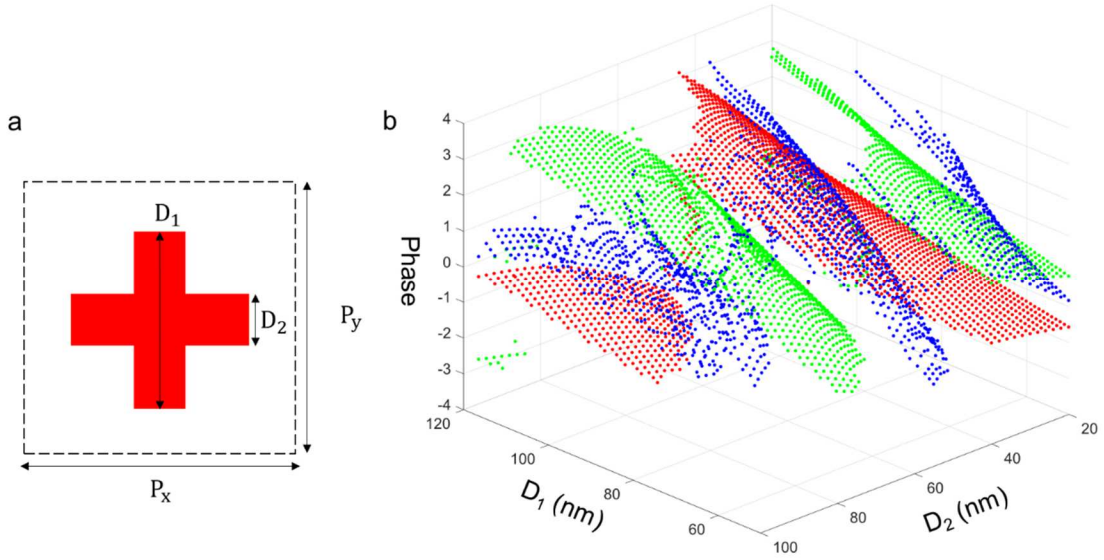

Figure 3.1: Cross archetype library for RGB metalens. (a) Design parameters of the cross archetype. P_x and P_y are the lattice period in x and y dimensions respectively. For visible wavelengths they are chosen to be 280 nm for subwavelength sampling. The cross nanopillar is made up of TiO_2 with a height of 860 nm. (b) The phase responses modulo 2π of the TiO_2 based cross archetypes at 430 (blue), 530 (green) and 620 (red) nm as a function of its two design parameters.

3.1.1 RGB Metalens in the Visible

For applications where the source of light is a narrowband laser or an LED, monochromatic metasurfaces can ideally replace conventional optical elements. However, for applications such as multiphoton microscopy or LED based projection, optical elements must focus light at multiple wavelengths to the same focal spot. As mentioned earlier, spatial multiplexing [99] can be used to divide the plane of the metasurface to focus chosen wavelengths correctly and achieve multiwavelength lensing. However, such a strategy usually results in lowered efficiency. Here, I demonstrate a strategy that utilizes dispersion engineering in dielectric metaunits to achieve a multiwavelength metalens without using spatial multiplexing.

High contrast dielectric nanopillars discussed in the introductory chapter can be structurally engineered in order to generate a variety of spectral responses. This is achieved through dispersion engineering similar to waveguide mode dispersion engineering in photonic integrated circuits. Waveguide cross-section is designed to allow for eigenmodes with varying degree of overlap with the core at various wavelengths. A larger difference in mode overlap at shorter and longer wavelength corresponds to a larger dispersion and vice versa. A more detailed explanation of this methodology is presented in chapter 4.

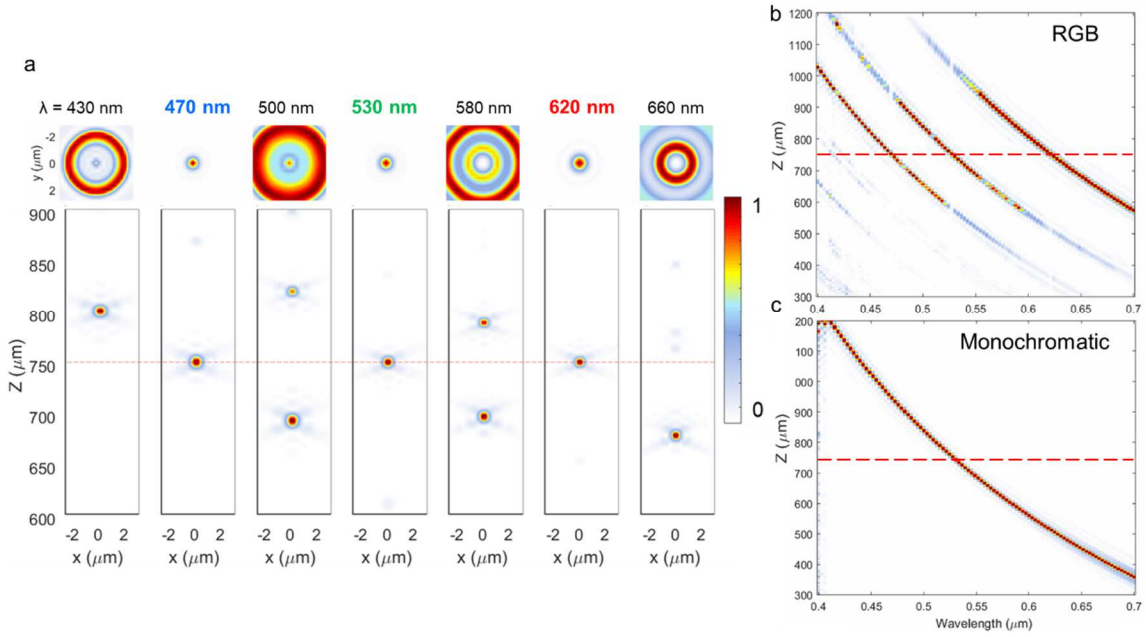

Figure 3.2: Simulation results of RGB metalens. (a) X-Y intensity distribution at the focal plane for a range of wavelengths with 470, 530 and 620 nm chosen as the design wavelengths and X-Z intensity distribution of focused light exiting the metalens showing alignment of focal plane for the RGB wavelengths at the design focal length. Note outside of the RGB wavelengths, the metasurface still behaves like a lens but their focal lengths are chromatically shifted according to diffractive dispersion. (b,c) Comparison of position of focal plane as a function of wavelength between the designed RGB lens and a monochromatic metalens with design wavelength at 530 nm.

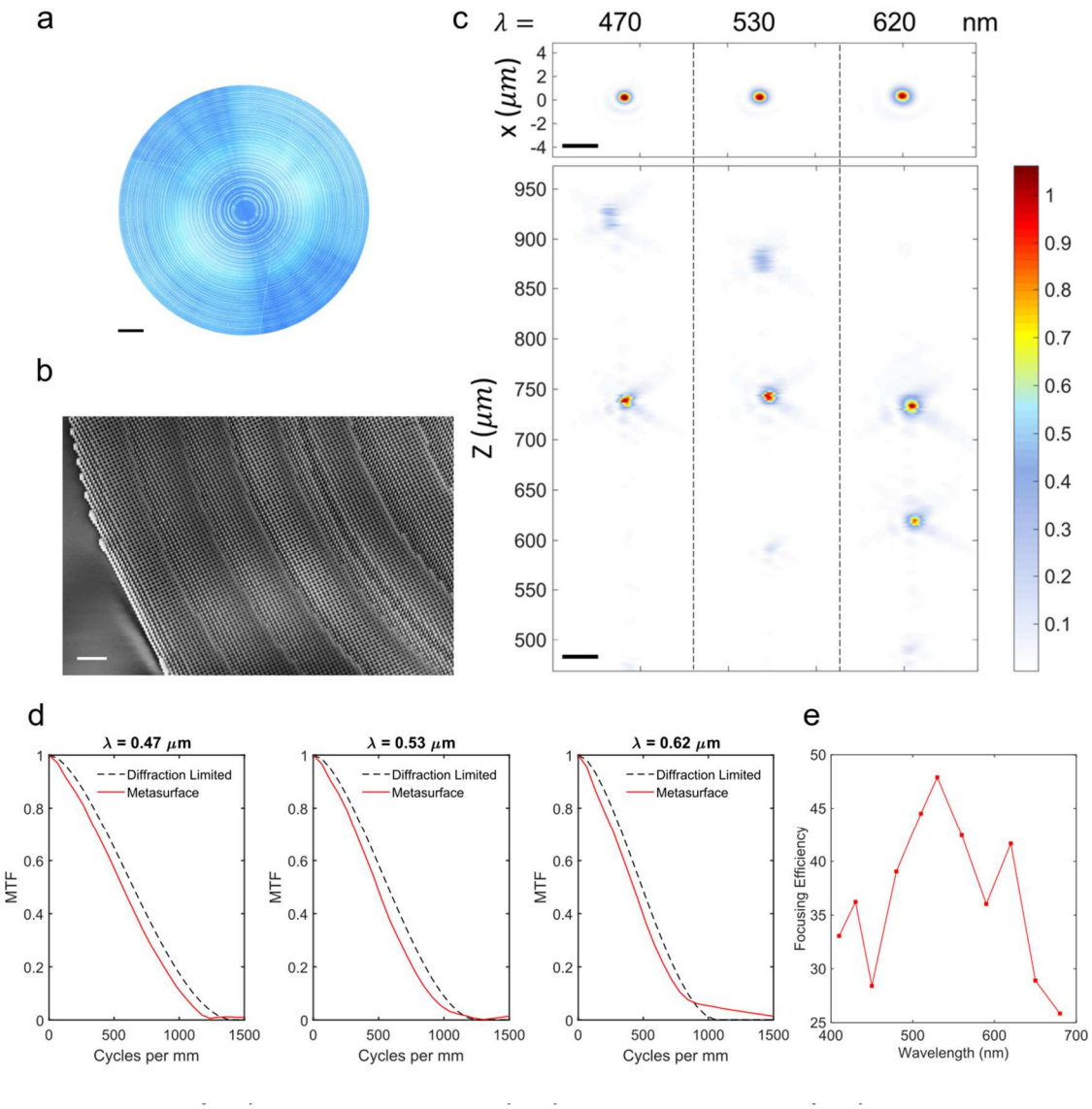

Figure 3.3: Experimental results demonstrating the performance of an RGB metalens. (a) Optical image of a fabricated RGB metalens with a diameter for 500 μm and focal length of 750 μm. Scale bar: 50 μm. (b) Scanning electron micrograph of a fabricated metalens. Scale bar: 2 μm. (c) Focal and X-Z plane intensity distribution of light exiting the RGB metalens for the design wavelengths. Scale bar: 1 μm. (d) Modulation transfer function (MTF) calculated from the focal plane intensity from (c) for the design wavelength compared to the diffraction limit value. (e) Measured focusing efficiency of the RGB metalens. The values peak at the design wavelengths.

Figure 3.1a shows a cross shaped metaunit archetype with its design parameters. This archetype has a symmetric cross-section which allows for polarization independent response. For the visible wavelength such metaunits are made up of TiO_2 which is a high index dielectric material in this

wavelength range with no absorption. The substrate is made up of fused quartz. Figure 3.1b shows the phase responses of such an archetype at three wavelengths in the visible. These unique sets of responses are not only a function of metaunit cross-section but also its height. Since, phase is accumulated through propagation in these nanopillars, taller pillars can provide more than 2π phase excursion. This is important as it allows for more varied spectral responses considering phase responses under modulo 2π. These responses can be used to satisfy the spatial and spectral phase requirement of a converging lens which can be easily derived from geometrical argument as:

$$\Phi(r,\lambda) = -\frac{2\pi}{\lambda}\sqrt{r^2+f^2} \qquad (3.1)$$

where λ is the desired wavelength, r is the spatial co-ordinate in the plane of the metasurface and f is the required focal length. For an RGB wavelength, this requirement must be satisfied for 3 wavelengths at each spatial location. Since it is usually not possible to exactly satisfy these spectral and spatial requirements, we employ an error minimization method which seeks to minimize the phasor error between the required and the available responses for all the target wavelength simultaneously to achieve the best possible sampling, mathematically,

$$\min \sum_{i=1}^{3} \left| A_{req} e^{i\phi_{req}(x,y,\lambda_i)} - A_{lib} e^{i\phi_{lib}(x,y,\lambda_i)} \right|^2 \qquad (3.2)$$

where $A_{req}, \phi_{req}, A_{lib}\ and\ \phi_{lib}$ are the amplitude and phase response pairs for the required lens and the same for an element of the metaunit library. Note that other optimization schemes can be employed for better results such as using weighting factor for different wavelengths or using min-max optimization routines.

Using this method, we design an RGB metalens with diameter of 0.5 mm and a focal length of 0.75 mm for 470, 530 and 620 nm representing the blue, green and red wavelengths. The corresponding numerical aperture (NA) is 0.3. The result of the error minimization for the 3 design wavelengths is shown in supplementary Fig. 3.1Sa showing reasonable sampling of the required phase at the specific wavelength. Figure 3.2a shows simulated performance of the RGB metalens with the chosen wavelengths producing focal spots at the designed focal length. Notice that away

from the designed wavelengths, the focal spot as a function of wavelength is shows a behavior corresponding to diffractive dispersion. This trend can be seen clearly in Fig. 3.2b where away from the 3 chosen wavelength, strong chromatic aberration corresponding to diffractive dispersion (i.e. focal length $\alpha \frac{1}{\lambda}$) is observed. Notice, that for the chosen wavelengths, parasitic spots, which are additional focal spots forming in planes other than the design focal plane are significantly reduced due to error minimization process. As a comparison, chromatic dispersion in monochromatic metalens with the center wavelength at 530 nm of the same NA is can be seen in Fig. 3.2c. We can clearly note that the overall chromatic shift between the shortest (400 nm) and the longest (700 nm) wavelength for the RGB metalens is smaller than the same shift for the monochromatic case, even though we did not specifically design our metalens with that intention.

We experimentally validate the simulation result by fabricating the RGB metalens described by the parameters above using conventional nanolithography processes (see supplementary section 3.1S for details). The optical image of a fabricated RGB metalens is shown in Fig. 3.3a and the zoomed in view of the individual nanostructures comprising it can be seen in a scanning electron micrograph (SEM) in Fig. 3.3b. The TiO_2 based fabricated RGB metalens is then characterized by an optical metrology setup specifically designed to measure the 3D point spread function (PSF) of metasurfaces. Figure 3.3c shows the focal plane intensity and the X-Z slice of 3D intensity distribution of light exiting the RGB metalens. We can see that the focal plane of the 3 designed wavelengths are very close to one another as desired. The presence of some of the parasitic spots can be attributed to fabrication errors and the incomplete coverage of the phase vs wavelength response required. An important figure of merit that is often used when describing the performance of optical lenses is the modulation transfer function (MTF) [105]. It defines how well an optical system can transfer contrast at varying spatial resolution to either a screen or a sensor.

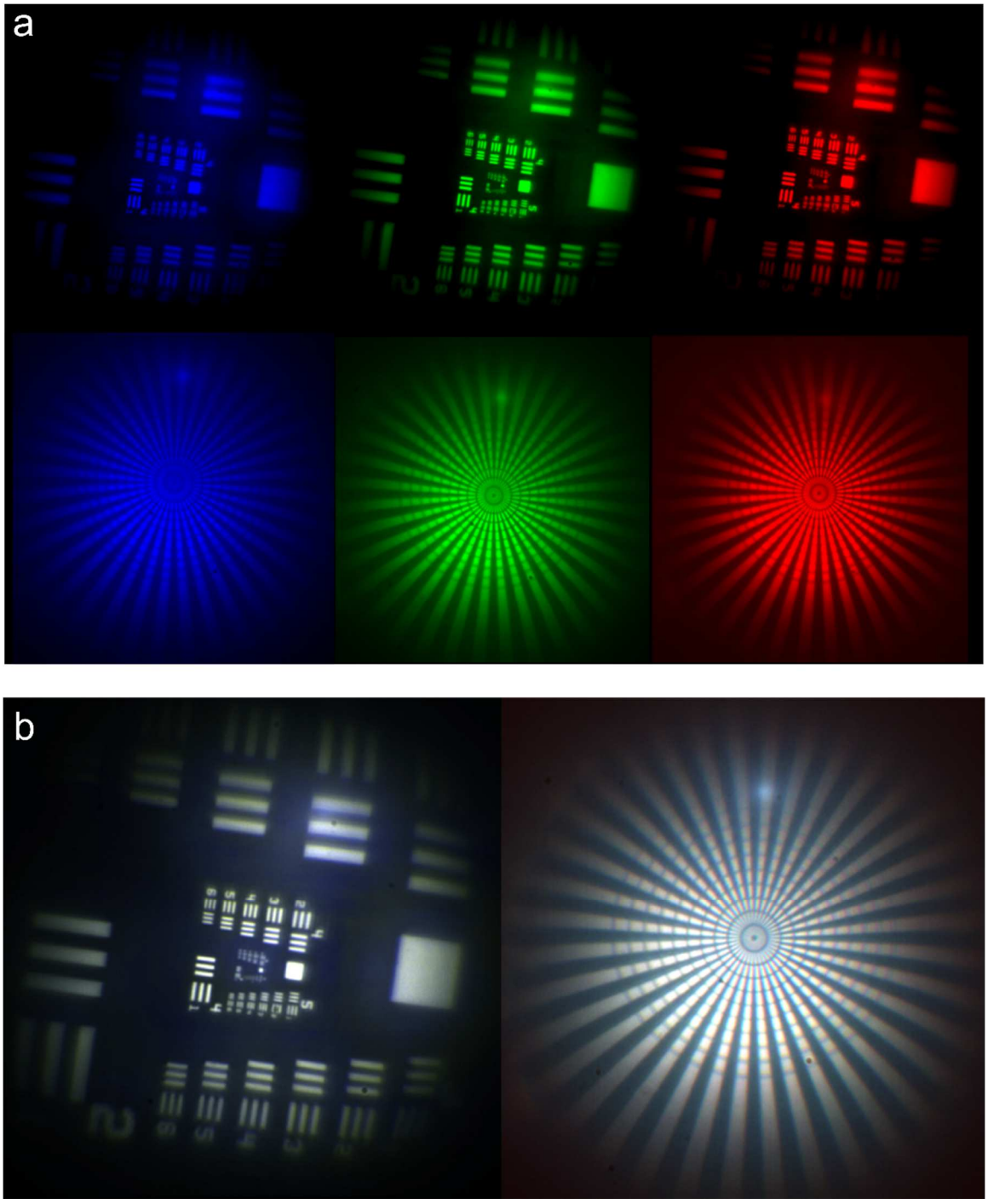

Figure 3.4: Imaging using RGB metalens. (a) Image of an USAF airforce resolution target and a Siemens star at the design RGB wavelength of 470, 530 and 620 nm respectively. (b) Image resulting from combining the RGB channels from (a).

It can be calculated by taking the Fourier transform of the focal plane intensity at a given wavelength. Figure 3.3d compares the diffraction limited MTF to the experimentally measured

values from the fabricated RGB metalens. We observe that the measured values are close to the diffraction limit. A comparison of the simulated MTF values compared with the diffraction limit is shown in supplementary Fig. 3.2Sa. The focusing efficiencies for various wavelengths are plotted in Fig. 3.3e. The focusing efficiencies peaks at the design wavelengths as expected since the focal planes of wavelengths outside of this range are defocused. The reported values are higher than those reported in similar multiwavelength design based metalenses. The simulated focusing efficiency is shown in Fig 3.2Sb and we observe values reaching 80% for the designed wavelengths. This discrepancy can be attributed to fabrication errors and can be seen in the presence of parasitic focal spots.

Finally, we demonstrate imaging in visible using the fabricated RGB metalens. A wavelength tunable narrowband source (~2.5 nm bandwidth) is used to illuminate a resolution target, which is imaged by the RGB metalens to an intermediary back focal plane. This intermediary image is then relayed to the camera sensor via another objective lens (see methods in supplementary section 3.1S). Image is captured at the 3 designed wavelength and moving the relay objective confocal to the focal plane of the RGB metalens. We can see that at the designed focal length, image formed by the metalens preserves the contrast of the objects at the 3 designed wavelengths. Further, combining the 3 image channels into a single RGB image shows very little sign of chromatic aberration. However, it should be noted that chromatic aberration will be observed for larger source bandwidth due to the residual chromatic aberration present away from the design wavelength as discussed above.

Hence, we have successfully demonstrated an RGB metalens imaging device capable of producing chromatic aberration corrected imaging at the specific design wavelength. Such devices can be of use in multiphoton optical microscopy as well as narrowband LED projector systems especially for compact augmented/virtual reality systems.

Supplementary Section 3.1: Methods and Supplementary Information

Metalens fabrication. Amorphous Titanium Dioxide (TiO_2) films of thickness 860 nm are deposited by electron beam evaporation on 500-μm fused quartz substrates starting with Titanium 3 Pentoxide (Ti_3O_5) granules. An Elionix GLS-100 electron beam lithography system is used to define the metasurface lens pattern on a double layer resist (PMMA 495k A4 and 950A2) with a dose of 800 μC/cm2 at a current of 2 nA. A 20-nm layer of ESpacer is spun on top of the double-layer resist to avoid the electron charging effect. After the resist is developed in IPA:DI (3:1) for 2 min at room temperature, 25 nm of chromium (Cr) followed by 25 nm of aluminum oxide (Al_2O_3) are deposited using electron beam evaporation and lifted off in Remover 1165. The metasurface lens pattern is transferred to TiO_2 films by inductively coupled plasma (ICP) etching in a mixture of SF_6, CH_4, Ar and O_2 gases at 10˚C. The Cr and Al_2O_3 mask are the wet etched away as the final step in Transene 1020 etchant.

Optical characterization. A collimated laser beam with a tunable wavelength is incident on the metalens, and the 3D far-field of the lens is measured by acquiring a stack of 2D images at different distances from the lens. The tunable laser beam is generated by passing the emission from a supercontinuum laser source (NKT SuperK Extreme) through a monochromator. (Fianium LLTF) Light exiting the monochromator is coupled into a single-mode fiber and then collimated using an achromatic fiber collimator (PAF2-A4A). The imaging optics for monitoring the far-field of the metalenses consist of a ×100 objective (Nikon 100x), a tube lens of focal length 200 mm, and monochromatic CMOS camera (Andor Zyla 4.5), which are mounted on a motorized stage.

For point spread function measurement, the device plane is brought to focus on the camera using the stage. Then, the stage is moved toward the focal plane of the metalens in predefined increments (typically 1 μm). At each position, the transverse intensity distribution is captured by the camera for desired wavelengths by changing the monochromatic settings. In this way, the 3D far-field of the metalens is measured. The longitudinal intensity distribution is then created for each wavelength by splicing the 3D intensity distribution along the axis of the metalens. For imaging, a resolution

target transparency is illuminated by a narrow band source through a rotating diffuser. This is necessary to avoid speckle which would be present due the coherent nature of the source. The object is then focused by the RGB metalens and relayed to the camera sensor by a x10 objective (Mitotoyu). Image is captured at each design wavelength and then later the 3 channels are combined computationally to produce an RGB image.

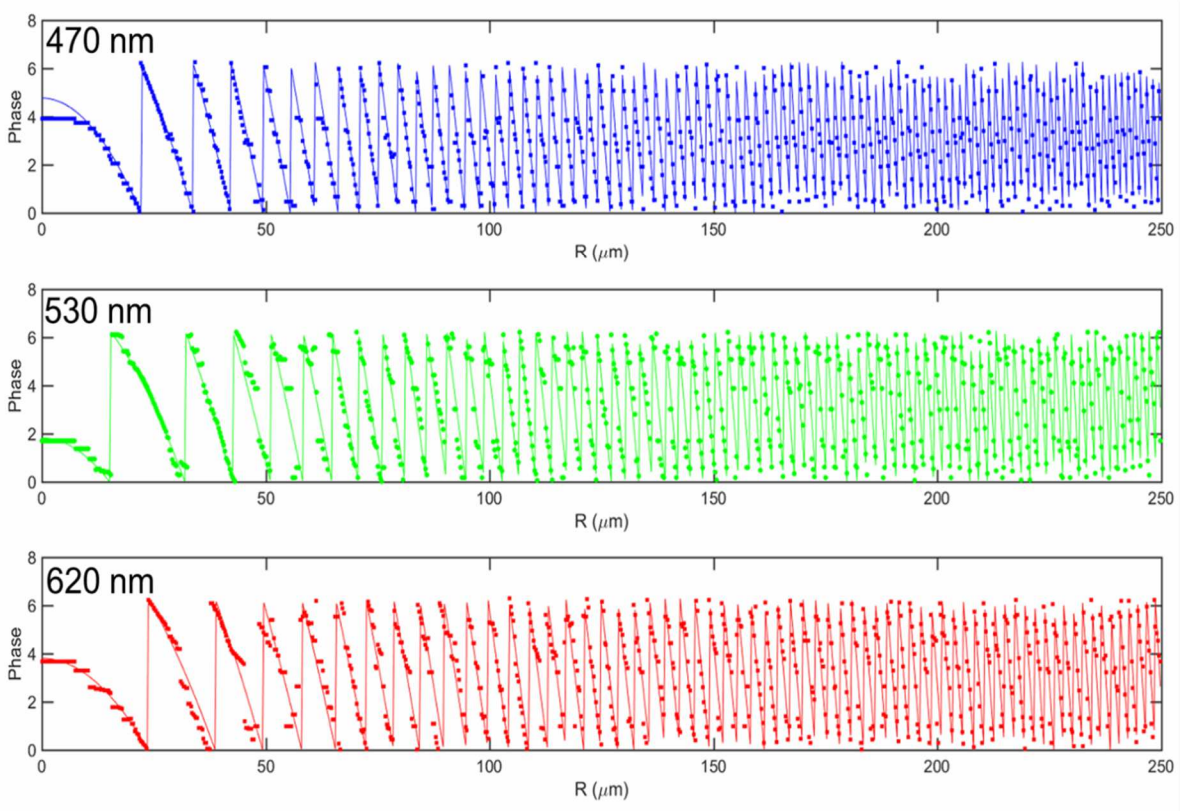

Figure 3.1S: Error minimization result. Comparison of the required phase and the best possible phase response provided by the metaunit library at each position in the RGB metalens for the 3 chosen wavelengths. The lens has a focal length of 750 μm and a radius of 250 μm.

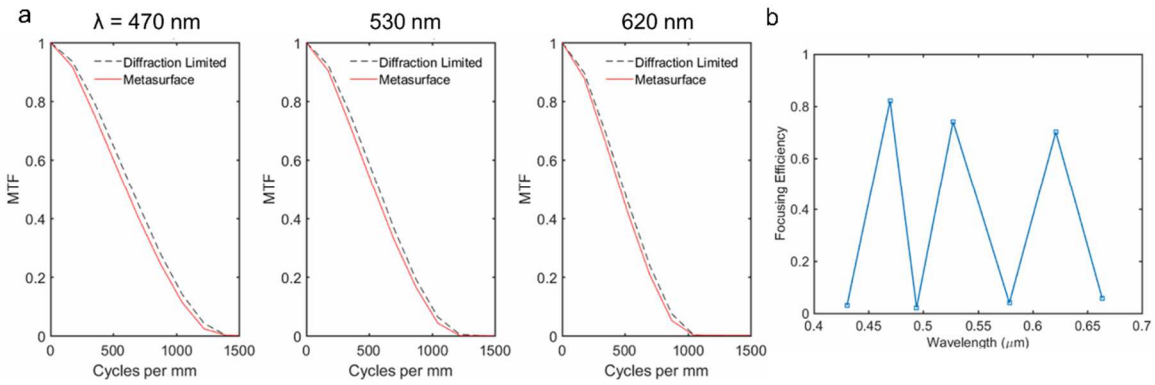

Figure 3.2S. Simulated MTF and focusing efficiencies. (a) Simulated MTF values of the RGB metalens compared to the diffraction limit at the designed wavelengths. (b) Simulated focusing efficiencies as a function of wavelength.

3.1.2 RGB Phase and Amplitude Hologram Doublet

Geometric phase based dielectric metasurface allow control of optical wavefront by simple rotation of metaunit element as discussed in the introductory section. A considerable number of optical devices [32,44,103,106] have been demonstrated using this platform. However, most of these works only impose a phase mask to an incoming optical wavefront. However, geometric metasurface have additional degrees of freedom that can be utilized to control more than one parameter of the optical wavefront. Using dielectric metaunits, simultaneous control of phase and polarization has been efficiently achieved in the near-infrared [25] and visible wavelengths [43]. These reports demonstrate multifunctional metasurfaces where entirely independent phase masks can be applied to any orthogonal pairs of polarized light to generate arbitrary holograms. Such frameworks utilize both form birefringence and the rotational degree of freedom of metaunits to extend the control to multiple parameter of the optical wavefront. As explained in the introductory section, simultaneous phase and polarization control of optical wavefront can be easily transformed to simultaneous phase and amplitude control. A metaunit to realize such a functionality is shown in Fig. 3.5. As discussed before, the amplitude modulation is achieved by applying a polarization filter orthogonal to the input polarization on the light exiting the metasurface. Partial conversion of

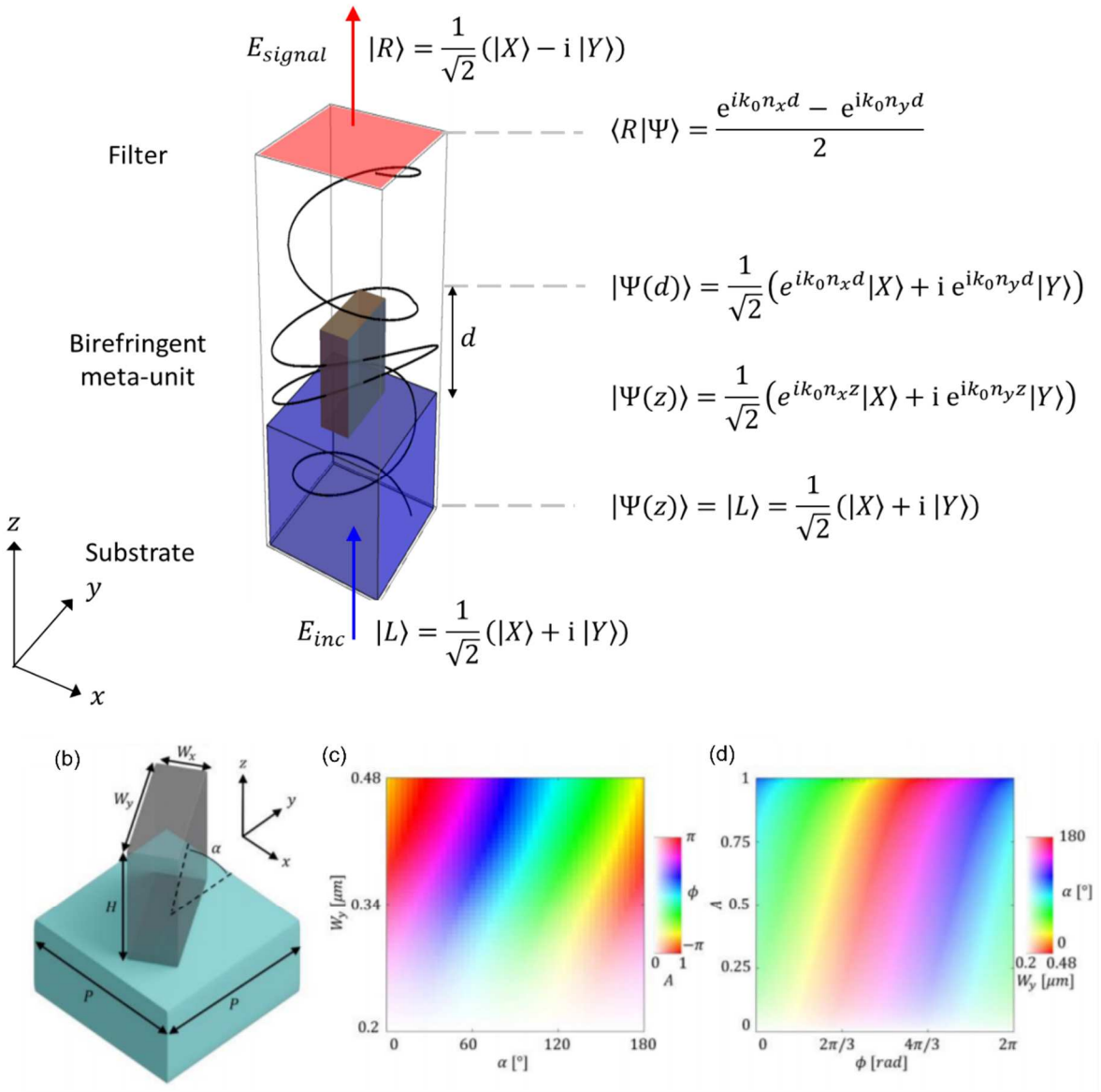

Figure 3.5: Birefringent metaunit for geometric phase. (a) Input circularly polarized light impinges on a birefringent metaunit with a well defined fast and slow axis determined by the waveguide mode index of light polarized along that axis. After passing through the metaunit of height d, the polarization state of the light changes to another point in the Poincare sphere. By applying a filter of opposite handedness to the input light, an amplitude response can be derived [42]. The phase response is derived by adding propagation phase accumulated and twice orientation angle of the metaunit which is the geometric response. (b) Geometric parameters of a meta-unit. (c) Full-wave simulations varying Wy and α for H = 800 nm, Wx = 200 nm , P = 650 nm , and λ = 1.55 μm . The colormap depicts the amplitude, A, of converted light by the saturation and the phase, ϕ, by the hue. (d) "Look-up table" inverting an interpolated version of (c) to specify the values of Wy (saturation) and α (hue) required to achieve a desired A and ϕ (adapted from [42]).

polarization of light from one handedness to other directly imposes an amplitude mask. This also means that we can provide a means of converting a circularly polarized light to any other point on the Poincare sphere. In terms of the metaunit design parameter, this is controlled by the degree of birefringence of the metaunit, i.e. the difference between its length and width. Figure 3.5(b-d) shows the phase and amplitude response of a metaunit for the near-infrared wavelength of 1550 nm based on amorphous silicon on quartz material platform. We utilize the width and the orientation angle as

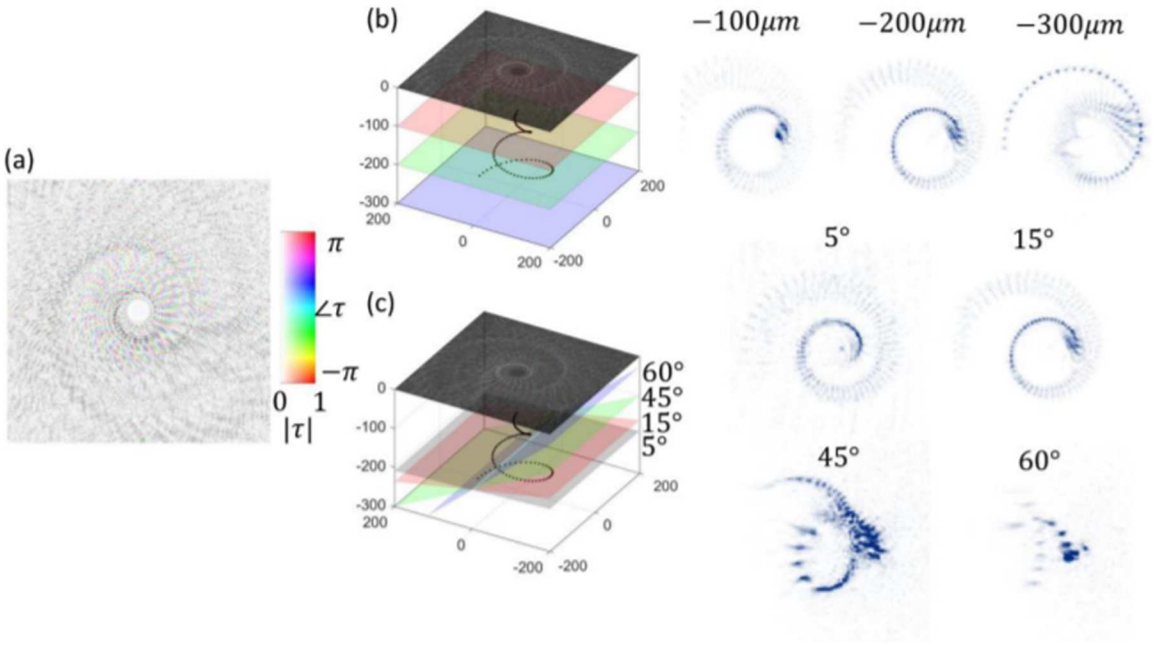

Figure 3.6: Experimental demonstration of depth and parallax in a 3D holographic object. (a) Complex transmission function, τ, of a 3D coil that is 400 × 400 μm in size. (b) Experimental reconstruction of the coil at three depths, showing the 3D nature of the coil. The approximate focal plane positions relative to the metasurface plane and point sources representing the coil are shown for reference. Note that the focal planes are tilted by approximately 15° to the metasurface to reduce spurious back reflections that were present. (c) Reconstruction of the coil at varying observation angles with approximate focal planes for reference, demonstrating parallax. (adapted from [42])

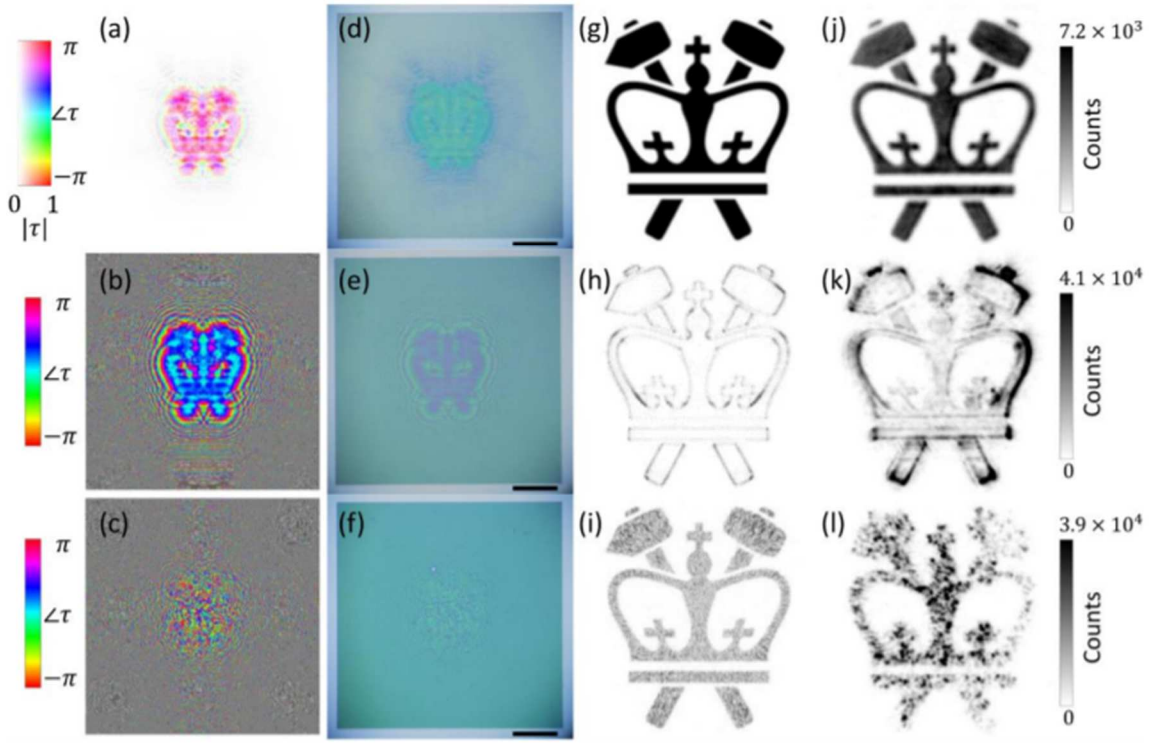

Figure 3.7: Experimental comparison of phase-amplitude (PA, top row), phase-only (PO, middle row), and Gerchberg-Saxton (GS, bottom row) holography. (a-c) The required amplitude and phase across each metasurface, where the saturation of the image corresponds to the amplitude and the hue corresponds to the phase. (d-f) Optical images of fabricated holograms. Scale bars are 150 μm. (g-i) Simulated reconstruction of the holograms. (j-l) Experimental reconstruction of the holograms, with counts shown for comparison. (adapted from [42])

the two parameters that can completely provide any arbitrary combination of phase and amplitude. Using this design, we have shown a phase and amplitude hologram in the near infrared that can among many applications including generating complex 3D point spread functions and faithfully reconstruction of 2D objects [42]. Figure 3.6 shows a demonstration of a 3D point cloud point spread function arranged in a spiral generated by a phase and amplitude metasurface. Individual points can be observed by accessing different focal depths and angle of observations. Other complex point spread function can be similarly designed for applications such as atomic tweezer array [107] and 3D point particle tracking [108].

Phase and amplitude (PA) holograms also demonstrate significantly better-quality reconstruction of 2D scenes when compared to phase only (PO) holograms and phase only holograms generated from iterative algorithms like Gerchberg Saxton. Figure 3.7 shows a

comparison of PA holograms and PO holograms. The superior quality to PA holograms both to PO and the Gerchberg-Saxton based PO is clearly visible, The PO hologram over saturates the edges of the logo seen in Fig 3.6. We can therefore infer that the amplitude modulation reduces the large amplitudes of high spatial frequencies in the reconstructed hologram. Gerchberg-Saxton based PO hologram do not have edge saturation issue, however they produce images with speckle like artifacts due to unwanted destructive interference.

Such high-fidelity holographic reconstructions are desirable for augmented reality applications and in this section, we propose a platform which demonstrates a three colour PA hologram. A single metasurface does not have enough degrees of freedom to accurately provide independent phase responses for more than two wavelengths, it is therefore not possible to achieve the more difficult task of providing simultaneous amplitude and phase masks at RGB wavelengths. We therefore utilize spatial multiplexing where we create three spatially separated PA hologram for each of the three colours that comprise red, green and blue wavelengths and use a second metasurface at a different plane that can combine the individual channels to form a single RGB hologram. A schematic of such a device is shown in Fig. 3.8. Each PA hologram representing a single colour channel has an additional phase tilt added to it complex phasor response such that after propagating a fixed distance the holograms formed by the three colours spatially overlap at an intermediary plane. At this plane, we can impose a metasurface corrector plate that imposes a wavelength selective beam deflector functionality to correct for the tilt of each wavelength channel. Hence any observer looking at this doublet device head on will only observe the combined RGB hologram.

We computationally derive the correct phase and amplitude response for each channel by first picking a desired focal plane where we would like to form the hologram scene. Then we separate the scene into red, green and blue channels. Each channel is then separately backpropagated using Fourier domain methods to an intermediary grating plane. At this plane, we

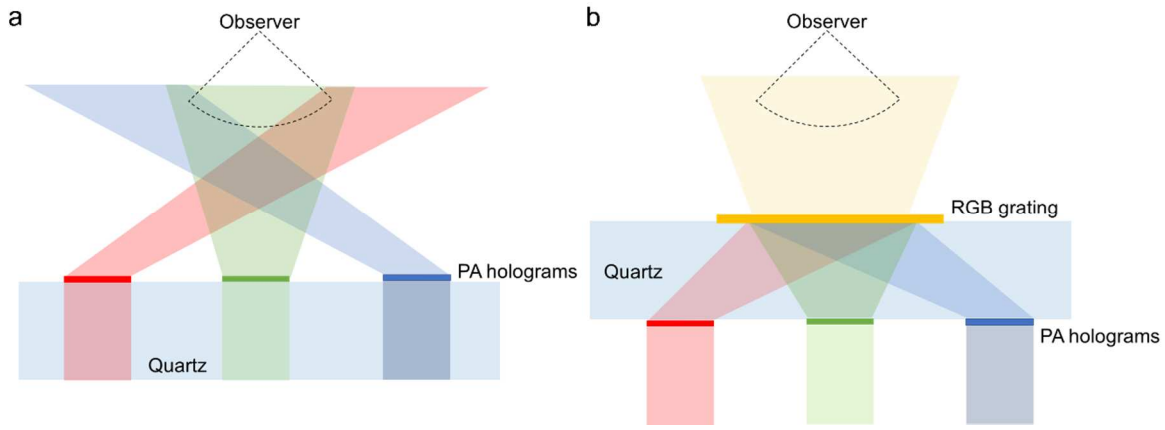

Figure 3.8: RGB phase and amplitude doublet hologram. (a) Schematics of the device with spatially separated phase and amplitude holograms for individual red, green and blue channel. An observer will observe different channels based on his viewing angle and only for certain viewing angle will some portions of the individual RGB channels overlap. (b) Schematics of the device with spatially separated phase and amplitude holograms for individual red, green and blue channel on one side of the quartz substrate and a wavelength selective grating that corrects for the deflection angle of each channel to send the mixed channel signal to an observer. With this doublet RGB channels are correctly overlap and the observer will see the desired scene as intended.

judiciously pick a beam deflection angle for individual channel such that at the metasurface hologram plane, the complex transmission function of the three wavelength channels are entirely spatially separated. The complex field at this plane is then backpropagated to the metasurface hologram plane taking into account the tilted wavefronts. We should then have three independent complex transmission function for each wavelength at the hologram and their corresponding spatial extent and a wavelength selective RGB grating based on the chosen deflection angles.

Using the framework described above, we simulate an RGB phase and amplitude hologram doublet for visible wavelengths of 430 (blue), 530 (green) and 620 (red) nm using the TiO_2 on quartz platform discussed in section 3.1. Each metaunit has the structure shown in Fig 3.5b where the period is chosen to be 280 nm and the height of TiO_2 pillars are 860 nm. The wavelength selective deflector is designed in a manner similar to the RGB metalens described in the previous section. Thus, this element is polarization insensitive and does not change state of polarization of light passing through it. Figure 3.9a shows our target RGB image that we would like

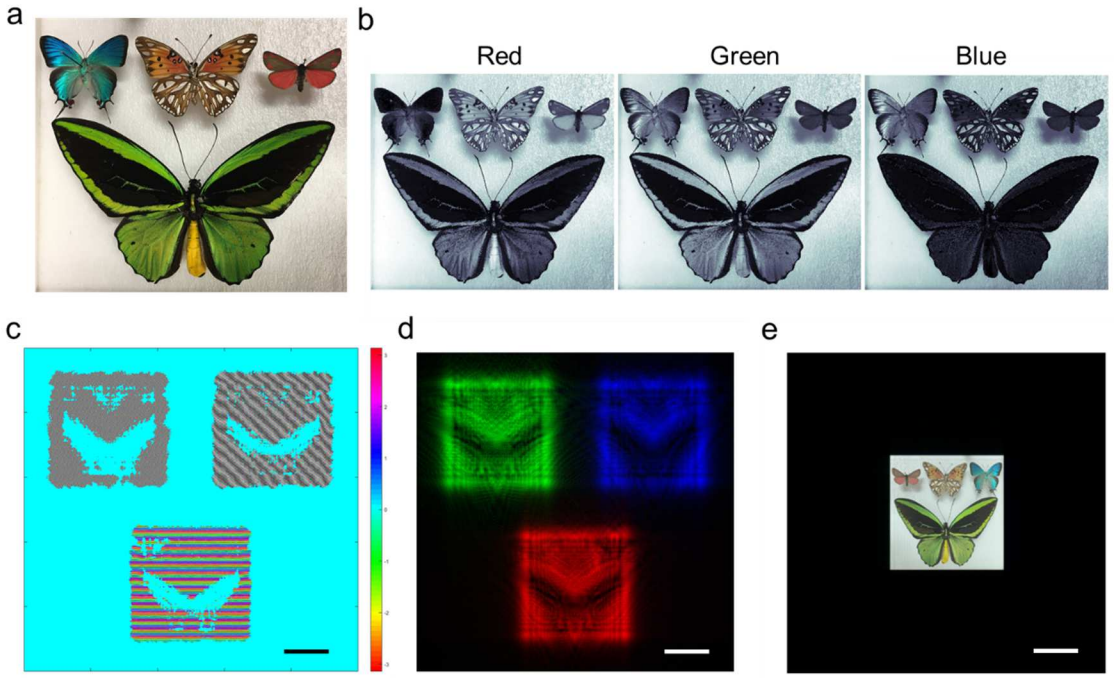

Figure 3.9: Simulation of RGB phase and amplitude hologram. (a) Image of colourful butterflies as target object. (b) Red, green and blue channels that forms the image in (a). (c) Spatially varying phase for three channels obtained from backpropagation. (d) Corresponding amplitude mask. (e)Reconstructed hologram of target in (a). Scale bar: 100 μm.

to reconstruct using our doublet platform. The image has all three colours in the RGB spectrum and subtle texture that is difficult to reproduce with phase only holograms. The amplitudes of individual channels are shown in Fig. 3.9b. The background colour of white also makes it important to have high fidelity reconstruction to avoid large noise contribution from it. Figure 3.9(c,d) shows the required amplitude and phase masks for the three wavelengths. The spatial extent of the three holograms is determined by the final size of the image we would like to reconstruct and the individual beam deflection angle for each colour. The object size is set to 250 μm and is 900 μm away from the metasurface hologram plane. Beam deflection angles of (0 $^{\circ}$,18°), (18°, -18°) and (-18°, -18°) corresponding to deflection in x and y direction are chosen for red, green and blue wavelengths respectively. Finally, we reconstruct the hologram using Fourier domain methods propagating the incident light at all RGB wavelengths through both the metasurface elements to the desired imaging plane with the result shown in Fig. 3.9e. We can see that the original image is reconstructed faithfully with no speckle artifact and correct amplitude distribution. In addition, we

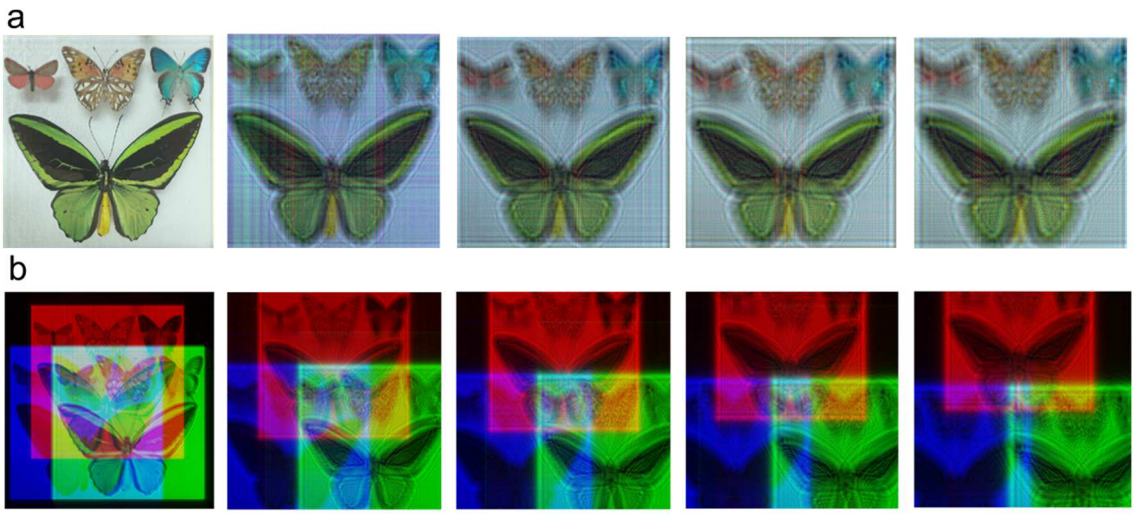

Figure 3.10: Importance of wavelength selective deflector. Image seen by the observer when focusing at planes away from the designed focal plane of the hologram with (a) and without the wavelength selective deflector (b). From left to right, the focal planes are 0,100,150,250,300 μm away from the design focal plane.

show in Fig. 3.10 why the wavelength selective deflector is important for combining the three channels correctly. It shows that away from the focal plane, the holographic image merely looks out of focus as expected when the corrector is used as seen in Fig. 3.10a, where the simulated images are shown when the observer focuses at distances 100,150,250 and 300 μm away from the designed focal plane. In comparison, without the deflector, the three channels do not combine correctly and continue to spatially separate at distances further away from the design focal plane in addition to displaying defocus behavior as seen in Fig. 3.10b.

To conclude, we have demonstrated a method to realize three colour phase and amplitude hologram that can reconstruct the desired objects with very high fidelity with no speckle or grainy texture that is often associated with phase only algorithms that are based on iterative methods. By utilizing two metasurface elements and simple backpropagation method we can easily define complex transmission function for different colour channels without relying on optimization processes. Further improvement in design maybe possible by exploring additional degrees available by making the second element also based on geometric phase. We are actively pursuing experimental verification of such device for the visible wavelength range using the TiO_2 metaunits.

Chapter 4: Dispersion Engineered Metasurfaces

The material in this chapter is reproduced from [160].

4.1 Chromatic Aberration Correction in Metasurfaces

Metasurfaces offer a unique platform to precisely control optical wavefronts and enable the realization of flat lenses, or metalenses, which have the potential to substantially reduce the size and complexity of imaging systems and to realize new imaging modalities. However, it is a major challenge to create achromatic metalenses that produce a single focal length over a broad wavelength range because of the difficulty in simultaneously engineering phase profiles at distinct wavelengths on a single metasurface. For practical applications, there is a further challenge to create broadband achromatic metalenses that work in the transmission mode for incident light waves with any arbitrary polarization state. We developed a design methodology and created libraries of meta-units—building blocks of metasurfaces—with complex cross-sectional geometries to provide diverse phase dispersions (phase as a function of wavelength), which is crucial for creating broadband achromatic metalenses. We elucidated the fundamental limitations of achromatic metalens performance by deriving mathematical equations that govern the tradeoffs between phase dispersion and achievable lens parameters, including the lens diameter, numerical aperture (NA), and bandwidth of achromatic operation. We experimentally demonstrated several dielectric achromatic metalenses reaching the fundamental limitations. These metalenses work in the transmission mode with polarization-independent focusing efficiencies up to 50% and continuously provide a near-constant focal length over λ = 1200–1650 nm. These unprecedented properties represent a major advance compared to the state of the art and a major step toward practical implementations of metalenses.

Expanding the control of optical wavefronts is the promise of a class of engineered two-dimensional materials called “metasurfaces” [2,14,23,39,109,110]. Composed of subwavelength scatterers with tailored optical responses, or “meta-units”, a metasurface can realize a variety of device functions [3,11,12,15,21,25,47,50,51,106,111–120] with a completely flat form-factor if the library of meta-units is sufficiently diverse. The flat formfactor is a particular advantage for devices such as lenses, enabling compact imaging systems to be fabricated with complementary metal oxide semiconductor (CMOS)- compatible processes. However, as with lenses based on bulk materials, metasurface lenses, [13,16,28,29,32,33,111,121–127] or “metalenses”, must be designed to minimize aberrations for use in high-performance imaging systems. Recent work [128,129] has substantially reduced monochromatic aberrations by using two parallel metasurfaces, yielding compound metalenses with a large field of view. Initial efforts to correct chromatic aberrations inherent to diffractive optical systems have led to demonstrations of multiwavelength metalenses. [130–133] More recent endeavors have focused on extending the correction to a continuous range of wavelengths but have been limited to reflective lenses, [134–137] polarization-dependent focusing, [136–138] and/or limited operation bandwidths. [134,135] Here we introduce a CMOS-compatible platform achieving diffraction-limited, polarization-independent focusing in the transmission mode across a broad bandwidth (up to $\Delta\lambda = 450$ nm) in the near-infrared wavelength range. We clarify the role of the spectral degree of freedom, [130,139] $C(\omega)$, which determines the reference phase at each frequency. We incorporate this understanding into a framework for dispersion-engineered metalenses that maps the design challenge onto filling a parameter space we call “phase-dispersion” space. We introduce novel meta-unit geometries that fill this space to a much greater degree than conventional meta-unit geometries. Using this new framework, we explore the fundamental limitations of chromatic aberration correction in metalenses and experimentally implement several metalenses reaching these limits. Chromatic dispersion is the dependence of focal length on the wavelength of light. Conventional, bulky lenses are based on refraction and exhibit positive dispersion (higher frequencies have smaller focal lengths). Diffractive focusing elements (such as Fresnel zone plates) exhibit the opposite (negative) dispersion. [140] In imaging systems, both types of dispersion lead to a degradation of image

quality due to blurring, an effect known as chromatic aberration. In both schemes, chromatic aberration correction can be achieved by careful design of a composite system of numerous optical elements, with the drawbacks of increased complexity, size, weight, and cost. Diffractive lenses have an advantage over refractive lenses in that they are flat and lightweight and can be fabricated with conventional nanofabrication techniques at low cost. However, these lenses have a much lower focusing efficiency due to the presence of high diffractive orders. Metalenses can be thought of as diffractive lenses with only one diffractive order, which eliminates this disadvantage while inheriting all the advantages of a conventional diffractive element over their bulky, refractive counterparts. Furthermore, the meta-units comprising metalenses are vastly more tailorable than those that make up simple diffractive elements (e.g., gratings), opening up the possibility to correct chromatic aberration in a single optical element.

4.2 Theory

In its most general form, a broadband achromatic metasurface presents a daunting challenge. Each meta-unit must be designed to simultaneously satisfy the phase requirement at all design wavelengths. Since the phase profiles for each frequency are potentially entirely independent, each meta-unit should provide a unique phase response (never to be re-used elsewhere in the metasurface). The size of the meta-unit library will therefore generally be equal to the number of elements of the metasurface. This fact compels the careful, joint consideration of meta-unit library design combined with the optical functionality desired. For converging achromatic metalenses, the spatial and spectral phase profiles follow a simple relation up to a spectral degree of freedom, C(ω):

$$\phi(r,\omega) = -\frac{\omega}{c}\left(\sqrt{r^2+f^2}\right) + C(\omega), \qquad (4.1)$$

where f is the focal length, r is the radial position, c is the speed of light, and ω is the angular frequency. The conventional choice is $C(\omega) = \frac{\omega}{c}f$, which renders the required phase 0 for all frequencies at the center of the lens (r = 0), convenient and intuitive option. Figure 4.1 summarizes the difference between the conventional design approach, which achieves focusing with chromatic

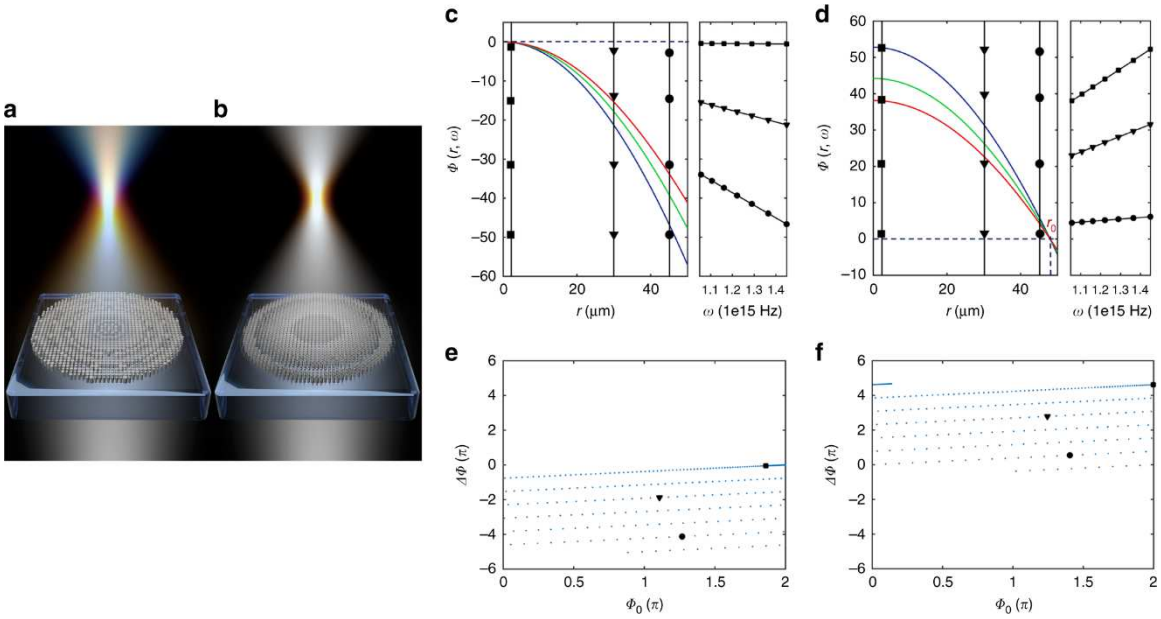

Figure 4.1 (a) Schematic of a monochromatic metalens composed of simple cylindrical meta-units, showing diffractive dispersion (focal length proportional to frequency). (b) Schematic of a broadband achromatic metalens composed of meta-units with complex cross sections, showing dispersionless focusing. c Spatial (left panel) and spectral (right panel) phase profiles required for a sample achromatic metalens (radius of 50 μm, focal length of 100 μm, operating in the wavelength range of λ = 1.3-1.8 μm) designed with the conventional choice of $C(\omega) = \frac{\omega}{c} f$. Three different frequencies are represented by three colors, and three positions are represented by different symbols. (d) Similar diagrams as in (c) but for our choice of $C(\omega) = \frac{\omega}{c}\sqrt{r_0^2 + f^2}$. (e, f) Requirements of meta-units for the metalens in the phase-dispersion space, where ϕ0 is the phase of the smallest frequency and the dispersion $\Delta\Phi = \frac{d\phi}{d\omega}\Delta\omega$ for a given bandwidth $\Delta\omega$ is the difference in phase between the largest and smallest frequencies.

aberration (Fig. 4.1a), and a novel design approach introduced herein, which produces dispersionless focusing (Fig. 4.1b). Figure 4.1c depicts the required spatial phase profiles based on the conventional choice for three select frequencies, as well as the spectral phase profiles (phase dispersion) at three selected positions along the metalens. We propose a generalized choice of

$$C(\omega) = \frac{\omega}{c}\sqrt{r_0^2 + f^2} + C_0, \qquad (4.2)$$

which makes the required phase $\phi(r_0, \omega) = C_0$ for all frequencies at the reference position r = r0. Figure 4.1d depicts the equivalent phase profiles of Fig. 4.1c for comparison. To understand the

impact of this choice, we first note that Eq. 4.1 is a simple linear function with respect to frequency. This feature suggests parameterizing the spectral phase required at each position as

$$\phi(r,\omega) = \phi_0(r) + \frac{d\phi}{d\omega}(r)(\omega - \omega_0), \qquad (4.3)$$

where $\phi_0(r)$ is the phase at a reference frequency ω_0, and $\frac{d\phi}{d\omega}(r)$ is the dispersion required at that frequency. In other words, a given meta-unit to be placed at position r can be described by two parameters: phase, ϕ_0, and dispersion, $\frac{d\phi}{d\omega}$. This aspect motivates the exploration of both meta-unit libraries and the choice of C(ω) in a parameter space defined by these two quantities, which we call "phase-dispersion" space. At each position on a metalens, Eq. 4.1 specifies the required values of phase and dispersion relative to a reference phase and a reference dispersion set by C(ω). These requirements can be plotted in the phase-dispersion space to visualize the extent of parameter space that a meta-unit library must fill to create the metalens (Fig. 4.1e, f). Figure 4.2 complements Fig. 4.1 by summarizing the area in the phase-dispersion space achievable by our meta-unit libraries. Figure 4.2(a–c) shows three meta-unit libraries based on dielectric pillars of a variety of cross-sectional shapes, and Fig. 4.2(d–f) maps the coverage of these libraries in the phase-dispersion space. Note in particular that all values of dispersion are positive, rendering the conventional choice of $C(\omega) = \frac{\omega}{c} f$ incompatible, as it prescribes only negative values of dispersion relative to the center of the metalens (Fig. 4.1e). In contrast, the proposed form of C(ω) prescribes positive values of dispersion by setting the reference as a position r0 (Fig. 4.1f and Supplementary section 4.2S1 and 4.2S2). The dielectric libraries can now match the required phase over a continuous bandwidth for positions r < r0 but not outside of that domain. This suggests making r0 the radius of the metalens, which fixes the dispersion required at the edge of the metalens $\frac{d\phi}{d\omega}\Big|_{\min}$ as zero and causes the dispersion to increase toward the center of the lens. Consequently, the dispersion required at the center of the lens $\frac{d\phi}{d\omega}\Big|_{\max}$ monotonically increases with metalens radius. The range of phase dispersion, $\Delta\Phi' = \left(\frac{d\phi}{d\omega}\Big|_{\max} - \frac{d\phi}{d\omega}\Big|_{\min}\right)\Delta\omega$, covered by a meta-unit library therefore limits the maximum radius R_{max} of an achromatic metalens that can be achieved with that

library. Specifically, this limitation is given by the following relation (details in Supplementary section 4.2S3):

$$R_{max} \leq \frac{\Delta\Phi' \, c}{\Delta\omega\left(\frac{1}{NA} - \sqrt{\frac{1}{NA^2} - 1}\right)}, \qquad (4.4)$$

which simplifies to

$$R_{max} NA \Delta\omega \leq 2c\Delta\Phi', \qquad (4.5)$$

when numerical aperture *NA*<<1.

Equation 4.5 imposes the tradeoffs in this design problem and indicates that metalenses with a larger diameter, higher NA, and/or broader operational bandwidth, $\Delta\omega$, require a larger $\Delta\Phi'$ and therefore a more diverse meta-unit library. The challenge, then, is to populate our library with meta-units with the largest range of dispersive responses possible within a fabrication scheme. To meet this challenge, we employ a dielectric metasurface platform of amorphous silicon nanostructures on a quartz substrate for proof-of-principle demonstrations. We model meta-units operating in transmission mode as dielectric waveguides with frequency-dependent effective refractive indices, $n_{eff}(\omega)$ (see Supplementary section 4.2S4). For each frequency, $n_{eff}(\omega)$ is calculated by eigenmode analysis on a finite difference grid and recorded for each choice of meta-unit cross-sectional shape. The phase is then obtained by an analytical thin film interference model with the meta-unit layer having an index of $n_{eff}(\omega)$ and thickness of H. This technique differs from previous approaches [134,135] that rely on sharp resonances exhibited by infinitely periodic meta-units (see Supplementary section 4.2S5). Figure 4.2a shows the first generation of our meta-unit library, called Generation 1A, with a thickness of H = 800 nm. Three archetypical cross sections are used: singular pillars, annular pillars, and concentric pillars. Each archetype is parameterized by the relevant radii and therefore represents a subclass of meta-units. It is evident that each subclass characteristically fills a different area of the phase-dispersion space (Fig. 4.2d). In particular, singular pillars (the conventional choice for dielectric meta-units) provide the highest dispersion for each phase value. However, this approach is limited to a singular value of dispersion for each phase, suggesting that the conventional meta-unit library composed of only this subclass

is a poor choice. Annular pillars allow for varied and slightly lower values of dispersion for each phase in comparison, while concentric pillars allow for even lower values of dispersion (Fig. 4.2d). Together, the meta-unit library fills an appreciable area of the phase-dispersion space. The extended coverage offered by these new archetypes can be understood as structural dispersion engineering [141]. High-dispersion meta-units (such as singular pillars) retain more short-wavelength light within the silicon compared to longer-wavelength light; in contrast, low dispersion meta-units (such as concentric pillars) retain nearly the same amount of short- and long-wavelength light within the silicon, acting similar to dispersionless effective media (mode profiles of sample meta-units are provided in see section 4.2S4). Further improvement of the coverage of the phase dispersion space, in particular, the extent of $\Delta\Phi'$, requires an increase in the height of the meta-units. Figure 4.2b shows meta-unit library Generation 1B. Its cross-section archetypes are identical to those of Generation 1A, but they differ in height, H = 1400 nm. A comparison of Fig. 4.2d, e reveals that taller meta-units greatly expand the coverage of the phase-dispersion space, at the cost of increased fabrication challenge. Figure 4.2c depicts meta-unit library Generation 2. This library has the same height as Generation 1B but has fourfold symmetry rather than rotational symmetry. This reduction of symmetry allows for additional subclasses not available in rotationally symmetric schemes without sacrificing polarization-independent performance. In particular, we explore crosses and inscribed crosses as two additional archetypes. The former more densely populates the medium-high dispersion range, while the latter extends the lowest dispersion range at large phases (acting more like an effective material than any other archetype in that phase range) (Fig. 4.2f).

4.3 Results and Discussion

To explore the impact of meta-unit libraries on metalens performance, we fabricated and characterized metalenses using all three generations of libraries (the parameters of the fabricated

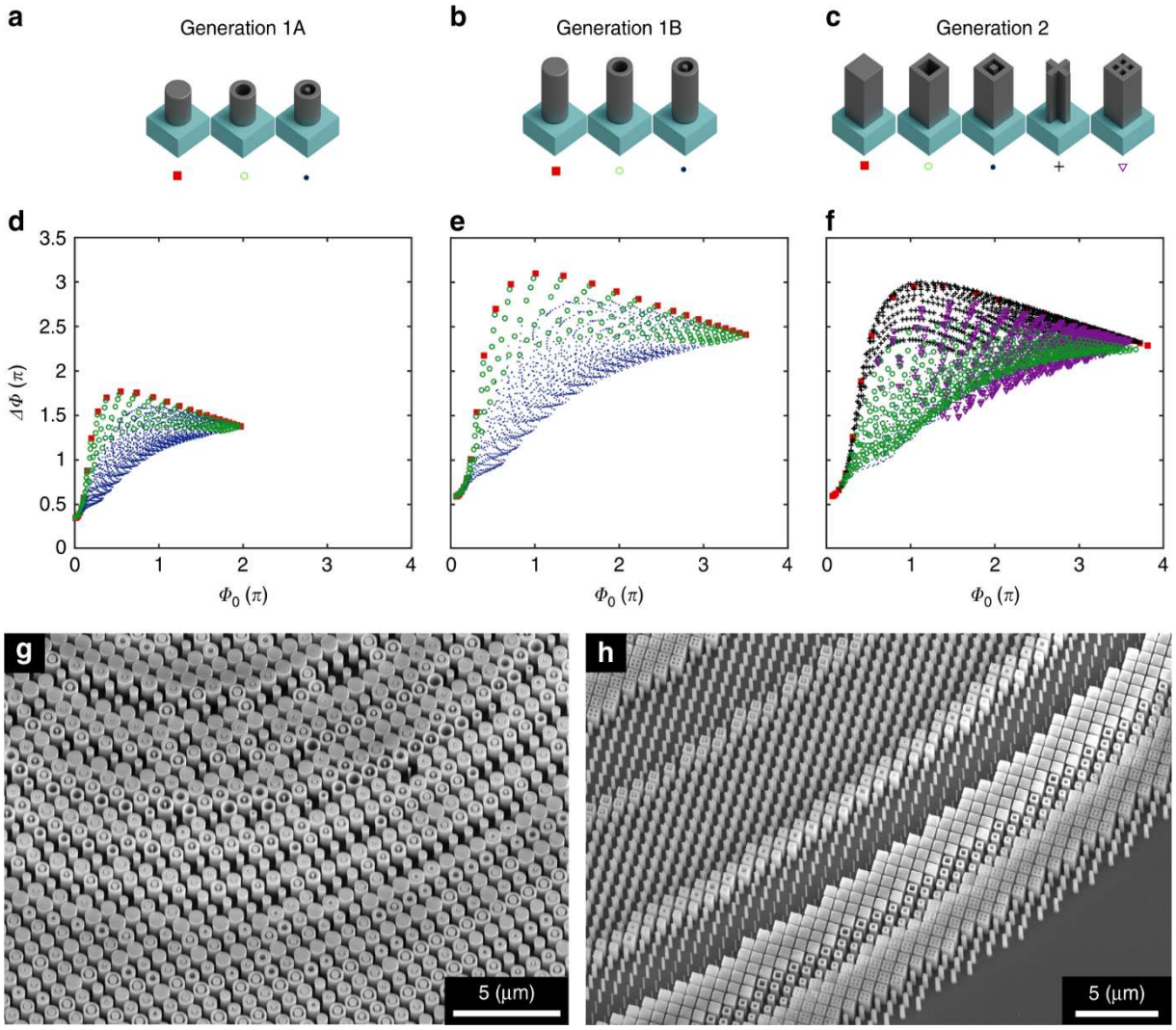

Figure 4.2: (a–c) Schematics showing meta-unit archetypes, each representing a subclass of meta-units composed of the archetype's basic shape but with varying in-plane geometrical parameters (e.g., inner and outer radii of annular pillars). (d) Calculated phase, Φ_0, of the lowest frequency (or largest wavelength, λ = 1.6 µm) and dispersion, $\Delta\Phi = \frac{d\phi}{d\omega}\Delta\omega$, for the chosen bandwidth $\Delta\omega$ (i.e., λ = 1.2–1.6 µm) of each meta-unit used in the Generation 1A library: singular pillars (red squares), annular pillars (green circles), and concentric rings (blue dots). The meta-units are composed of silicon, with a height of 800 nm. Note the expansive coverage of phase-dispersion space compared to that obtained by employing only the conventional choice of singular pillars. (e) Calculated phase and dispersion for the Generation 1B library, differing from the Generation 1A library only by increasing the height to 1400 nm. The range of dispersion achieved is nearly doubled. (f) Calculated phase and dispersion for the Generation 2 library, keeping the same height as the Generation 1B library but switching to archetypes with four-fold symmetry instead of rotational symmetry. This change expands the number of archetypes to include crosses (black crosses) and inscribed crosses (purple triangles). The two orange curves define the upper and lower boundaries that can be reached by dielectric meta-units, found by an exhaustive computational search (see Supplementary section 4.2A8). Our choice of meta-unit cross sections fully populates the possible area in the phase-dispersion space, while being feasible for nanofabrication. (g, h) Scanning electron microscope images of fabricated metalenses using Generation 1A and Generation 2 meta-units, respectively.

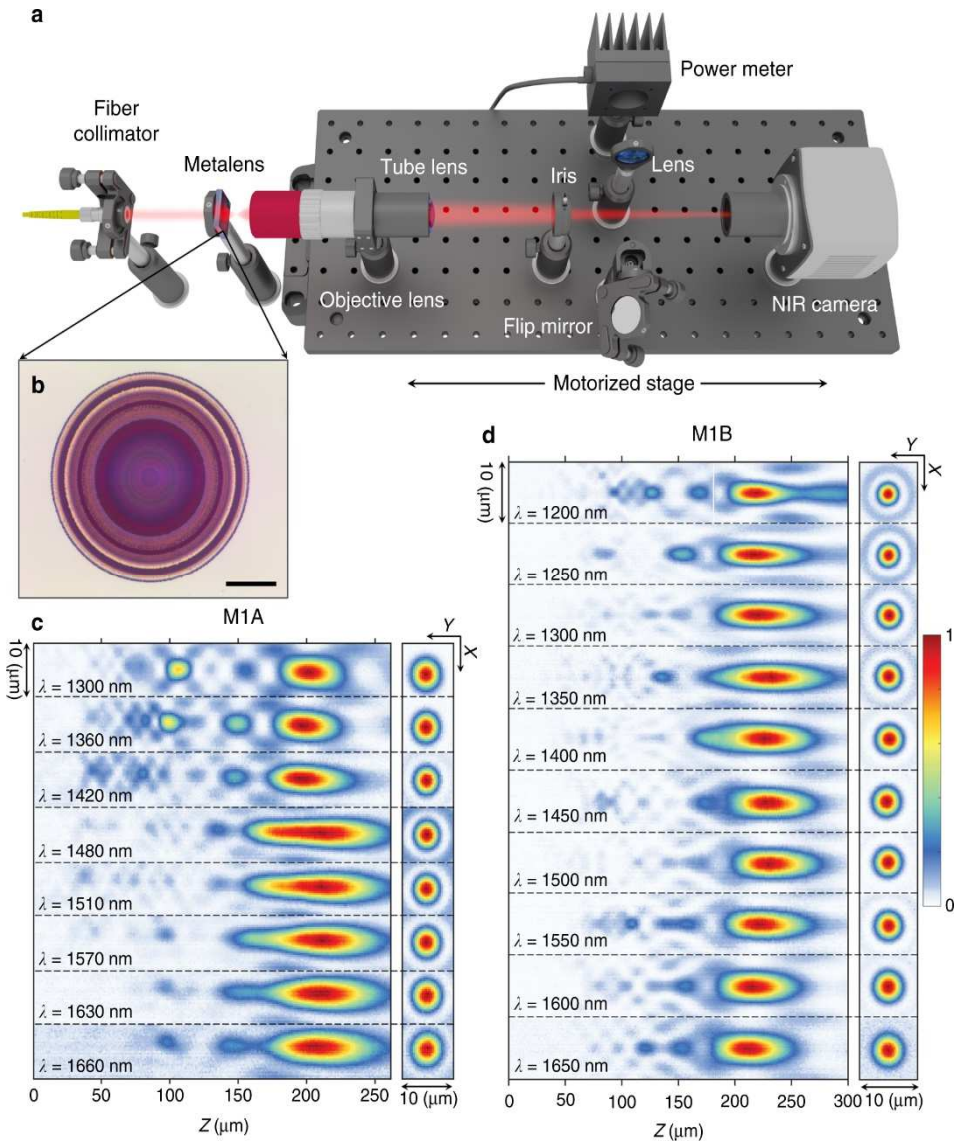

Figure 4.3: (a) Schematic depicting the optical setup. The optics for mapping the 3D far-field of the metalenses are mounted on a motorized stage. A flip mirror allows light to pass from a target focal plane to a power meter for efficiency measurements. (b) Optical image of a sample metalens. Scale bar: 25 μm. (c) Measured far-field intensity distributions of metalens M1A, composed of Generation 1A meta-units and with diameter $D = 100$ μm and target focal length $f = 200$ μm, corresponding to NA = 0.24. Measured normalized intensity distributions in the axial plane (x - z cross section) are shown for select wavelengths spanning from 1300 to 1660 nm. The x-y cross sections are shown at the target focal plane for each wavelength. (d) Corresponding experimental results for metalens M1B, composed of Generation 1B meta-units, showing substantially suppressed parasitic focal spots, little elongation of the depth of focus as observed in (c), and larger operational bandwidth

metalenses using a standard electron beam lithography, lift-off, and etch procedure (Materials and methods section). Scanning electron microscope images of two sample fabricated metalenses are

shown in Fig. 4.2(g, h). Using the custom-built setup shown in Fig. 4.3a, we characterized the three-dimensional (3D) intensity distribution of light exiting the fabricated metalenses. Using the Generation 1A library, we realized an achromatic metalens, M1A, with a diameter of 100 μm, designed focal length of 200 μm (NA ≈ 0.24), and operational bandwidth of λ = 1300–1650 nm. The measured intensity distributions in the focal (x–y cross section) and axial (x–z cross section) planes at different wavelengths for M1A are plotted in Fig. 4.3c. From the axial intensity distributions, we can see that the chromatic aberration is significantly reduced across the entire operating bandwidth, with the focal planes for all wavelengths lying very close to one another. It is important to stress that this is a continuous aberration correction over the entire designed wavelength range, not just at the selected wavelengths. However, we can see parasitic focal spots for wavelengths shorter than 1400 nm and an elongation of the depth of focus (DOF) for wavelengths longer than 1450 nm. We attribute these features to the limited coverage of the phase-dispersion space provided by the Generation 1A library (Fig. 4.2d) for this lens. We therefore designed and fabricated metalens M1B, with the same size and NA as M1A, using the taller meta-units from the Generation 1B library. The corresponding measured focal and axial intensity distributions are plotted in Fig. 4.3d and show substantially suppressed parasitic focal spots and little elongation of the DOF. The wavelength range over which the chromatic aberration is corrected is also expanded to λ = 1200–1650 nm, a 100- nm improvement over the operational bandwidth of M1A. The combination of size, NA, and bandwidth of M1B reaches the fundamental limitation described by Eq. 4.5 (Fig. 4.4a). The predicted benefits (see Supplementary section Figure 4.2S4) of expanded coverage of the phase-dispersion space are clearly demonstrated, despite the increased challenges involved in the fabrication. We believe that this is the best reported result for a broadband polarization-independent achromatic metalens working in transmission mode.

Using the Generation 1B library, we created metalens M2, with a diameter of 200 μm and a focal length of 800 μm (NA ≈ 0.13), with chromatic aberration correction over the same wavelength range of 1200–1650 nm (Fig. 4.4b). This larger lens (marked by a black square in Fig. 4.4a) still falls within the limits set by the phase-dispersion coverage of our Generation 1B library

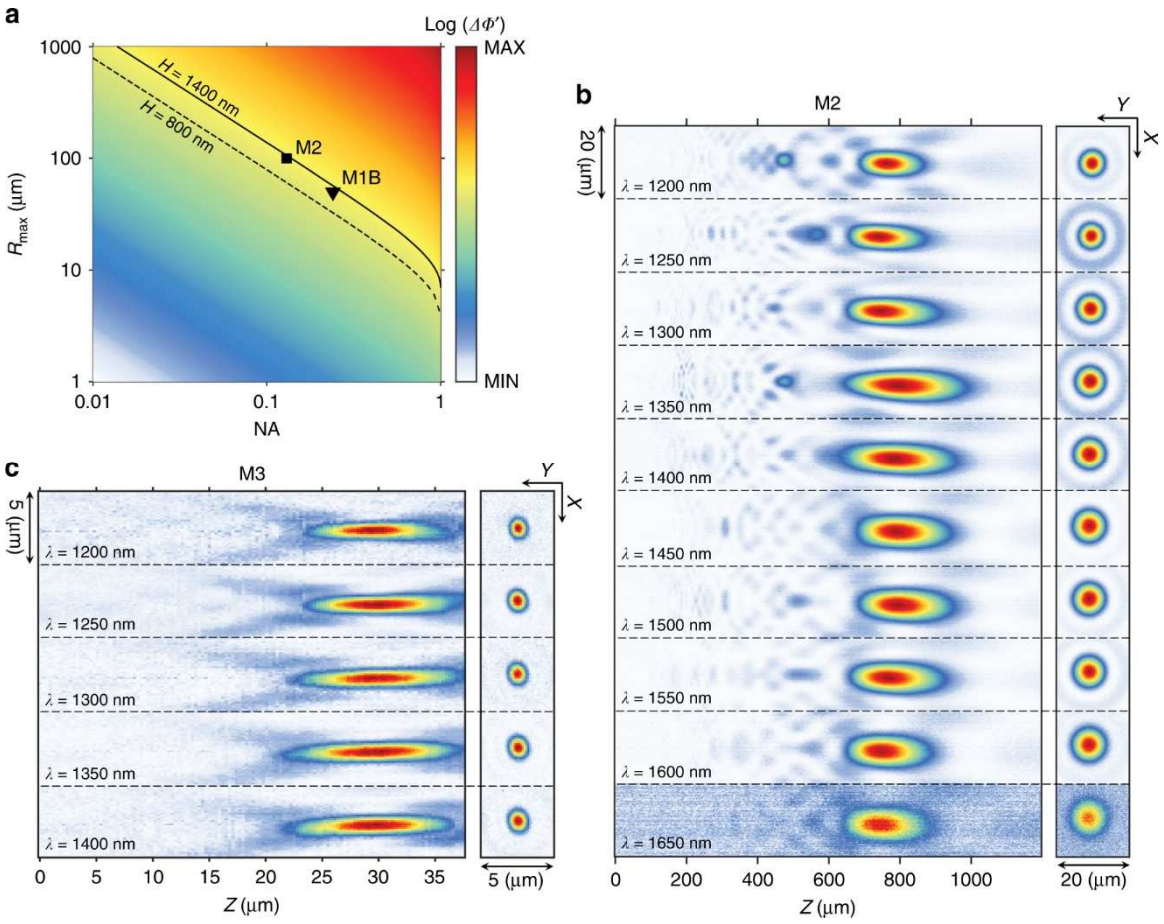

Figure 4.4: (a) Diagram showing that the range of dispersion, $\Delta\Phi' = \left(\frac{d\phi}{d\omega}\Big|_{\max} - \frac{d\phi}{d\omega}\Big|_{\min}\right)\Delta$, achieved by a meta-unit library sets an upper limit on the achievable combinations of NA and radius, R_{max}. In particular, the solid and dashed curves represent the limitations on achievable metalenses using the Generation 1B and 1A libraries, respectively. Two demonstrated metalenses M1B and M2, indicated in the diagram by triangle and square symbols, respectively, reach the fundamental limits. (b) Measured far-field intensity distributions for metalens M2 (D = 200 μm and NA = 0.12), implemented with the Generation 1B library. (c) Measured far-field intensity distributions for metalens M3 (D = 100 μm and NA = 0.85), implemented with the Generation 2 library.

and represents an alternative choice in the tradeoff between metalens size and NA described by Eq. 4.5. Increasing the NA of metalenses comes at a cost of the operational bandwidth. We used the Generation 2 library and demonstrated a high-NA metalens M3, with a diameter of 100 μm and a focal length of 30 μm (NA ≈ 0.88), with chromatic aberration correction over a reduced operational bandwidth of λ = 1200–1400 nm (Fig. 4.4c). Figure 4.5 summarizes important figures of merit, including the focal length, focusing efficiency, focal spot size, and Strehl ratio, for all of the

fabricated metalenses. Figure 4.5a shows focal plane intensity profiles at the selected wavelengths shown in Fig. 4.3d for metalens M1B; Fig. 4.5b shows corresponding horizontal and vertical cuts of the measured focal spots with an ideal Airy disk overlaid for comparison. The results show nearly diffraction-limited focal spots for all wavelengths with no obvious distortion. Figure 4.5c shows the measured focal lengths of the metalenses at sampled wavelengths, with the maximum shift from the mean focal length limited to 2–5% for the entire design bandwidth.

Measured focusing efficiencies, defined as the percentage of power incident on the metalens and transmitted through a circular aperture positioned on the focal plane of the metalens with a radius equal to a few times the full-width at half-maximum (FWHM) of the focal spot, are plotted in Fig. 4.5d. The efficiencies of our metalenses are not as high as those of the best monochromatic metalenses based on dielectric resonators [29,32,33,126] but are significantly higher than those of metalenses based on plasmonic scatterers [3,13,123,133,136] and recent reports of dielectric achromatic metalenses [134,135,137,138]. In all cases, sources of reduced efficiencies in achromatic metalenses include amplitude variations (not all meta-units have the same scattering efficiency), phase errors due to mismatch between the required and actual phase responses of the meta-units, nearest-neighbor effects (the optical response of a meta-unit is perturbed by adjacent meta-units, more pronounced for the taller library due to the increased interaction length), and fabrication errors (such as sidewall roughness and slope). In our transmission-mode metalenses, backscattering from meta-units can further reduce the overall efficiency. Another symptom of these errors is the presence of multiple parasitic focal spots, appearing in varying degrees in the fabricated devices but with significantly smaller intensity than the primary focal spots. These spots are commonly seen in recent achromatic metalens attempts, and the present results are of comparable magnitude to previous efforts.

Diffraction-limited focal spots are important for high performance imaging systems. We measured the FWHM of the focal spots of all of the metalenses at sampled wavelengths and compared them with the theoretical limit $\left(\sim \frac{\lambda}{2NA}\right)$. The results are plotted in Fig. 4.5e and show that

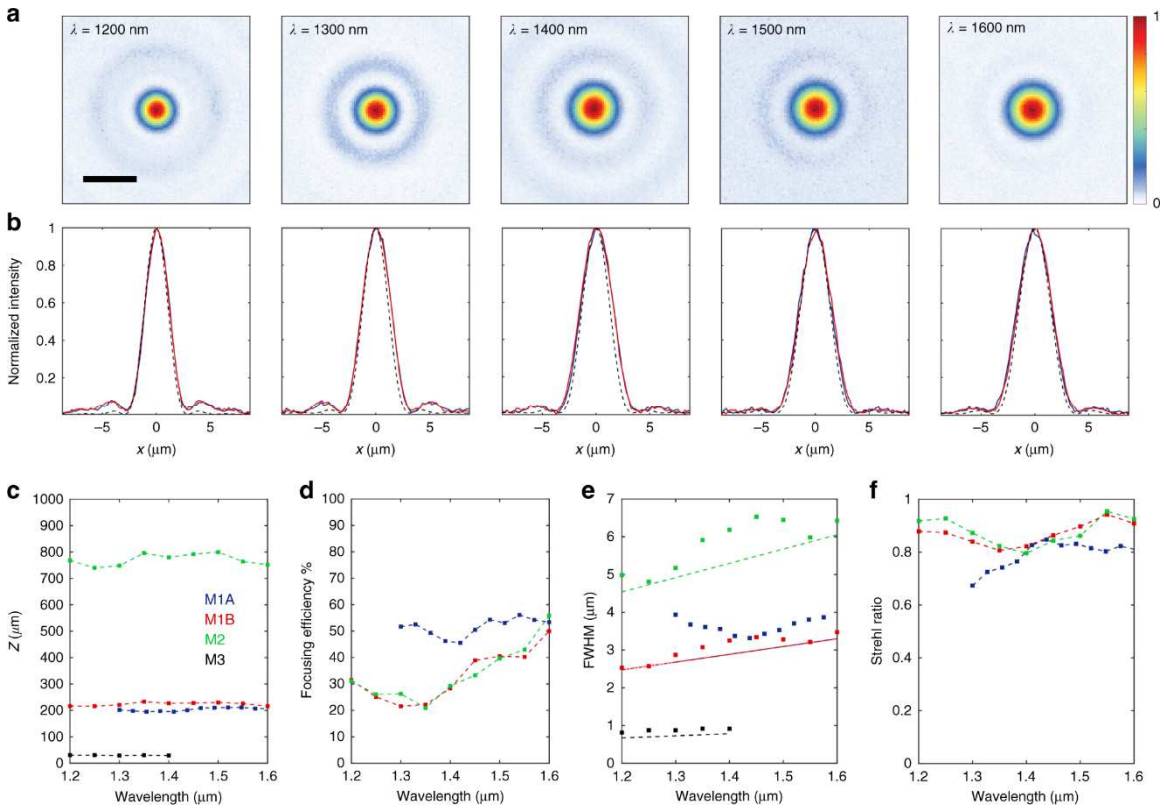

Figure 4.5: (a) Focal plane intensity distributions of metalens M1B (*D* = 100 μm and NA = 0.24) at select wavelengths. Scale bar: 5 μm. (b) Horizontal (blue curves) and vertical (red curves) cuts across the measured focal spots in (a) compared with an ideal Airy spot (black dashed curves). (c) Focal lengths as a function of wavelength for the four metalenses demonstrated. (d) Measured focusing efficiencies of the metalenses, excluding M3 because its NA exceeds that of the measurement setup. (e) Extracted FWHM of focal spots for the four metalenses. Straight lines represent the theoretical FWHM. (f) Calculated Strehl ratios for the metalenses, excluding M3 because Strehl ratio measurements are not applicable for high-NA lenses.

for all of the lenses based on the 1400-nm library, the focal spots are at or near the diffraction limit for the entire operational wavelength range of the lenses. The focal spots for M1A, which is based on the 800-nm library, are slightly larger than the diffraction limit for some wavelengths. The performance can be further quantified by measuring the Strehl ratio [127,128] of the focal spots. The calculated Strehl ratios for the entire bandwidth of metalenses M1A, M1B, and M2 are plotted

in Fig. 4.5f; the ratios are above 0.8 for M1B and M2 for all wavelengths, satisfying the condition for diffraction-limited focal spots.

We conclude with a discussion on the utility of the present work for compact imaging systems. We believe that a combination of the present framework with the approach of recent work on achieving wide-angle monochromatic imaging [128,129] can simultaneously reduce or eliminate chromatic and monochromatic aberrations, fully realizing the promise of metalenses. Our approach is equally capable of realizing diverging lenses (see Figure 4.2S8), which are also utilized in imaging systems. Additionally, a combination of several metalenses can substantially improve achromatic performance past the theoretical limitation of a singlet. For instance, stacking N achromatic metalenses would decrease the achievable focal length for the same diameter, bandwidth, and meta-unit library by approximately the same factor N (see Supplementary section 4.2S8 and Figure 4.2S6). Singlet metalenses merit consideration as stand-alone devices as well, despite their well-known off-axis aberrations. A singlet achromatic metalens is suitable for broadband collimation in a flat form-factor (a collimator does not have to operate off-axis). Such a metalens could be packaged on the end of fiber optics for broadband and compact functionality [142,143] Additionally, high-NA microlens arrays are of considerable interest for applications such as light-field cameras and CMOS camera sensors. We note that the present approach is directly applicable to other optical frequencies with a change of material platform. For instance, visible metalenses could be realized using TiO2 on quartz [32,33,134,138] or GaN on sapphire. [137] The magnitude of the refractive index, intrinsic material dispersion, and aspect ratio achievable in nanofabrication are important considerations for choosing a platform. A larger refractive index enables an increased diversity of optical response from structural dispersion engineering, and intrinsic material dispersion can add to structural dispersion to improve coverage of the phase dispersion space. For a given dielectric material, the ultimate limiting factor on metalens performance using the present approach is the height of the meta-units, which sets the maximum range of phase dispersion. Without incorporating plasmonic or Mie resonance or meta-units with anomalous dispersion, we believe that the meta-unit libraries presented here fully utilize the phase-dispersion variety within a given height (see Supplementary section 4.2S9 and Figure

4.2S7). For crystalline silicon, very high aspect-ratio structures are achievable, [144] motivating future work to improve on the performance demonstrated here. In conclusion, we have demonstrated continuous diffraction-limited achromatic focusing across a broad near-infrared bandwidth. In particular, our metalenses work in the transmission mode with incident light of any arbitrary polarization state, which is highly desirable for shrinking imaging systems. We introduced a clarifying framework for understanding the limitations on chromatic aberration correction and the tradeoffs therein and have developed an approach that jointly utilizes the spectral degrees of freedom in the lens phase profiles and the geometric degrees of freedom in the meta-units to create achromatic metalenses reaching these limits. We describe and employ a phase-dispersion space that proves integral to framing and solving this problem. Our experimental results validate this approach, and these new metalenses offer a novel method for achieving chromatic aberration correction across a continuous and broad bandwidth in compact imaging systems.

Supplementary section 4.1S: Methods

Error minimization during metalens design. The spectral degree of freedom, $C(\omega)$, has parameters r_0 and C_0 that can be used to best match a target metalens phase function with the available meta-unit library. In order to select the optimal meta-unit at each lattice point (x,y) of a metalens, we devise an algorithm that sweeps over possible combinations of r_0 and C_0, and determines the best possible set of meta-units for the metalens.

The figure of merit, FoM, used is the summation of phasor errors across all design wavelengths and lattice positions. The target phasor of a metalens is $A_t e^{i\phi_t(x,y,\lambda_j)}$, where A_t is a target amplitude (ideally set to 1, but in practice is set according to a typical transmittance value for the given meta-unit library, e.g., 0.75), and $\phi_t(x, y, \lambda_j | r_0, C_0)$ is the phase profile of the metalens given a value of r_0 and C_0. Each meta-unit has a simulated phasor $A_m(\lambda_j)e^{i\phi_m(\lambda_j)}$ stored in the

meta-unit library, and the difference (error) between the target phasor and meta-unit phasor is calculated at each (x, y, λ_j). The meta-unit with the minimal error summed across wavelengths is recorded as the best choice for that (x, y). The error of each optimal choice is summed across all points (x, y) and recorded as the FoM for that r_0 and C_0. The values of r_0 and C_0 corresponding to the smallest FoM are then chosen.

This error minimization algorithm minimizes errors for a specific set of discrete wavelengths (in practice, we select many closely spaced wavelengths, approximating a continuous spectrum). It takes into account deviations from linear phase response presumed under the phase-dispersion framework (which only strictly considers the lowest and highest frequencies and interpolates phase linearly in between), and straightforwardly includes simulated amplitude deviations from unity (variation in amplitude across a metasurface leads to high diffraction orders).

Metalens fabrication. Amorphous silicon films of thickness 800 or 1400 nm are deposited by plasma-enhanced chemical vapor deposition at 200˚C on 500-μm fused quartz substrates. A JEOL JBX-6300FS electron beam lithography apparatus is used to define the metasurface lens pattern on a doublelayer resist (PMMA 495k A4 and 950A2) with a dose of 770 μC/cm2 at a current of 200 pA. A 20-nm layer of ESpacer is spun on top of the double-layer resist to avoid the electron charging effect. After the resist is developed in IPA:DI (3:1) for 2 min at 5˚C, 20 nm of aluminum oxide is deposited using electron beam evaporation and lifted off in Remover 1165. The metasurface lens pattern is transferred to amorphous silicon films by inductively coupled plasma (ICP) etching in a mixture of SF6 (40 sccm) and O2 (16 sccm) at −100˚C with an ICP power of 800 W and an RF power of 40 W.

Optical characterization. In the experimental setup (Fig. 3a), a collimated laser beam with a tunable wavelength is incident on the metalens, and the 3D far-field of the lens is measured by acquiring a stack of 2D images at different distances from the lens. The tunable laser beam is

generated by passing the emission from a supercontinuum laser source (NKT SuperK Extreme) through a monochromator (Horiba iHR550). Light exiting the monochromator is coupled into a single-mode fiber (Thorlabs P1-980A-FC) and then collimated using an adjustable aspheric fiber collimator (Thorlabs CFC-5X-B) with an anti-reflection coating for a wavelength range of 1050–1620 nm. The imaging optics for monitoring the far-field of the metalenses consist of a ×100 objective (Mitutoyo Plan Apo NIR), a tube lens (Thorlabs AC254-200-C) of focal length 200 mm, and an InGaAs camera (Princeton Instruments Nirvana 640ST), which are mounted on a motorized stage.

Using the stage, the device plane is brought to focus on the camera. Then, the stage is moved toward the focal plane of the metalens in predefined increments (typically 1 μm). At each position, the transverse intensity distribution is captured by the camera for desired wavelengths by changing the angle of the grating in the monochromator. In this way, the 3D far-field of the metalens is measured. The longitudinal intensity distribution is then created for each wavelength by splicing the 3D intensity distribution along the axis of the metalens.

For efficiency measurements of the metalenses, a flip mirror and an iris are introduced before the InGaAs camera. The power transmitted through a metalens is measured by focusing the camera on the device plane and closing the iris to match the diameter of the metalens. The power is then passed to a power meter (Thorlabs SM05PD5A) using the flip mirror and a lens with a 40-mm focal length. The incident power is measured by focusing the camera on an unpatterned region of the quartz substrate and recording the power with the iris set to the same diameter as the metalens. The ratio between transmitted and incident power defines the transmission efficiency. To measure the focusing efficiency, the motor is first moved to the focal plane of the metalens and the iris is closed such that it corresponds to three to five times the FWHM of the focal spot. Then, the light is passed to the power meter. The ratio between the measured focused power and the incident power defines the focusing efficiency.

To determine any chromatic aberration in our imaging optics, we image gold nanostructures at different wavelengths by bringing them to focus using the motorized stage and recording the position of the stage for each wavelength. In this way, we ascertain the chromatic aberration of our imaging optics; this information is used to correct the 3D intensity measurements of the metalenses.

Supplementary section 4.2S. Supplementary Information for Chromatic aberration correction in metasurfaces

4.2S1. Geometric interpretation of the spectral degree of freedom

A typical approach to derive the required phase function of a metasurface involves the holographic principle. In the case of a metalens, this corresponds to placing a dipole source at the focal spot and propagating the emitted spherical wave to the plane of the metasurface. This process can be visualized as in Fig. 4.2S1a, wherein a black semi-circle represents a reference wavefront of the dipole centered at the focal point, f. The phase function is related to the segment, d, of ray ρ, spanning from position r to the semi-circle,

$$d = \sqrt{r^2 + f^2} - f.$$

It is apparent that a phase *advance* (a negative value) proportional to the propagation phase across a distance d must be added at each position r. That is, at position r the hemispherical wavefront must jump *ahead* a distance d in order to match the planar metasurface. The phase function is therefore easily written down as:

$$\phi(r, \omega) = -k_0 d = -\frac{\omega}{c}\left(\sqrt{r^2 + f^2} - f\right),$$

which is recognizable as the conventional form of the phase function. The natural dispersion of this form is seen by the dashed red, green, and blue wavefronts in Fig. 4.2S1a. The wavefronts for

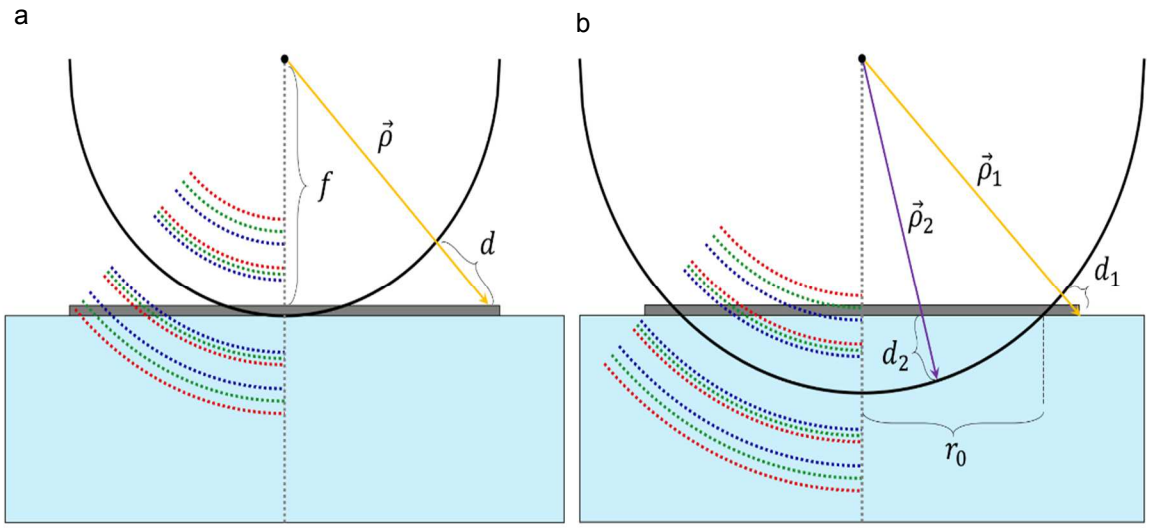

Figure 4.2S1: Geometrical interpretation of $C(\omega)$, the spectral degree of freedom. (a) Schematic of the conventional geometrical derivation of the phase function of a metalens. A reference wavefront (black) defines a segment d of ray $\vec{\rho}$ representing the distance an incident planewave must jump to meet the converging wavefront. Chromatic wavefronts diverge with opposite signs on either side of this reference wavefront, and can be seen intersecting the metalens in the order Blue, Green, Red for increasing distance from the central axis. (b) Schematic of the proposed geometrical derivation of the phase function of a metalens. The reference wavefront is extended past the surface of the metalens; chromatic wavefronts can be seen intersecting the metalens in the order Red, Green, Blue for increasing distance from the central axis up to the radius r_0.

each color overlap at the reference wavefront, but diverge due to dispersion on either side. The sign of this dispersion is opposite above and below the reference wavefront.

If we instead choose to propagate the reference wavefront by a distance $\sqrt{r_0^2 + f^2}$, it will intersect the plane of the metalens at a position r_0. This choice is depicted in Fig. 4.2S1b, wherein two zones of the metalens are thereby defined: for $r > r_0$, the sign of the dispersion at the metalens is the same as the conventional choice, but for $r < r_0$, it is opposite. In this region, the hemispherical incident wavefront must jump backwards to meet the metalens, corresponding to a phase delay that is proportional to a distance d. The phase function in this case is again easily written down as;

$$\phi(r,\omega) = -k_0 d = -\frac{\omega}{c}\left(\sqrt{r^2 + f^2} - \sqrt{r_0^2 + f^2}\right).$$

It is apparent from comparison of Fig. 4.2S1a with Fig. 4.2S1b that the sign of the dispersion of the chromatic wavefronts (i.e., intersection of red, green, and blue wavefronts with the metasurface) is opposite near the center of the lens. The location of the reference wavefront (determined by $C(\omega)$) therefore determines the sign of the dispersion required by the metalens.

Finally, we clarify the separate role C_0 plays. Generalizing the phase function above to include C_0, we can write:

$$\phi(r,\omega) = -\frac{\omega}{c}\left(\sqrt{r^2+f^2} - \sqrt{r_0^2+f^2}\right) + C_0.$$

It is readily apparent that $\phi(r = r_0, \omega) = C_0$ is independent of frequency. Therefore, C_0 is the value of the phase of the reference wavefront, and r_0 is the position of that wavefront. In a monochromatic metalens, r_0 and C_0 play a duplicate role, and only in achromatic metalenses does the distinction become relevant. In this way, the reference position r_0 can be interpreted as extending the concept of reference phase to include reference dispersion for the case of broadband metalenses.

4.2S2. Derivation of proposed $C(\omega)$ from Generalized Snell's Law

Deriving the form of the phase function of a metalens from the Generalized Snell's Law, or conservation of momentum, is a brief yet clarifying exercise. We present it here to motivate the proposed form of $C(\omega)$ from first principles. We begin with the observation that a converging metalens needs to deflect an incoming planewave by an angle θ at position r corresponding to:

$$\sin(\theta) = \frac{r}{\sqrt{r^2+f^2}}.$$

By the Generalized Snell's Law, this corresponds to a phase gradient:

$$\frac{d\phi(r,\omega)}{dr} = k_0 \sin(\theta) = \frac{\omega}{c}\frac{r}{\sqrt{r^2+f^2}},$$

where $k_0 = \frac{\omega}{c}$ is the free-space wavevector (we take the metalens to be focusing in air). Indefinite integration of the above leads to the phase function,

$$\phi(r,\omega) = \int dr \frac{\omega}{c} \frac{r}{\sqrt{r^2+f^2}} = -\frac{\omega}{c}\sqrt{r^2+f^2} + C(\omega),$$

and the Fundamental Theorem of Calculus obtains it in definite form,

$$\phi(r,\omega) = \int_{r_0}^{r} dr' \frac{\omega}{c} \frac{r'}{\sqrt{r'^2+f^2}} = -\frac{\omega}{c}\left\{\sqrt{r^2+f^2} - \sqrt{r_0^2+f^2}\right\},$$

where r_0 is a reference radius where the integration begins. A comparison to the indefinite form shows the choice:

$$C(\omega) = \frac{\omega}{c}\sqrt{r_0^2+f^2},$$

which is identical to equation (4.2) in the main text with the particular choice $C_0 = 0$.

The spectral degree of freedom $C(\omega)$ is therefore understood to be the same degree of freedom inherent to integration. The indefinite form puts no limitations on the form of $C(\omega)$, allowing it to be any function of frequency, including nonlinear functions of ω. Since both a typical meta-unit response as well as propagation phase have a linear dependence on frequency, a linear form of $C(\omega)$ is the natural choice. With the addition of the C_0 to reflect the arbitrary choice of the value of the reference phase, the definite form of the integral provides the most general linear form of $C(\omega)$ while abiding the natural physical interpretation explored in Supplementary section 4.2S1.

4.2S3. Derivation of lens limitations

An understanding of the relationship between desired lens parameters (the numerical aperture, *NA*, and the lens diameter, $D = 2R$, metasurface lattice spacing *P*) and the resulting required area of phase-dispersion space is important.

The first consideration is in the phase sampling rate of the metasurface, which is constrained by the largest deflection angle for the smallest wavelength. This constraint can be

made rigorous by considering the magnitude of the rate of phase change as a function of radial position:

$$\left|\frac{d\phi}{dr}\right| = \frac{\omega}{c}\frac{r}{\sqrt{f^2 + r^2}}. \qquad (4.2S1)$$

Using the definition of *NA*:

$$NA = n\,sin(\theta) = n\frac{R}{\sqrt{f^2 + R^2}}, \qquad (4.2S2)$$

then for a lens operating in air ($n = 1$), Eq. S1 at $r = R$ for the smallest wavelength simplifies to

$$\left|\frac{d\phi}{dr}\right|_{r=R} = \frac{\omega_{max}}{c}NA = k_{max}NA. \qquad (4.2S3)$$

Requiring at least N phase samples in a 2π phase range in a metasurface with periodicity P amounts to the constraint:

$$\left|\frac{d\phi}{dr}\right|_{r=R} < \frac{2\pi}{NP}. \qquad (4.2S4)$$

The choice of N will impact the efficiency of the metalens, with higher values of N producing higher efficiencies of diffraction into the 0th order. Combining equations (4.2S3) and (4.2S4) gives the constraint of:

$$NA < \frac{\lambda_{min}}{NP}. \qquad (4.2S5)$$

Equation (4.2S5) describes the tradeoff between the NA of a lens and its bandwidth of achromatic performance. The lower bound wavelength is directly represented as λ_{min}, while the upper bound is implicitly represented in P. If P is too small compared to a desired λ_{max}, the flexibility of structural dispersion engineering within a meta-unit area of $P \times P$ is restrained (i.e., phase-dispersion space is more difficult to fill). Thus equation (4.2S5) clarifies the impact of meta-unit library design on achievable lens performance.

The second consideration is that the limitations introduced by the finite coverage of the meta-unit library in phase-dispersion space. For simplicity, we focus on a meta-unit library that spans a finite range along the dispersion axis ($\Delta\Phi' = \left(\left.\frac{d\phi}{d\omega}\right|_{\max} - \left.\frac{d\phi}{d\omega}\right|_{\min}\right)\Delta\omega$) while fully spanning

the phase axis throughout this range. Since the extremes of dispersion are represented at the center and edge of the metalens, the required range of dispersion can be written:

$$\frac{d\phi(0,\omega)}{d\omega} - \frac{d\phi(R,\omega)}{d\omega} = \frac{d}{d\omega}\left(\frac{\omega}{c}\sqrt{f^2+R^2} - \frac{\omega}{c}\sqrt{f^2}\right). \qquad (4.2S6)$$

The limitations of a finite $\Delta\Phi'$ can therefore be written:

$$\Delta\Phi' \geq \frac{\Delta\omega}{c}\left(\sqrt{f^2+R^2} - \sqrt{f^2}\right). \qquad (4.2S7)$$

Using equation (4.2S2) again with $n = 1$, we arrive at a relationship between the maximum achievable radius of the metalens R_{max}, NA, operational bandwidth $\Delta\omega$, and the characteristic span $\Delta\Phi'$ along the dispersion axis:

$$R_{max} \leq \frac{\Delta\Phi'\,\mathrm{c}}{\Delta\omega\left(\frac{1}{NA} - \sqrt{\frac{1}{NA^2}-1}\right)}, \qquad (4.2S8)$$

which simplifies to $R_{max} \leq \frac{2\Delta\Phi'\,\mathrm{c}}{\Delta\omega NA}$, when *NA*<<1.

4.2S4. Structural dispersion in dielectric meta-units

In order to fill as much of phase-dispersion space as possible, the dielectric meta-unit library must contain a diverse set of phase and dispersion responses. Within the model of dielectric meta-units as vertical waveguides this suggests structuring the cross-section of the meta-units in order to get as diverse a set of effective index dispersion as possible. Figure 4.2S2 depicts structural dispersion in five example meta-units, chosen to represent various regions of phase-dispersion space. In the waveguide model, the phase is approximately:

$$\phi_0 = \frac{\omega_{min}}{c} n_{eff}(\omega_{min}) H,$$

while the dispersion is approximately

$$\Delta\phi = \frac{H}{c}\left(n_{eff}(\omega_{max})\omega_{max} - n_{eff}(\omega_{min})\omega_{min}\right),$$

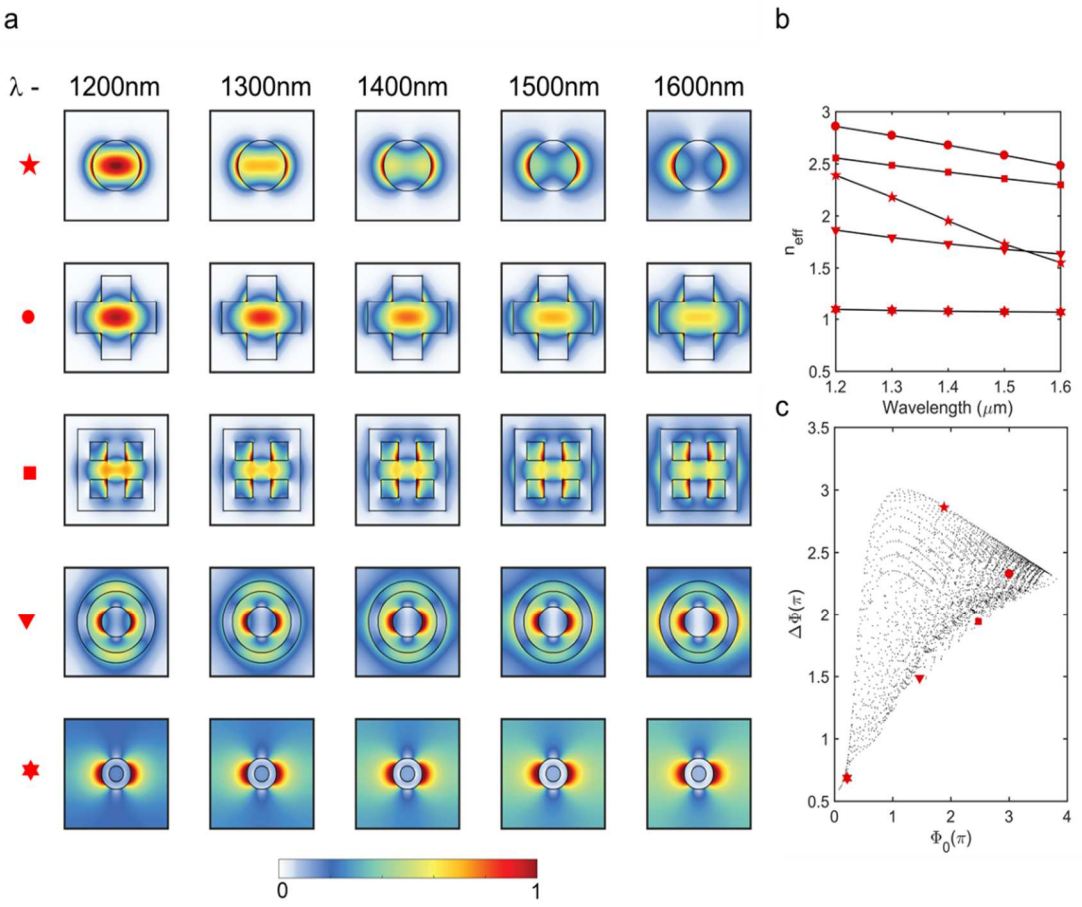

Figure 4.2S2: Mode profiles of example meta-units. (a) Each row corresponds to a single meta-unit, and each column a single wavelength. The first row depicts the most dispersive meta-unit, showing that for the lowest wavelength of 1,200 nm, the modal overlap with silicon is very high; conversely, for the longest wavelength of 1,600 nm, the modal overlap with silicon is quite low. This makes the effective index highly dispersive. In contrast, from top to bottom, each row depicts a meta-unit with successively smaller dispersion. For instance, in the final row the mode profiles of the shortest and longest wavelength are similar, implying little structural dispersion. (b) Corresponding effective indices of the meta-units. (c) Location of the meta-units in phase-dispersion space overlaid on top of a representative meta-unit library.

from which the role of the dispersion of $n_{eff}(\omega)$ is clarified. If $n_{eff}(\omega)$ is high for all frequencies, both the phase and dispersion will be large; if it is low for all frequencies, both the phase and dispersion will be low; if it is high for the highest frequency, but low for the lowest frequency, the phase will be low but the dispersion will be high. Several such example index profiles are seen in Fig. 4.2S2b, with the field profiles visualized in Fig. 4.2S2a and the corresponding points in phase-dispersion space marked in Fig 4.2S2c.

While calculating the phase response of our meta-units, we ignored the possibility of power coupling into higher-order waveguide modes. We can estimate the correct effective index of each meta-unit by taking the average of effective modal indices of each propagating mode weighted by the fraction of power carried by the mode. We have numerically solved for effective modal indices of the higher-order modes and the fraction of power coupled into them from free space by using eigenmode analysis techniques (Fig. 4.2S3). This has been done for various meta-unit architypes and the error in the estimation of effective indices when ignoring the higher-order modes has been calculated (Fig. 4.2S4). From these calculations, we observe that the choice of ignoring higher-order modes does not affect the calculation of the phase response of meta-units that have small to medium cross-section, since high-order modes do not propagate in such waveguides (e.g., meta unit disc1 and disc2, which are cylinders with radii 100 and 200 nm, respectively; see Fig. 4.2S4a). For meta-units with large cross-section in our library, up to two higher-order modes can propagate depending upon the meta-unit archetype and the wavelength (e.g., meta-unit disc3, which is a cylinder with radius 300 nm, supports two higher-order propagating modes; see Fig. 4.2S4a). We see that in the worst-case scenario of meta-units with very large cross-section, our estimation of effective indices can be off by up to 20% primarily at short wavelengths (Fig. 4.2S4c). However, these types of meta-units make up a small portion of our meta-unit library, hence our estimation of the effective indices of the meta-units based only on the fundamental waveguide modes is largely correct.

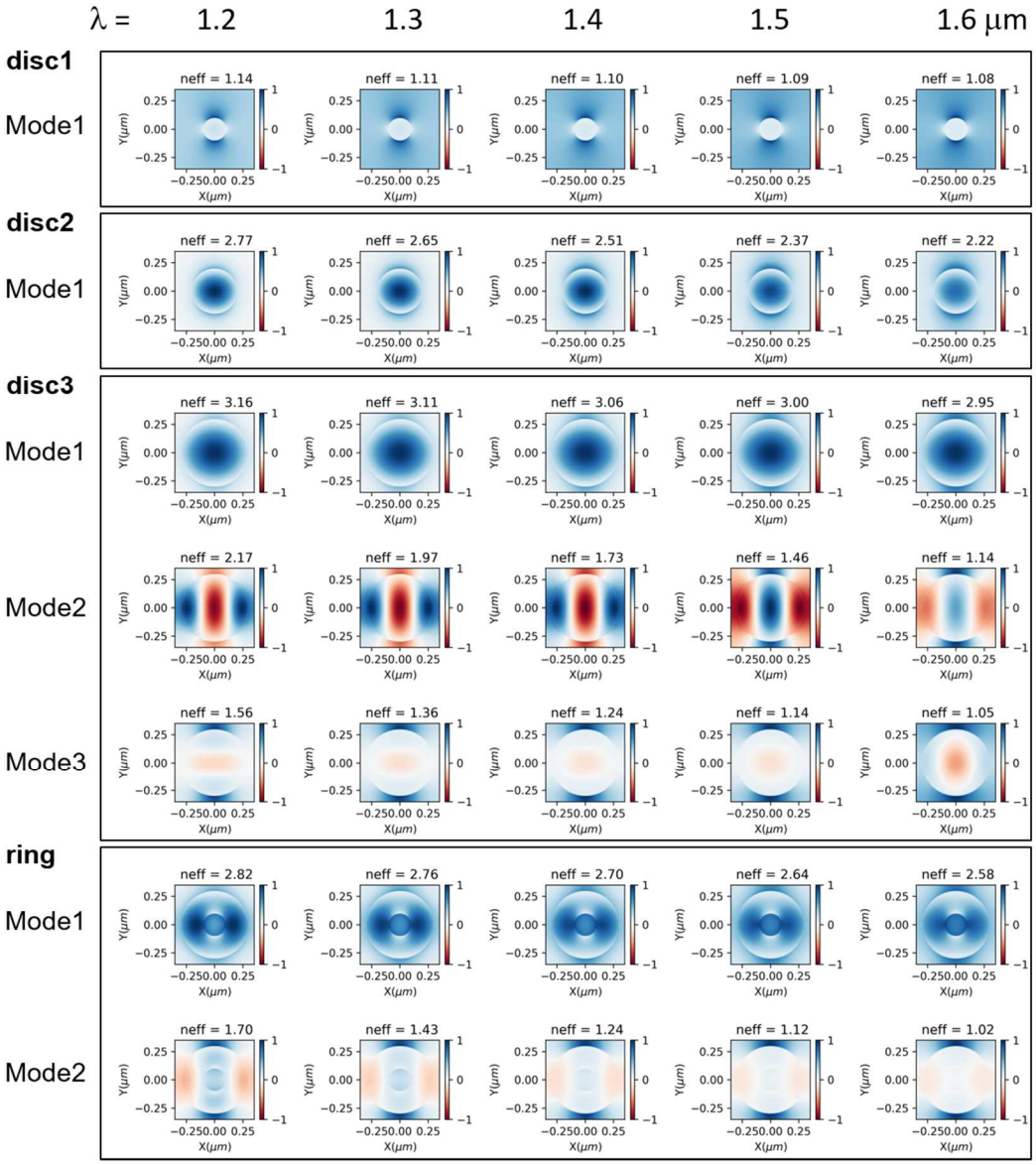
λ = 1.2 1.3 1.4 1.5 1.6 μm
disc1
Mode1
neff = 1.14
neff = 1.11
neff = 1.10
neff = 1.09
neff = 1.08
disc2
Mode1
neff = 2.77
neff = 2.65
neff = 2.51
neff = 2.37
neff = 2.22
disc3
Mode1
neff = 3.16
neff = 3.11
neff = 3.06
neff = 3.00
neff = 2.95
Mode2
neff = 2.17
neff = 1.97
neff = 1.73
neff = 1.46
neff = 1.14
Mode3
neff = 1.56
neff = 1.36
neff = 1.24
neff = 1.14
neff = 1.05
ring
Mode1
neff = 2.82
neff = 2.76
neff = 2.70
neff = 2.64
neff = 2.58
Mode2
neff = 1.70
neff = 1.43
neff = 1.24
neff = 1.12
neff = 1.02
Y(μm)
X(μm)
0.25
0.00
−0.25
−0.250.00 0.25
1
0
−1

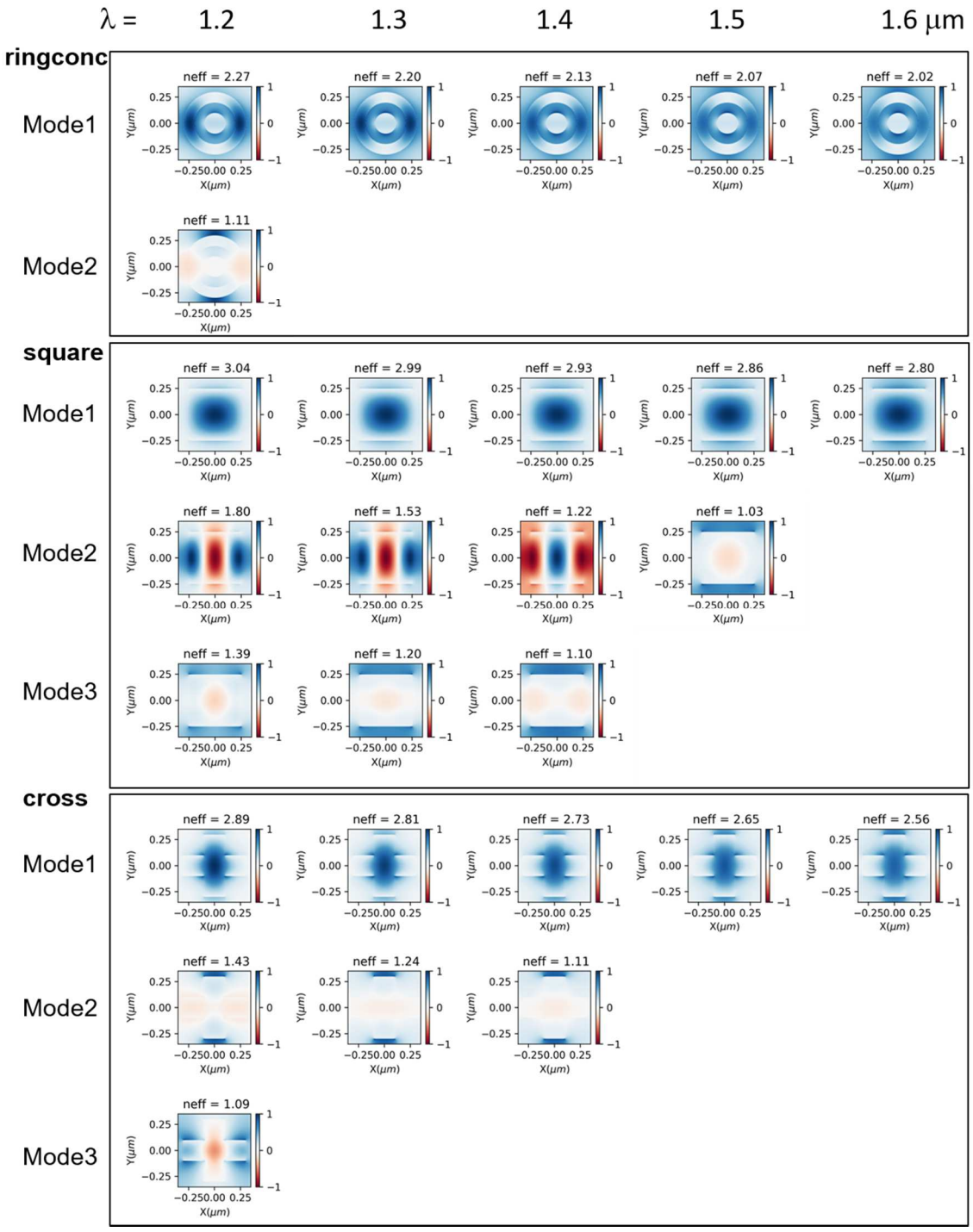

Figure 4.2S3: Modal analysis of meta-units. Eigenmode analysis for different archetypes are calculated as a function of wavelength and higher order modes are included.

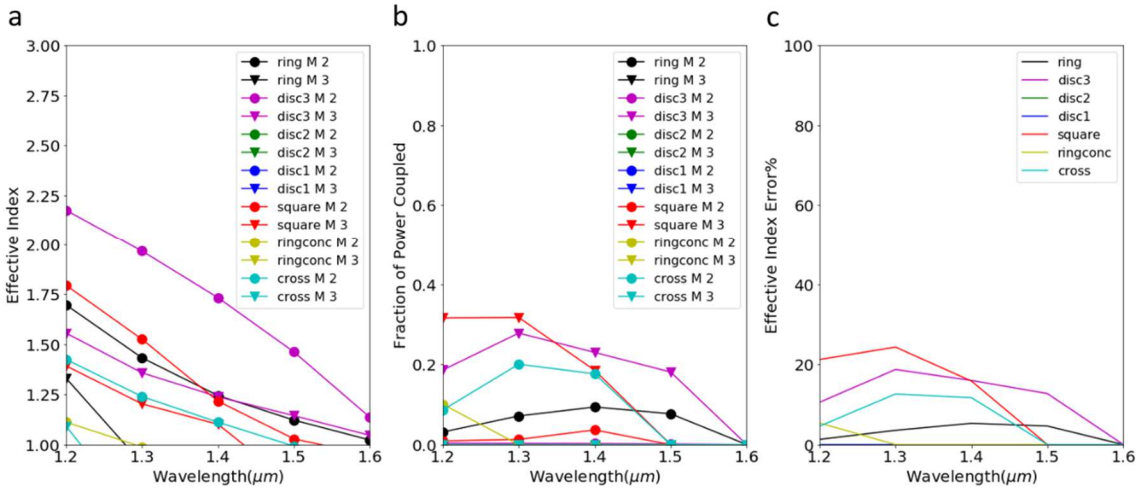

Figure 4.2S4 Coupling into higher-order modes. (a) Effective indices of the 2nd and 3rd order waveguide modes of selected meta-units of each archetype as a function of wavelength. Note for meta-units disc1 and disc2, which have a cylindrical cross-section of radii 100 and 200 nm, respectively, only the fundamental mode propagates. Whereas for disc3, which has a cylindrical cross-section of radius 300 nm, there are two higher-order modes (i.e., "M 2" and "M 3") that can propagate. (b) Fraction of power coupled into the higher-order modes. (c) Percentage error in estimation of effective modal indices when ignoring coupling into higher-order waveguide modes.

4.2S5. Treatment of sharp resonances of meta-units

A notable point of divergence in the present approach compared to recent work is in the treatment of sharp Fano resonances present in infinitely periodic lattices of dielectric meta-units. These are easily calculated from simulating the meta-units in full-wave simulations (for instance, Finite-Difference Time-Domain) with periodic boundary conditions. Past efforts using reflection-based dielectric meta-unit libraries rely on these sharp resonances to provide large dispersion meta-units (the phase goes through $\sim 2\pi$ across these resonances, so the dispersion is inversely proportional to the resonance bandwidth: $\frac{d\phi}{d\omega} \cong \frac{2\pi}{\Delta\omega}$).

However, we believe that there are a number of disadvantages to relying on these sharp resonances. First, this approach requires careful alignment of many such resonances. Second, narrow bandwidth resonances are by their nature difficult to reliably achieve in experiment as their

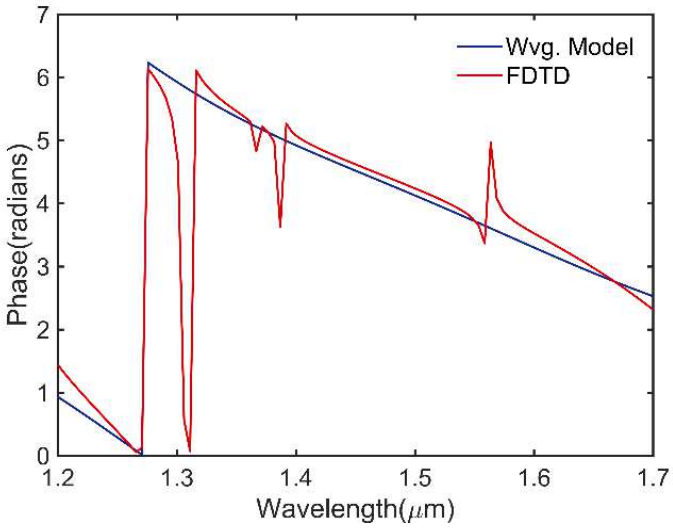

Figure 4.2S5: Comparison of phase responses of an example meta-unit obtained by the waveguide model and Finite-Difference Time-Domain (FDTD). Our waveguide approximation is seen to reproduce the trend predicted by the FDTD simulation, excluding sharp resonances.

long optical lifetimes intrinsically make them sensitive to small changes in structure (period, meta-unit cross-section) and surroundings. Third, they are difficult to generalize to high efficiency transmission mode metalenses, because the sharp resonances are typically associated with a transmission dip (irrelevant for reflection mode metalenses). Fourth, the resonances are born of the periodic interactions of many dielectric meta-units; a meta-unit located among dissimilar neighboring meta-units may not have the same response. This invalidates the assumption intrinsic to metasurfaces that meta-units operate approximately independently from each other. Moreover, while the periodic behavior is retained as more and more periods are included (e.g., low *NA* metalenses include regions of meta-units that are largely periodic), the degree of retention is a complex function of intrinsic optical lifetime, index contrast, and mode profile; it is difficult to reliably predict how many periods are needed. Indeed, even the bandwidth of the resonance will change as the number of periods changes, reducing the predictive power of the meta-unit library.

We note that while the proper treatment of sharp resonances is a subtle and open question, and submit that for broadband, high *NA* metalenses operating in *transmission* mode, the preferred approach should not rely on them. First, for rapidly changing phase profiles (especially at the edge

of a metalens) the meta-units will also need to change rapidly, meaning that very few periods will be present. In these cases, the sharp spectral lines may not be realized at all. Second, even in the case that sufficient periods are present (e.g., in a region of a metalens with very slowly changing phase profile), the spectral weight of the resonances over a broad bandwidth is often very small as seen in Fig. 4.2S5. This means that while the phase/amplitude responses for a few wavelengths in this region of the metalens may be different from the prediction of the waveguide model due to the resonances, the majority of the functionality of our metalenses will be retained. Third, in our experience, many typical metalenses of interest (*NA* and radii not too small) do not have many repetitive neighboring meta-units. For such metalenses the actual behavior of a meta-unit within a metalens should be typically much closer to the waveguide approximation, which can be seen to exclude the sharp resonances in Fig. 4.2S5. The waveguide model agrees well with full-wave simulations of infinitely periodic structures away from resonances. Neither approach to constructing a meta-unit library fully captures how a meta-unit would response in a metalens, but for the above reasons we believe that the waveguide approach is a better choice.

Some resonances, however, can be quite broadband, and can result in large back-reflection due to nearest neighbor coupling of only a few similar meta-units. This particularly impacts smaller wavelengths (where more complex modal interactions are possible) while it is less relevant for longer wavelengths (where the meta-unit lattice is deeply subwavelength). The waveguide approximation does not adequately treat these meta-units because it ignores the complex modal interactions, and future work could benefit from using a combination of full-wave simulations and the waveguide approach to exclude meta-units that exhibit spectra with broadband reflection. Future work could also benefit from fully including the modal interactions of nearest neighbors in metasurface design, which is especially relevant for materials systems with refractive indices lower than that of silicon (e.g., SiN, GaN, TiO_2).

4.2S6. Phase sampling of example metalens

Figure 4.2S6(a,b) compare achieved phase profiles by Generation 1A and 1B libraries of a metalens with R = 100 μm and NA = 0.14. It is evident that the Generation 1B library has small phase errors across four select wavelengths at all radial positions, while the Generation 1A library has substantial phase errors at the edge of lens. This indicates that the target metalens has too large a diameter or NA for the Generation 1A library to satisfy.

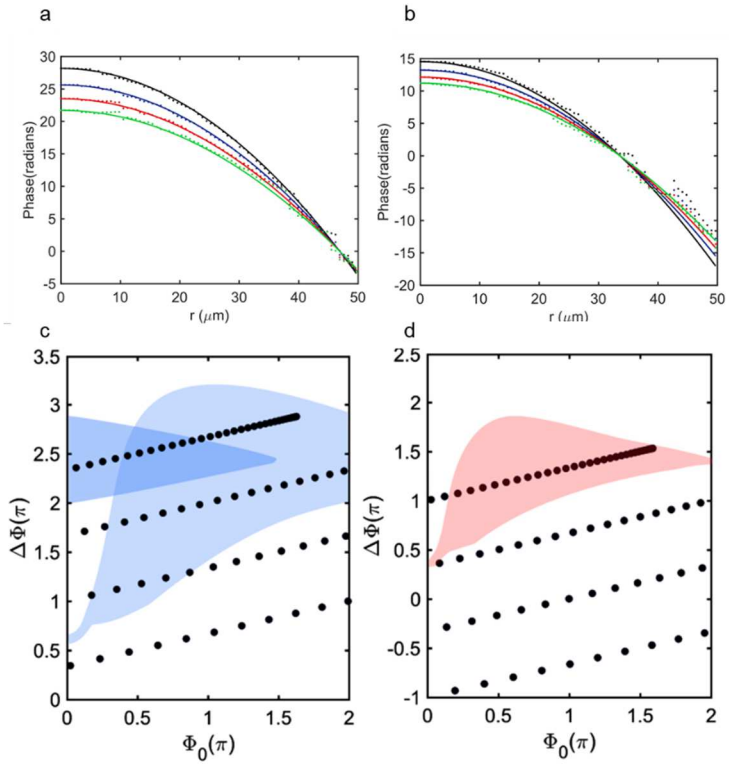

Figure 4.2S6 Comparison of achieved phase profiles by Generation 1A and 1B libraries of a metalens at four select wavelengths. Black, blue, red, and green represent wavelengths of 1210 nm, 1330 nm, 1450 nm, and 1570, respectively. The metalens has R = 100 μm and NA = 0.14. Note minimization of phase errors due to improved phase coverage offered by Generation 1B library in (a) compared to Generation 1A library in (b).

4.2S7. Comparison of simulated and experimental focal spots

In order to anchor expectations for experimental results, dipole simulations are performed using the expected responses of the meta-units retrieved from error minimization. Due to computational constraints, it is impractical to perform full-wave simulations of metalenses of the size we experimentally demonstrated. In lieu of full-wave simulations, dipole summations on a real-space grid are performed for each wavelength: a dipole is placed at each lattice point on the metalens, with wavelength dependent complex value $A(\lambda)\exp(i\phi(\lambda))$, where $A(\lambda)$ is the calculated amplitude response and $\phi(\lambda)$ is the calculated phase response of the chosen meta-unit for that point. The interference of these dipole sources (indexed by j) propagated towards the designed focal spot is calculated and recorded for each wavelength:

$$E(x,y,z,\lambda) = \sum_j A(\lambda)\exp\left(i\phi(\lambda)\right)\frac{\exp\left(i\frac{2\pi}{\lambda}R_j\right)}{R_j},$$

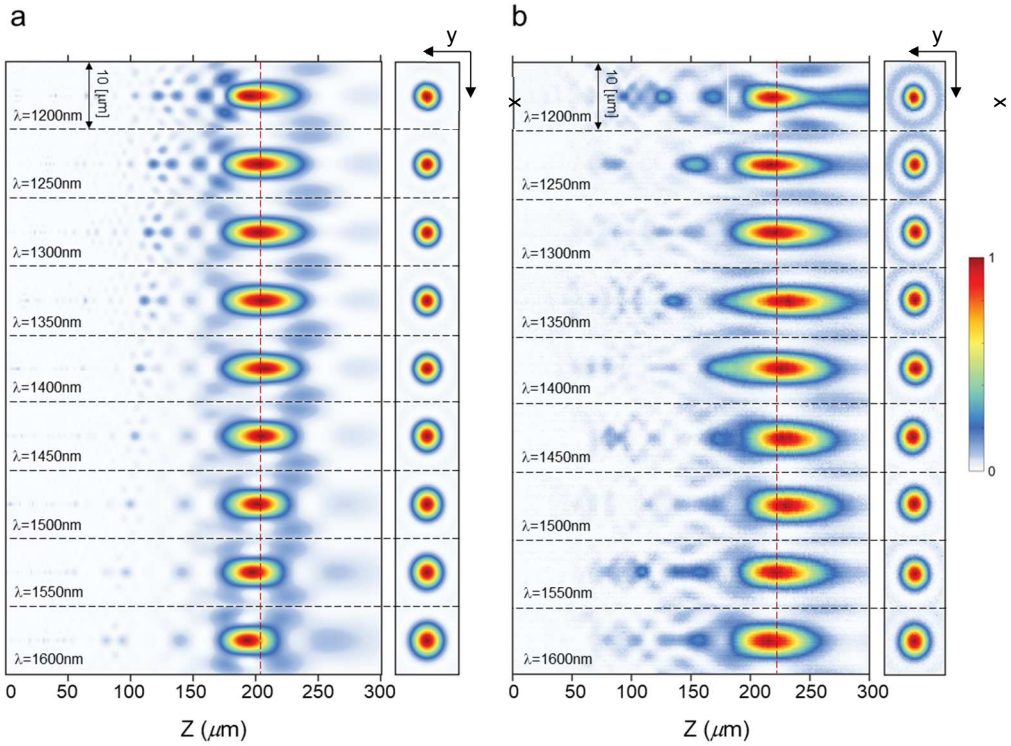

Figure 4.2S7: Comparison between numerical simulation and experimental results. (a) Dipole simulation results, showing some parasitic secondary spots, with reduced magnitude compared to experimental results in (b).

and compared to the experimental results as seen in Fig. 4.2S7.

Comparisons of this dipole approach and full-wave simulations (FDTD, Lumerical Solutions) are performed for much smaller lenses (where full-wave simulations are feasible) and the agreement is good. This suggests the validity of the dipole approach as a tool for approximate comparison to larger, experimental metalenses.

4.2S8. Simulation of compound metalens system

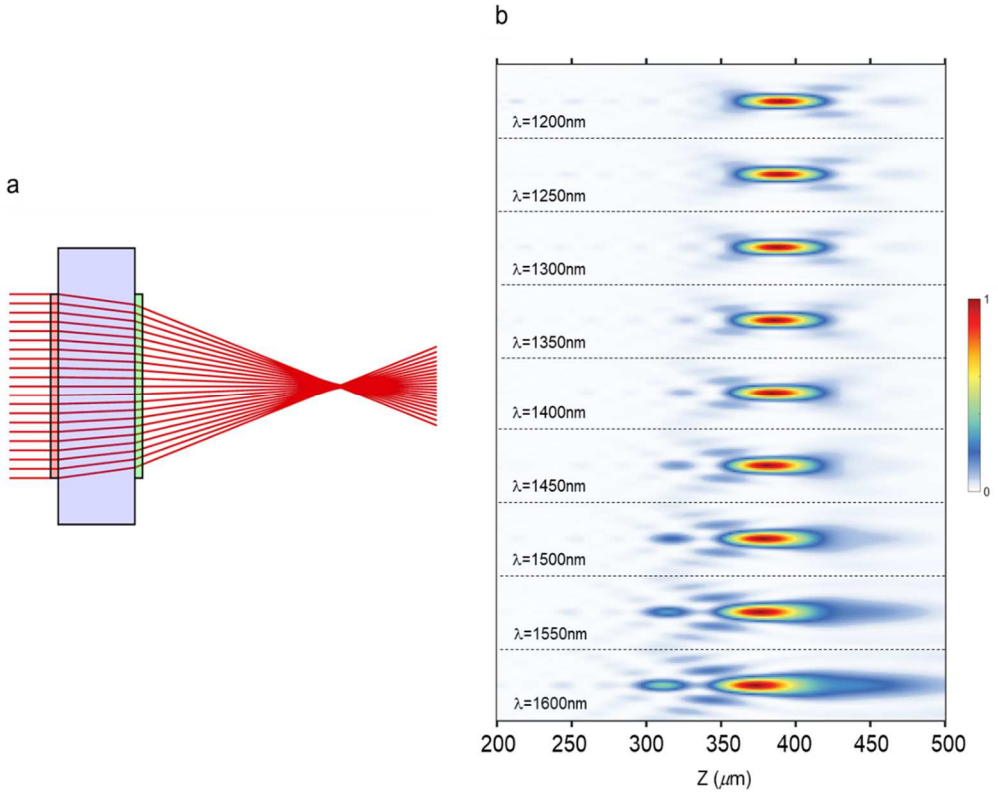

Figure 4.2S8 Stack of two achromatic metalenses. (a) Ray tracing diagram of a metalens doublet with two identical converging lenses. (b) Axial (x-z cross-section) intensity distributions of the doublet calculated using dipole simulations where the design focal length and diameter of each metalens are 800 μm and 200 μm, respectively, with spacing set to 50 μm. The focal length of the doublet is calculated to be 412 μm using the paraxial thin-lens approximation.

As an initial exploration of the utility of the present approach for compact imaging systems based on compound metalenses, we perform dipole simulations (4.2A8) for an example metalens doublet. The metalenses are spaced $\mathrm{s} = 50\ \mu\mathrm{m}$ apart, and have identical parameters ($D = 200\ \mu\mathrm{m}$, $f = 800\ \mu\mathrm{m}$), each of which is separately corrected for chromatic aberration.

According to geometrical optics, the focal length, F of the doublet can be determined by the following relation:

$$\frac{1}{\mathrm{F}} = \frac{1}{f} + \frac{1}{f} - \frac{s}{f^2}.$$

The ray picture of the doublet is shown in Fig. 4.2S8a, and the dipole calculation of the far field of the metalens doublet is shown in Fig. 4.2S8b. The expected focal length agrees well with the calculated focal length. The retention of the achromatic behavior for a higher *NA* than achievable with a singlet confirms the utility of the approach for high performance compound metalens systems.

4.2S9. Meta-unit library construction by binary search

In order to determine whether the meta-unit cross-sections used fully span the phase-dispersion space for a given height, we perform a more exhaustive set of simulations. As depicted in Fig. 4.2S9a, we discretize an area of a meta-unit period into a 14×14 grid, and explore all choices of populating each pixel of this grid by either air or Silicon. To reduce the coupling between adjacent meta-units and to be consistent with our fabricated structures, we keep a boundary of air at the edges of the meta-unit period, leaving a 12×12 grid to explore. We limit the cross-sections to those with four-fold symmetry to retain polarization independent behavior. This allows the cross-sections to be defined on an octant of the grid, and leaves 21 unique pixels to define the cross-sections. The total number of simulations is therefore 2^{21} = 2,097,512.

Figure 4.2S9b shows the resulting meta-unit library for a height of $H = 1{,}400\ \mathrm{nm}$ in phase-dispersion space. Also shown are results for singular pillars as a reference, as well as an effective

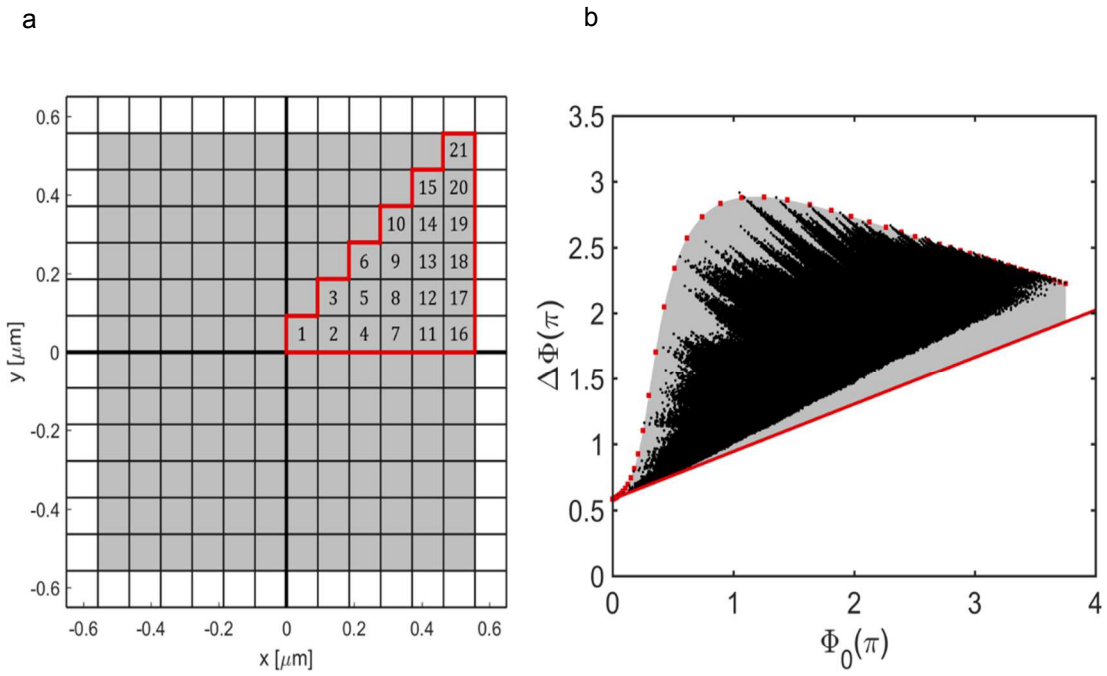

Fig. 4.2S9 Meta-unit library constructed from binary search. (a) Diagram showing the geometrical definition of 21 pixels that can either be air or Silicon. A boundary of air is left surrounding the modified area. The remaining choices are determined by symmetry based on the octant outlined in red. (b) A set of 221 = 2,097,152 simulations exploring all combinations of geometries. Also plotted are singular pillars (red squares) and an ideal effective medium (red line), showing that the binary search begins to fill in the shaded area bounded by these two references.

medium line representing the theoretical limit of performance at minimal dispersion (no structural dispersion). The area between these two references is shaded grey. It is evident that the results of this binary search begin to fill the shaded area, but do not extend past it. This suggests that the meta-unit libraries chosen based on physical intuition perform as well as the brute-force approach taken here. A finer grid would fill the shaded area better at high dispersion values, but would make the number of simulations impractical to perform.

We lastly note that the impact of the boundary of air is two-fold. First, a sharp cut-off in the shaded grey area is apparent at high phase. This represents the fact that a fully-Silicon meta-unit is never used (so the upper limit of the effective index is less than that of silicon). Secondly, as the value of phase increases, the lowest dispersion values possible begins to diverge from the effective medium line. This can be interpreted as the wavelength dependence of the boundary (the index for longer wavelengths is reduced more by the air boundary than the index for shorter wavelengths). This binary approach therefore suggests that the inclusion of an air boundary imposes a practical

limit to the lowest values of dispersion possible. A comparison to Generation 2 shows that Generation 2 is near this practical limit, but with much more easily fabricable cross-sections.

Table 4.2S1. Parameters of fabricated metalenses.

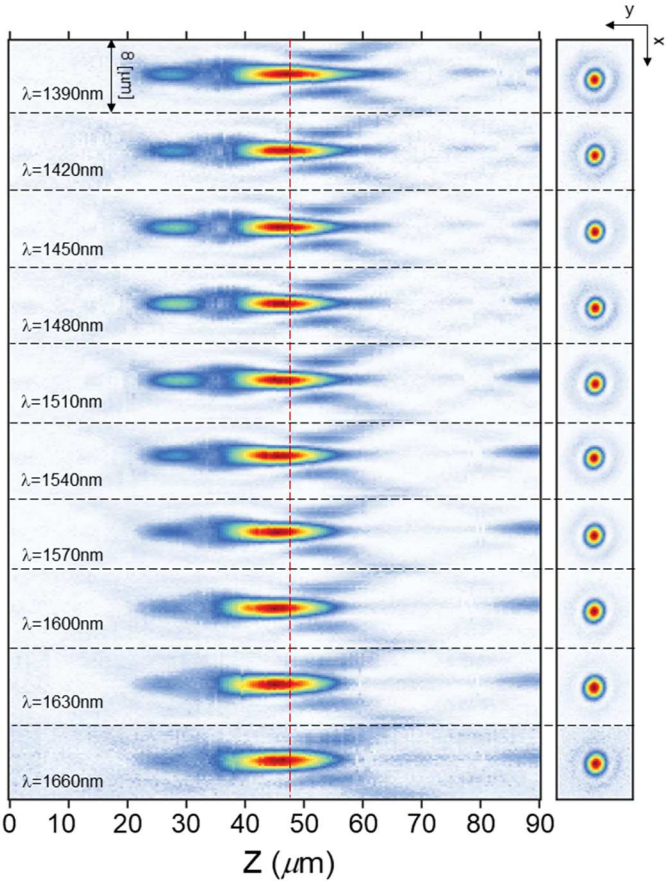

Figure 4.2S10 Diverging Lens. Measured axial (x-z cross-section) and focal plane (x-y cross-section) intensity distributions of a diverging lens with design focal length 50 μm and diameter 100 μm (*NA* ~ 0.7). The measured focal spot is a virtual spot behind the metasurface, where the wavefront originates. Hence, the motorized stage with the objective and the camera is moved towards the metasurface to scan the virtual 3D far-field intensity distribution. The operational bandwidth (~ 270 nm) of the lens is reduced to achieve large *NA*.

4.2S10. Performance of diverging metalenses

Metalens	Diameter, D (μm)	Focal length, f (μm)	Numerical Aperture, NA	Library Generation	Operating Bandwidth (nm)
M1A	100	200	0.24	1A	1,300 – 1,650
M1B	100	200	0.24	1B	1,200 – 1,650
M2	200	800	0.13	1B	1,200 – 1,650
M3	100	30	0.88	2	1,200 – 1,400

Chapter 5: Multi-element Metasurface Systems for Imaging

The material in this chapter is part of a manuscript that is currently under review.

In this chapter, I will present a brief introduction of monochromatic optical aberration. Then I will outline optimization methods to correct for such aberration using raytracing techniques. Finally, I will present a multi-element metasurface system to correct for both monochromatic and chromatic aberration simultaneously for imaging.

5.1 Monochromatic Optical Aberrations

Monochromatic optical aberrations are deviation of optical wavefront from the ideal spherical surface as it emerges from the exit pupil of an element. In other words, a point on the object plane is not mapped to exactly one unique point on the image plane by the optical element.

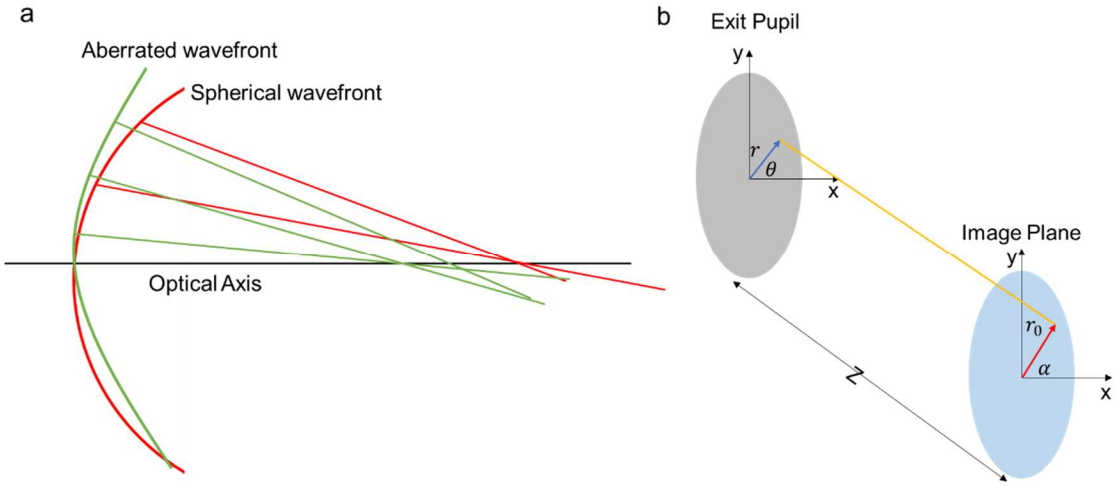

Figure 5.1: Monochromatic aberration. (a) Rays from an idea spherical wavefront cross the optical axis at one location. Rays from an aberrated wavefront cross the optical wavefront at multiple location. (b) Propagation of a point object from the exit pupil of an optical element to the image plane at a distance Z away.

Figure 5.1a shows a comparison of rays converging to a point on the optical axis from an ideal

spherical wavefront and an aberrated one. The spherical wavefront all converge to a single point on the optical axis whereas the rays coming from aberrated wavefront cross the optical axis at many points. A primary reason for this is the paraxial approximation that is used when modelling optical elements. Such an assumption does not take into account diffractive effects. In addition, fabrication errors also add to the deviation from the ideal wavefront.

The amount of aberration in the optical wavefront can be quantified by quantifying the phase difference between the optical wavefront emerging from an optical element with the phase of the ideal spherical wavefront. We can do so by first calculating the phase accumulated when a point on the exit pupil is propagated to a point on the image plane. Figure 5.1b shows a point (r, θ) on the exit pupil plane that is propagated to the image plane a distance z away from the exit pupil to a point (r_0, α). Polar coordinates are chosen since we are assuming a circularly symmetric optical element. The distance between the two points is:

$$R = \sqrt{z^2 + (rcos\theta - r_0 cos\alpha)^2 + (rsin\theta - r_0 sin\alpha)^2} \qquad (5.1)$$

The phase accumulated is then calculated as:

$$\Phi(z) = \frac{2\pi}{\lambda} R = \frac{2\pi z}{\lambda}\left\{1 + \left[\frac{r^2 + r_0^2}{z^2} + \left(-\frac{2rr_0}{z^2} cos\phi\right)\right]\right\}^{\frac{1}{2}} \qquad (5.2)$$

where $\phi = \theta - \alpha$. After power series expansion and further simplification, we get [145],

$$\phi(z) \approx \frac{2\pi z}{\lambda} + \frac{\pi}{\lambda z} r^2 + \frac{\pi}{\lambda z} r_0^2 - \frac{2\pi}{\lambda z} r r_0 cos\phi - \frac{\pi}{4\lambda z^3} r^4 - \frac{\pi}{\lambda z^3} r_0^4 - \frac{\pi}{\lambda z^3} r^2 r_0^2 \cos^2\phi -$$

$$\frac{\pi}{\lambda z^3} r^2 r_0^2 + \frac{\pi}{\lambda z^3} r r_0^3 cos\phi + \frac{\pi}{\lambda z^3} r^3 r_0 cos\phi \qquad (5.3)$$

Eqn. 5.3 is a decomposition of the optical wavefront in to multiple terms with varying powers of the pupil and image plane coordinate and their angular orientation. Finally, we can calculate the phase difference between the actual and the ideal spherical wavefront as:

$$\Delta\Phi = \Phi_{actual} - \Phi_{spherical}$$

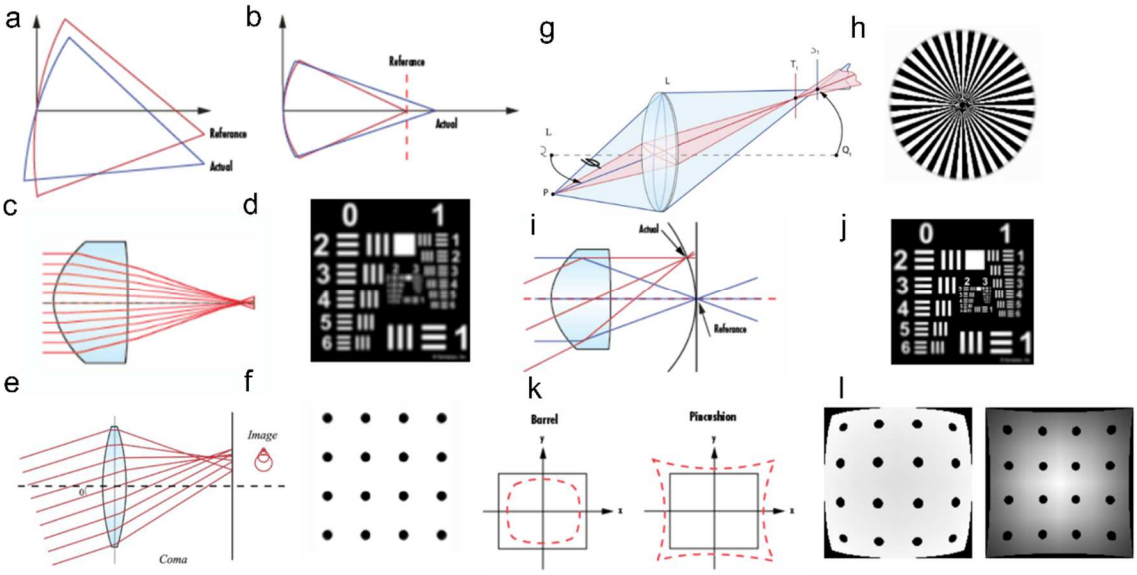

Figure 5.2: Image formed by aberrated systems. (a) Tip-Tilt aberration- the wavefront is tilted with respect to the reference producing incorrect magnification. (b) Defocus-the focal plane is shifted from the design. This can be corrected by shifting the sensor to new focal plane. (c) Spherical aberration- rays from the edge and the center are focused at different planes. (d) Images formed by spherical aberrated system are blurred. (e) Coma- magnification changes as a function of spatial location on the imaging plane. (f) Coma aberration causes dots at the edges to be larger than the central ones. (g) Astigmatism – produces two focal planes for horizontal and vertical planes. Focal spots are asymmetrical. (h) Aberrated image formed due to astigmatism. (i) Field Curvature- non-normal incident rays are focused on to different plane. The plane is a curved surface. Therefore, a curved imaging sensor could produce a perfect image. (j) Due to field curvature aberration, image is defocused at the edges. (k) Distortion – produces images with spatially varying magnification. There are barrel and pincushion type of distortion. (l) Aberrated images formed due to barrel and pincushion type distortion. (adapted from [146])

$$\Delta\Phi = \sum_{i+j+k} W_{ijk} r_0^i r^j \cos^k \phi \qquad (5.4)$$

where we have written the phase difference in terms of the terms derived in Eq. (5.3) weighted by coefficients W_{ijk} that determines the contribution of each term. Each term has a unique contribution to optical aberration and have been assigned names. The following are the well-known aberration terms:

W_{000} → Propagation from exit plane to image plane. Not an aberration.

$W_{200}\, r_0^2$ → Piston

$W_{111}\, r_0 r$ → Tip-Tilt

$W_{020}\, r^2$ → Defocus

$W_{040}\, r^4$ → Spherical aberration

$W_{131}\, r_0 r^3 cos\phi$ → Coma

$W_{220}\, r_0^2 r^2$ → Field curvature

$W_{222} r_0^2 r^2 \cos^2 \phi$ → Astigmatism

$W_{311} r_0^3 r\, cos\, \phi$ → Distortion

$W_{400} r_0^4$ → Piston

Figure 5.2 shows the effect of these terms on image formation [146]. The extent of the aberration is determined by the amplitude of the coefficient and complicated multielement optical systems may be needed to correct for these terms. A detailed discussion on individual terms is out of the scope of this work.

Other decomposition methods are also used to describe wavefront aberration. In particular, Zernike polynomials [147] are widely used by the optical design community to quantify

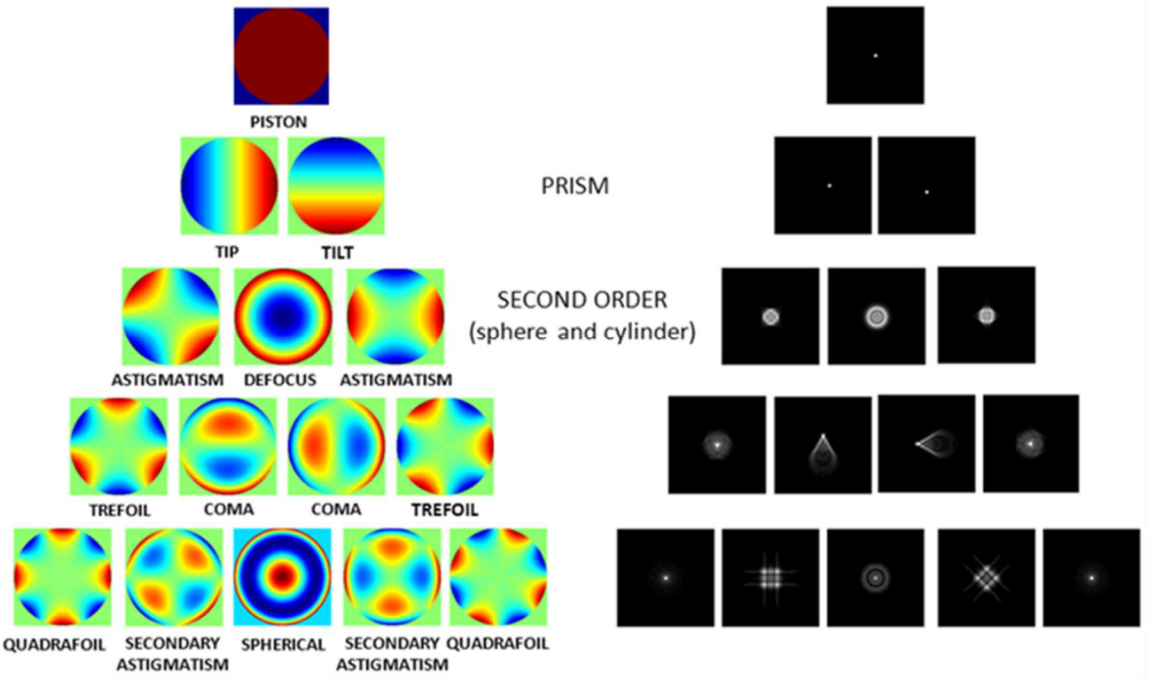

Figure 5.3: Zernike polynomial decomposition. First 15 Zernike polynomials and corresponding point spread function formed at the focal plane. (adapted from [147])

monochromatic aberration. They have an added advantage of being orthogonal to one another. Figure 5.3 shows the first 15 Zernike polynomials and the distorted point spread function at the focal plane due to each aberration term.

5.3 Metalens Triplet Design for Optical Aberration Correction

Advances in compact imaging, augmented/virtual reality and medical imaging devices have fueled the demand of high performance, light-weight and compact optical systems. Conventionally, these systems require multiple bulk optical elements stacked together to correct optical aberrations [105]. In high-performance systems, manufacturing of the elements requires meticulous grinding and polishing of different types of glasses, followed by precise alignment of individual elements. Planar optical metasurfaces [2,13,16,51,106,111,148] are promising candidates to replace conventional optical elements in these systems due to their flat formfactor, which may facilitate integration in miniature optical systems. Furthermore, optical metasurfaces can be fabricated using conventional lithographic techniques employed in CMOS foundries, suggesting the possibility of defining metasurface elements on superstrates directly on top of image sensors.

Metasurfaces can realize many optical functionalities [12,15,21,44,103,149] by encoding suitable phase, amplitude and/or polarization responses to individual elements called meta-atoms. Using meta-atoms of high-index dielectric materials, highly efficient [23,25,29,32,150] metasurfaces have been recently demonstrated for various applications [151–156]. Singlet metalenses implementing an analytical phase function are well-known to produce diffraction-limited focal spots free of spherical aberration for normally incident light. However, away from the design wavelength, significant chromatic aberrations will be present, and for light of oblique incident angles, significant monochromatic aberrations will degrade imaging performance.

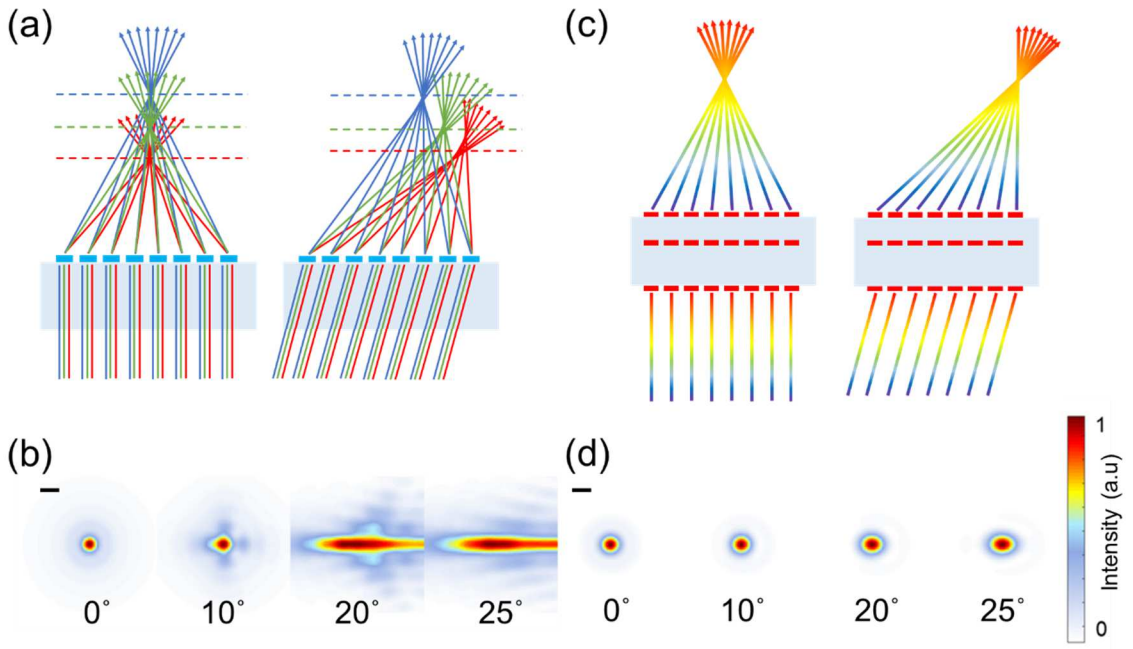

Figure 5.4: Correcting optical aberrations. (a,c) Illustrations of ray focusing by metalens singlet (a) and triplet (c) systems for light of various wavelengths incident at normal and off-normal angles. (b,d) Focal spots produced by the singlet (b) and triplet (d) when focusing a broadband source in the wavelength range of 1.30 to 1.60 μm. Scale bar: 10 μm

While chromatic aberrations are corrected in refractive optical system by using multiple glasses [157] providing different dispersions or by adding diffractive components [158,159], achromatic focusing across a continuous wavelength range in metalenses can be achieved by controlling the dispersive response [135] of individual meta-atoms.

Achromatic metalens singlets working in the visible [137,138] and the near-infrared [160] have been reported in recent works. Our previous work [160] has demonstrated polarization insensitive achromatic focusing in the near-infrared across a wavelength range of 1200 – 1600 nm by using structural dispersion engineered meta-atoms.

Enlarging the field of view (FOV) via correction of monochromatic aberrations such as coma and astigmatism is equally important for imaging systems, but cannot be achieved by a single metalens due to the fact that individual meta-atoms, being optically small, primarily produce spherical scattered wavefronts (Huygens' wavelets), which are invariant as a function of angle. However, an approach based on metasurface stacks [133,161,162] can be optimized to correct

monochromatic aberrations. In particular, metalens doublet systems operating in the near-infrared [128] and visible [129] have been reported recently with FOV of up to 60°. However, these demonstrations lack chromatic aberration corrections and so are not ideal for broadband imaging. Many other multi-element designs have been reported to extend the control of optical wavefront across multiple wavelengths [101,104,130,131,163] or incident angles [102], but none have been reported to correct both chromatic and monochromatic aberrations. In this report, we demonstrate a polarization insensitive metalens triplet designed to correct both chromatic and monochromatic aberrations across a continuous wavelength range in the near-infrared and with a FOV of 50°.

Figure 5.4(a, b) compares the focusing of a bundle of rays of light by a metalens singlet with only chromatic aberration correction and a triplet correcting both chromatic and monochromatic aberrations. There are significant aberrations for the singlet at oblique incident angles. These aberrations are suppressed for a properly designed triplet system. Figures 5.4(c, d) further demonstrate the comparison between a singlet and an aberration corrected triplet metalens with the same numerical aperture (NA), where we show simulated polychromatic focal plane intensity distributions at various angles of incidence. We can clearly observe the aberrations in the focal spots produced by the singlet compared to those formed by the triplet. The design process of multi-element meta-lens system is made tractable by the fact that ray tracing approaches are valid for metasurfaces just as they are for diffractive optical elements. We therefore design our aberration-corrected metalens triplet using conventional ray-tracing techniques by minimizing the root mean square (RMS) focal spot size for a range of incident angles simultaneously through an appropriate choice of phase profiles for all three constituent metasurfaces. In the optimization process, the phase profile for each metasurface is parametrized as even-ordered polynomials,

$$\Phi^{(m)}(\delta) = \sum_{n=1}^{5} a_n^{(m)} \left(\frac{\delta}{R^{(m)}}\right)^{2n} \qquad (5.5)$$

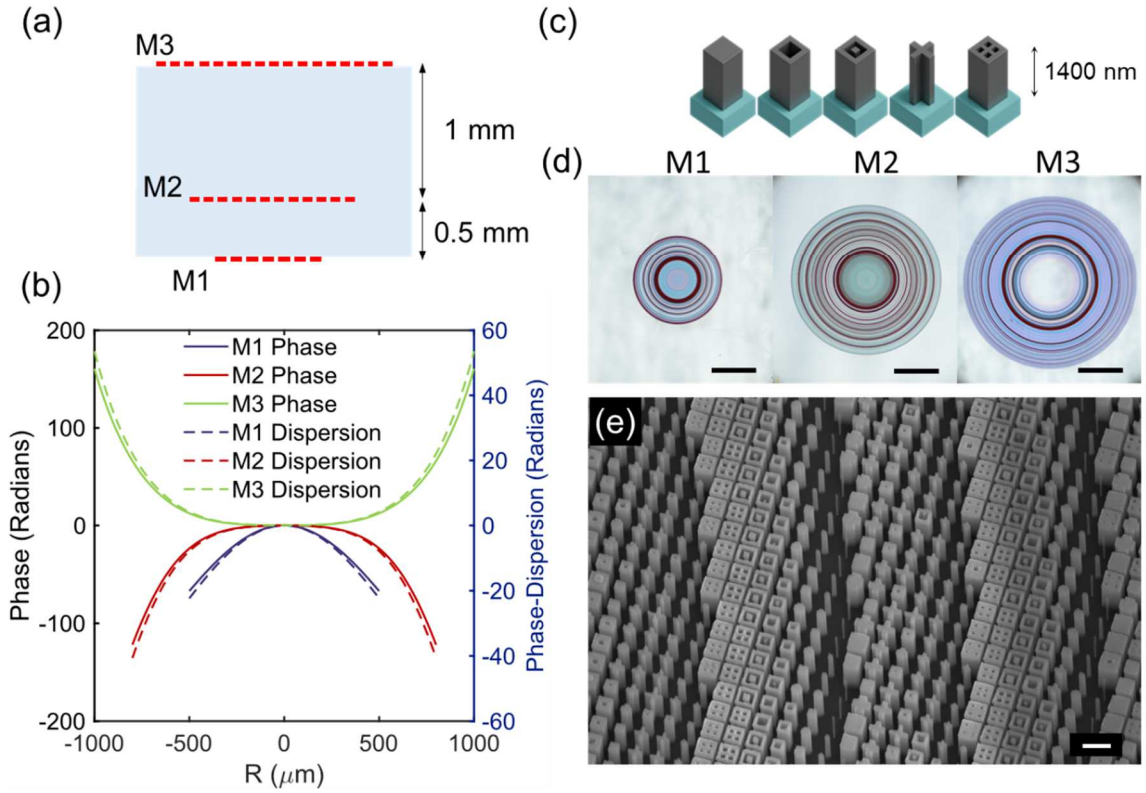

Figure 5.5: Metalens triplet. (a) Schematic of the metalens triplet. Each meta-element is fabricated on a 500 μm thick quartz wafer. (b) Required phase and dispersion profiles for each phase plate. (c) Amorphous silicon meta-unit archetypes utilized in realizing the metasurfaces. (d) Optical images of fabricated elements. Scale bar: 500 μm. (e) Scanning electron microscope image of a section of the fabricated metasurface. Scale bar:1 μm.

where δ is the radial coordinate and R is the radius of the "m-th" meta-element. This optimization is done for a single wavelength that lies in the desired operation wavelength range. To extend this monochromatic solution to a continuum of wavelengths, each metasurface must simultaneously satisfy the required phase function for all the wavelengths in the desired spectral range. That is, each metasurface must satisfy a phase profile and a phase dispersion profile for achromatic operation. Our approach, outlined previously [160], employs high-index dielectric nano-pillars with engineered cross-sectional shapes to provide wavelength dependent phase responses. By restricting the cross-sections to be four-fold symmetric and by only using five archetypes of cross-sectional shapes, we generate a library of polarization insensitive meta-atoms providing the maximum theoretically allowed coverage of phase dispersion determined by the wavelength-

dependent modal overlap between the meta-atom and the optical mode. Some example meta-atoms made of amorphous silicon and patterned on a fused quartz substrate are shown in Fig. 5.5a.

As derived in our previous work [160], the coverage of the phase-dispersion space by our meta-atom library sets a trade-off space between the maximum radius of a metalens and the numerical aperture (NA) for a given bandwidth. This trade-off applies equally to each of the three metasurfaces comprising the metalens triplet. Hence, the effective aperture size and the NA of the triplet system with chromatic aberration correction will be limited. Our choice of implementing a triplet instead of a doublet is motivated by the consideration that an additional element allows us to share the task of providing the range of phase-dispersion required for a fixed focusing power into two metasurfaces instead of one. The third metasurface is primarily responsible for correcting monochromatic aberrations. With these considerations, we have designed a metalens triplet composed of metasurfaces with radii of 0.4, 0.8 and 1 mm and a focal length defined from the last metasurface of 5 mm, resulting in an effective NA of 0.06. The spacings between the first and the second metasurfaces and between the second and the third are 0.5 mm and 1mm, respectively. The triplet is optimized to correct chromatic aberration for the wavelength range of 1300 – 1600 nm in the near-infrared with a field of view of 50°. A schematic of the optimized triplet system is shown in Fig. 5.5a. The phase and phase dispersion profiles resulting from the ray-tracing optimization (see Supplement section Table 5.1S1 for the coefficients) of the three metasurfaces are plotted in Fig. 5.5b for various wavelengths. We then use a phasor error minimization method to appropriately pick individual meta-atoms from our library to satisfy these phase and phase dispersion values at each position of the metasurfaces. The archetypes of meta-atoms used to populate these metasurfaces are shown in Fig. 5.5c. They are 1,400 nm tall amorphous silicon (a-Si) pillars arranged in a periodic lattice of 700 nm. The metasurfaces are fabricated by defining a hard mask on a-Si-on-quartz chips using electron beam lithography, followed by reactive ion etching (see Supplement 5.1S methods section for details). Alignment marks are defined on each of the chips for stacking purposes, which was done by mounting each individual metasurface on a separate 3D stage and bringing them together. We note here that ideally this process will be done

lithographically in more advanced nanofabrication facilities with higher precision. The optical images of the fabricated metasurfaces and scanning electron micrographs of individual meta-atoms are shown in Figs. 5.5d and 5.5e, respectively. We characterize (see methods section in supplementary for details) the performance of the triplets by measuring the 3D optical intensity distributions produced by the triplet system while illuminating it with a collimated beam with tunable wavelengths and incident angles using the setup shown in Fig. 5.1S4. The axial (X-Z cross-section) intensity distributions at normal incidence over a wavelength range of 1200 – 1600 nm are shown in Fig. 5.1S1a, demonstrating that chromatic aberration across the wavelength range is suppressed significantly. In Fig. 5.6a, we show the measured intensity distributions as a function of wavelength and angle of incidence at the designed focal plane (see Supplement 5.1S, Fig. 5.1S2 for simulation results), demonstrating close to diffraction-limited focusing up to an incident angle of 25 degrees for all the designed wavelengths. A comparison of line cuts through these focal spots and the diffraction-limited spots is shown in Fig. 5.1S1b. The asymmetric nature of some of the focal spots can be attributed to the misalignment and fabrication errors. The degradation of focal spots at 25 degrees for short wavelengths can be attributed to the excitation of multiple resonant modes at that angle of incidence. We compute the polychromatic modulation transfer function (MTF) (see Supplement Fig. 5.1S3 for monochromatic MTFs) from these measured focal plane intensities and plot them in Fig. 5.6b. The deviation away from the ideal diffraction limit of the MTF can be attributed to the reasons describe above and also the large pixel size (20 μm) of our near-infrared camera.

We also measure the focusing efficiency defined as the ratio of power in the focal spots over the power incident on the input aperture of the triplet system and show the result in Fig. 5.6c. An average focusing efficiency of 30% is observed for normal incidence over the entire wavelength range of operation. The sources of reduced efficiency in our system are fabrication errors, nearest neighbor coupling producing anomalous phase responses, and imperfect coverage of phase-

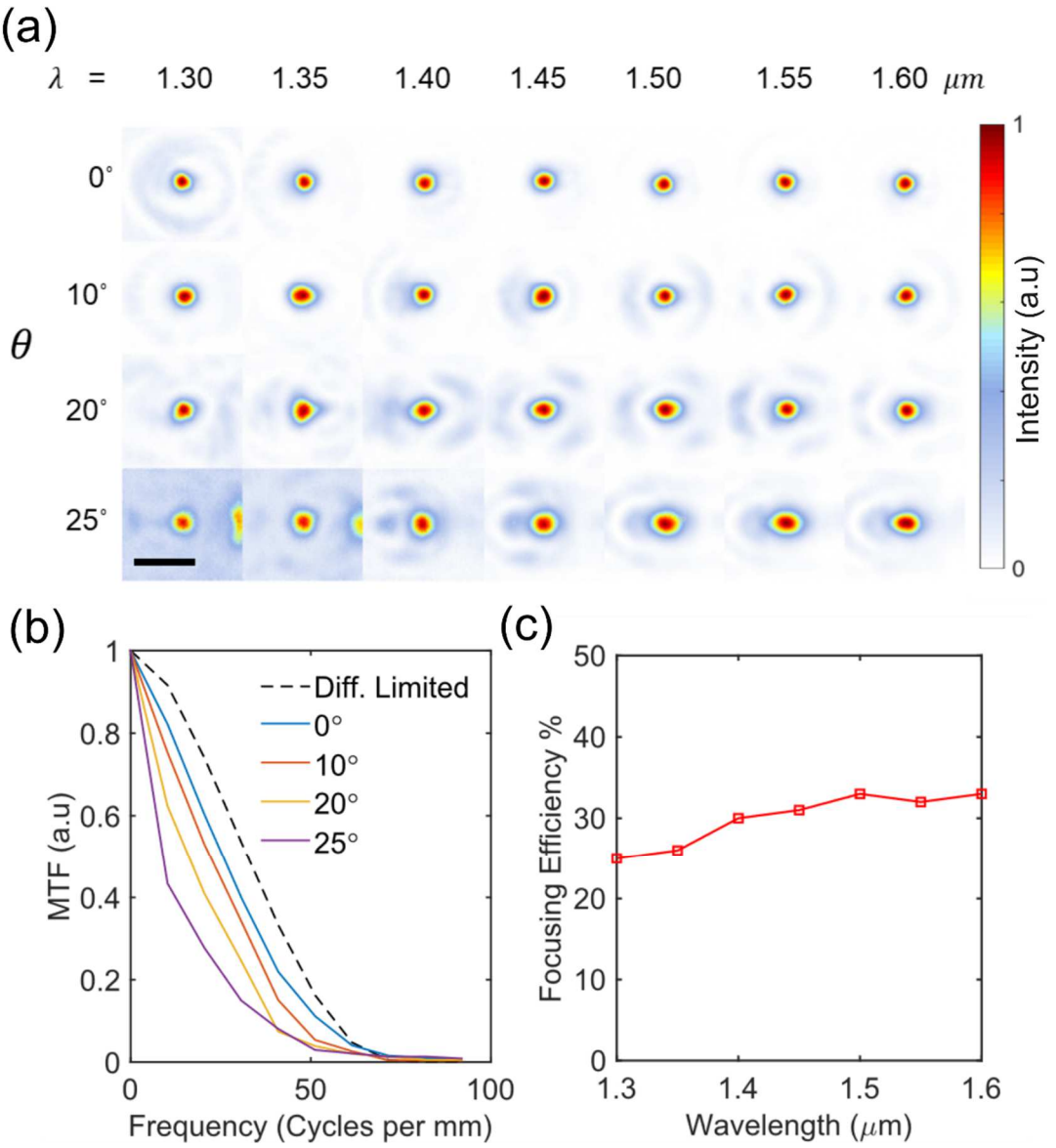

Figure 5.6: (a) Measured normalized focal plane intensity distributions for various wavelengths and angles of incidence. (b) Polychromatic modulation transfer function (MTF) calculated from (a) for select angles of incidence. (c) Measured focusing efficiency at normal incidence as a function of wavelength.

dispersion space by our meta-atom library producing a mismatch between the required and the provided response at certain positions. Additionally, lack of anti-reflection coating on the surfaces produces unwanted back reflection and further contributes to reduced efficiency of our system.

Using the setup shown in Fig. 5.1S5 and 5.1S6, we conduct broadband widefield imaging using the metalens triplet. A US Air Force resolution target transparency is illuminated with a

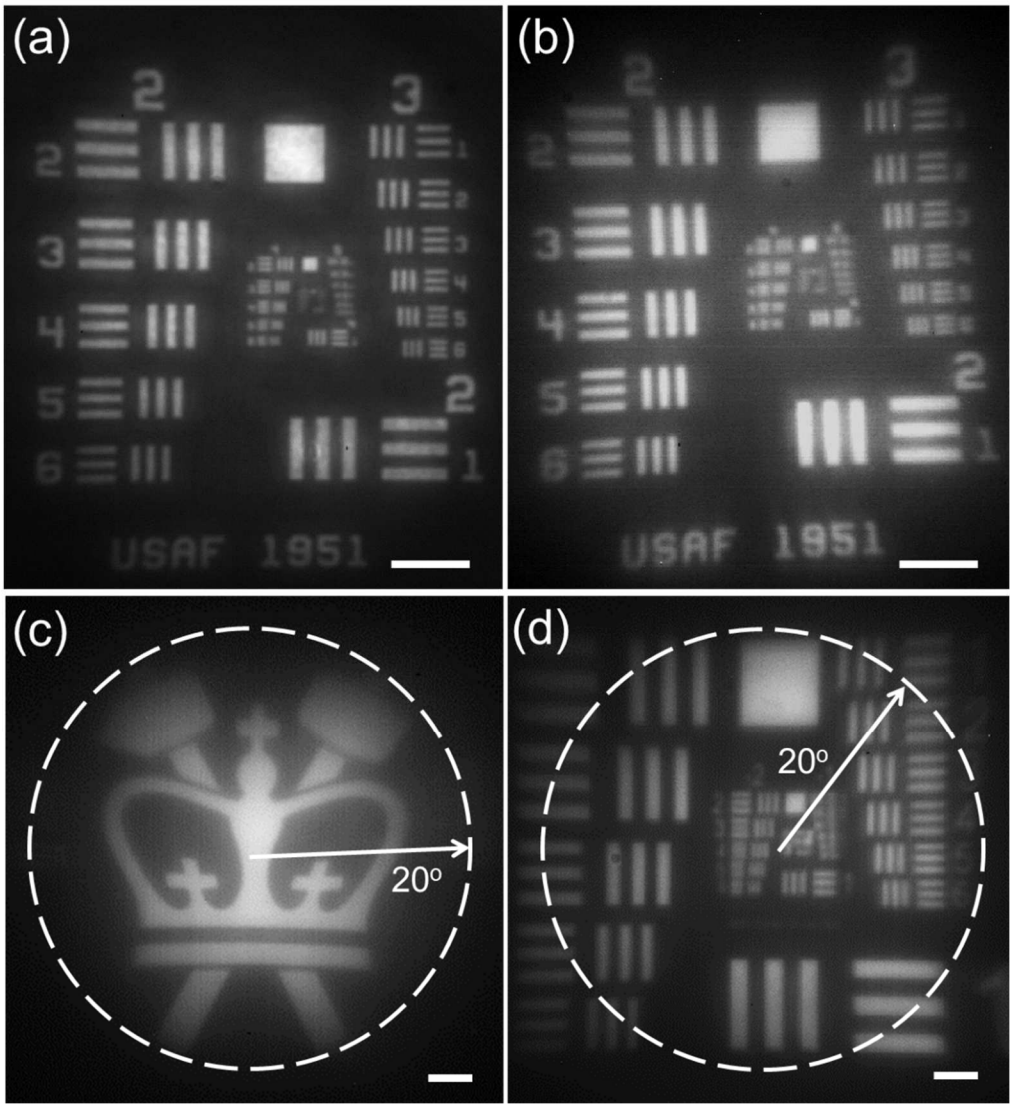

Figure 5.7. Imaging using the metasurface triplet. (a,b) Images, captured using the triplet, of the US Airforce resolution target transparency illuminated by a narrow linewidth telecom diode laser (a) and a broadband near-infrared source (b). Scale bar: 1 mm (c,d) Widefield images of Columbia Engineering logo and US Airforce target printouts illuminated by a broadband near-infrared source captured by the triplet. Dashed line represents ±20˚ FOV. Scale bar: 10 mm.

narrowband diode laser (λ=1,550 nm) and imaged using the triplet. A 10× objective and a tube lens are used to magnify and relay the image formed by the triplet to the camera sensor. To avoid speckles, a rotating diffuser plate is used before the transparency. The image captured by the sensor is shown in Fig. 5.7a. As a comparison, a halogen lamp producing broadband near-infrared

radiation (see Supplement 5.1S, Fig. 5.1S7 for its spectrum) is used to illuminate the same target and the image formed is shown in Fig. 5.7b.

We do not observe a significant presence of blur in the image that could be produced by defocus of different parts of the spectrum, illustrating the achromatic focusing capability of the triplet. We also image a print out of the Columbia Engineering logo that is 10 cm wide and placed 15 cm away from the triplet under the broadband near-infrared illumination generated by the halogen lamp. The image shown in Fig. 5.7c illustrates broadband monochromatic aberration correction within a FOV of ±20°. Figure 4d shows the image of a similarly sized resolution target placed at the same distance from the triplet as Fig. 5.7c.

Metasurface-based optical elements will become increasingly attractive for use in compact imaging systems if their overall performance can reach similar levels as their refractive elements-based counterparts. Our work outlines a methodology to realize optical aberration correction schemes in multi-element metasurface systems in order to achieve that goal. This design scheme can also be extended for non-imaging optical systems using multi-element metasurfaces such as spectrometers and holograms. We have demonstrated that such a system can be optimized by using ray-tracing approaches already used by professionals in this field and therefore expect to see increasing adoption of metasurfaces elements in hybrid refractive-diffractive systems for various applications.

Our design can be scaled to other wavelength ranges by appropriately choosing the materials platform. In particular, high-index transparent dielectric materials are highly suitable for producing meta-atoms with diverse phase and dispersion responses via structural engineering of the meta-atoms in addition to the intrinsic materials dispersion. Highly efficient dielectric metasurfaces in the visible have been reported using titanium dioxide [32] on quartz substrates as well as gallium nitride [137] on sapphire substrates.

In conclusion, we have outlined a design paradigm to realize simultaneous correction of chromatic and monochromatic aberrations in a metasurface triplet system. We experimentally demonstrated a metasurface triplet system working in the near-infrared and showed polarization

independent near-diffraction limited broadband imaging with a field of view spanning ± 20°. Metasurfaces can be lithographically stacked with high precision and can be mass manufactured on large wafers using conventional nanofabrication process lines. A significant advantage of metasurface-based optical systems is the possibility of direct integration of these elements on top of imaging sensors, which avoids the often-costly alignment process required when integrating refractive lens systems with image sensors in post-production. Leveraging such an integrated manufacturing process can reduce the cost and production time of high-performance optical systems particularly for compact optical systems for applications ranging from machine vision and metrology to virtual/augmented reality goggles and medical diagnostics.

Supplementary Section 5.1: Supplementary Information and Methods

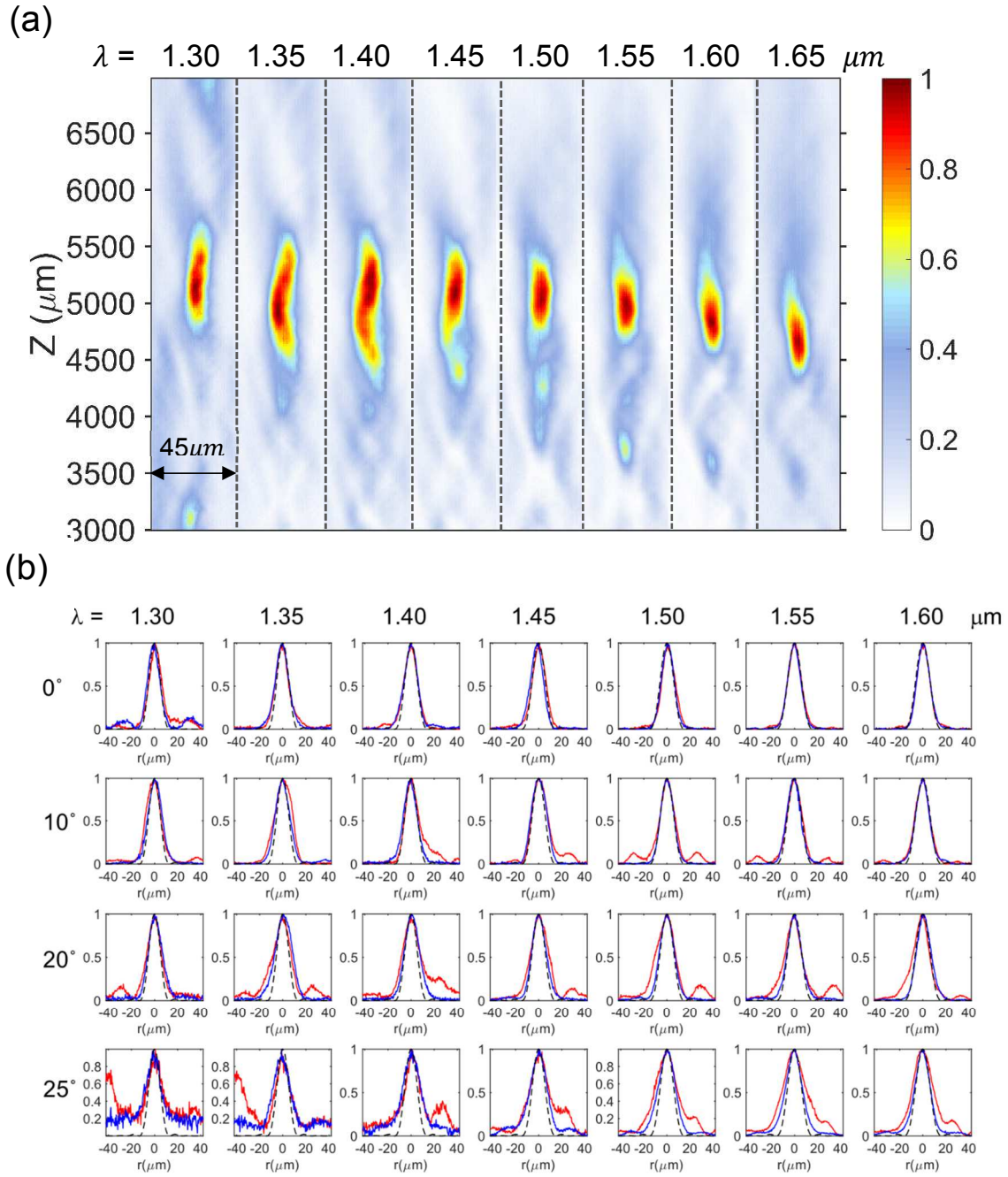

Figure 5.1S1:(a) Experimental normalized intensity distribution in the axial plane exiting the triplet for several wavelengths. (b) Measured focal plane intensity as a function of wavelength and angle of incidence plotted as axial line plots through X-axis(red) and Y-axis (blue). Dotted line represents the diffraction limited airy spot for the corresponding wavelength. Note the focal spot degradation is seen at 25 degrees incidence angle for shorter wavelengths

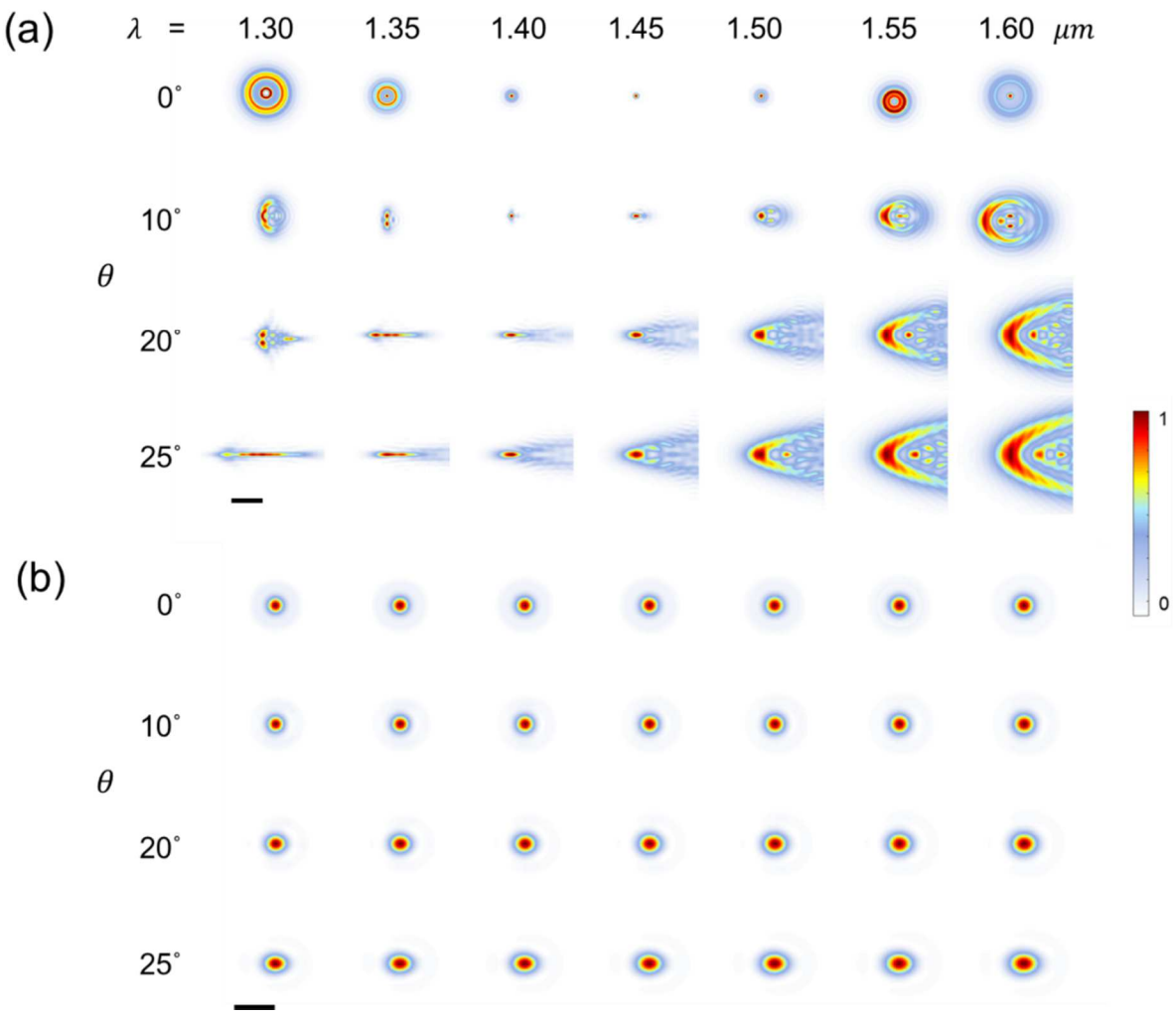

Figure 5.1S2: Comparison of focal plane intensity for a metasurface singlet and the designed triplet. The singlet has an aperture size of 1 mm and a focal length of 5 mm. (a) Simulated normalized focal plane intensity as a function of wavelength and angle of incidence for the singlet. Scale bar: 50 μm . We can see the effect of chromatic aberration in the defocus for normal incidence as a function of wavelength. At larger angle of incidence monochromatic aberration as well as chromatic aberration significantly distort the shape of the focal spot from the ideal. (b) Simulated normalized focal plane intensity as a function of wavelength and angle of incidence for the singlet. Scale bar: 25 μm. Significant suppression of focal spot distortion for all wavelengths and angle of incidence can be seen for the designed triplet.

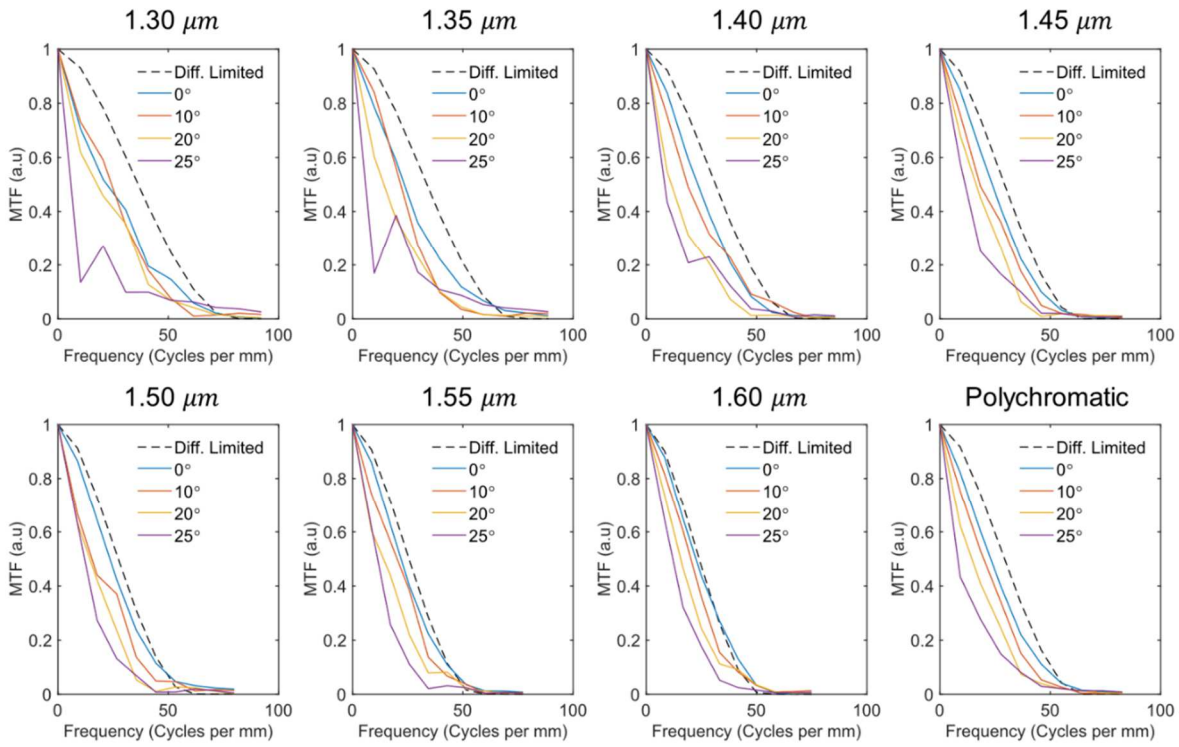

Figure 5.1S3. Calculated monochromatic modulation transfer function (MTF) for selected wavelengths from experimentally measured focal plane intensities. The weighted polychromatic MTF for comparison.

Table 5.1S1. Optimized coefficients for each individual meta-element derived from raytracing optimization

Meta-Element	Radius (μm)	a_1	a_2	a_3	a_4	a_5
M1	500	-82.7438	11.6717	0.6222	-2.5292	1.4984
M2	800	-19.7484	-103.8042	-38.5744	32.7715	-0.6754
M3	1000	16.8220	149.9195	-26.2600	32.9050	-1.9527

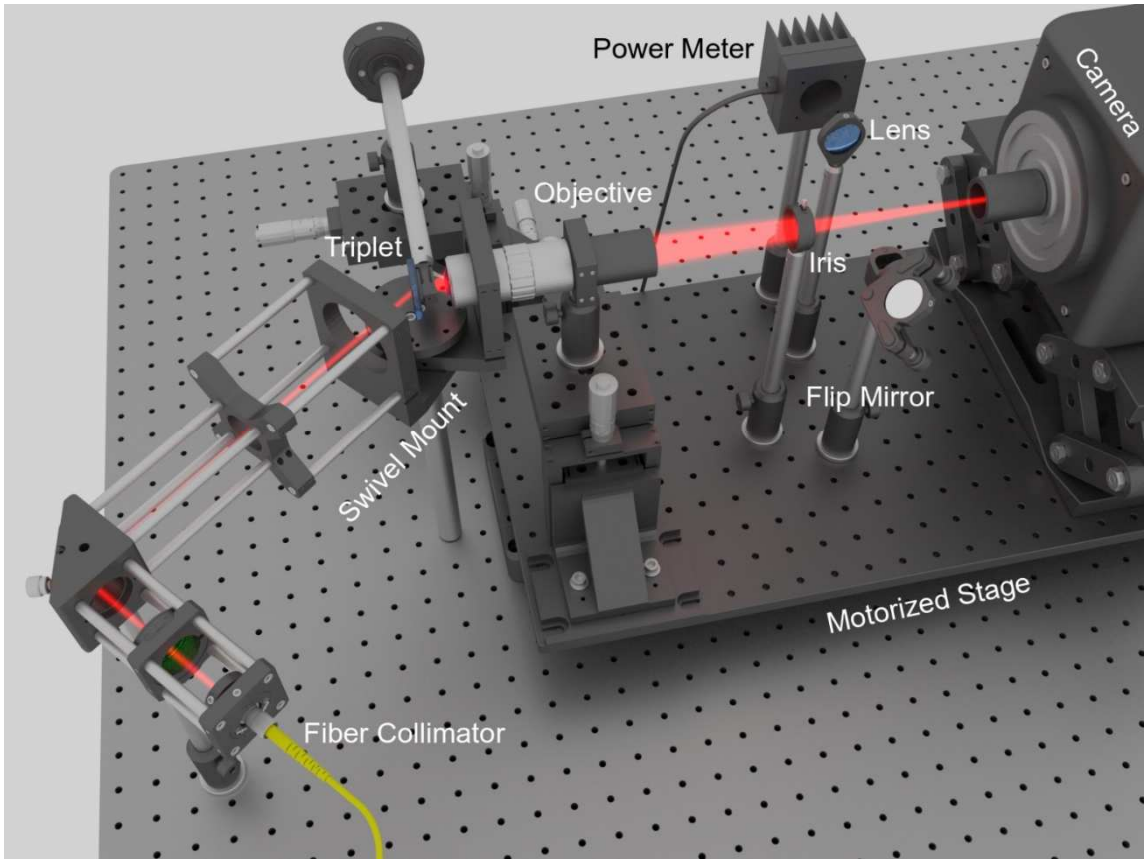

Figure 5.1S4. Measurement setup for measuring 3D intensity distribution of light exiting the triplet metalens. By utilizing the flip mirror, iris and the power meter, the same setup can measure focusing efficiency.

.

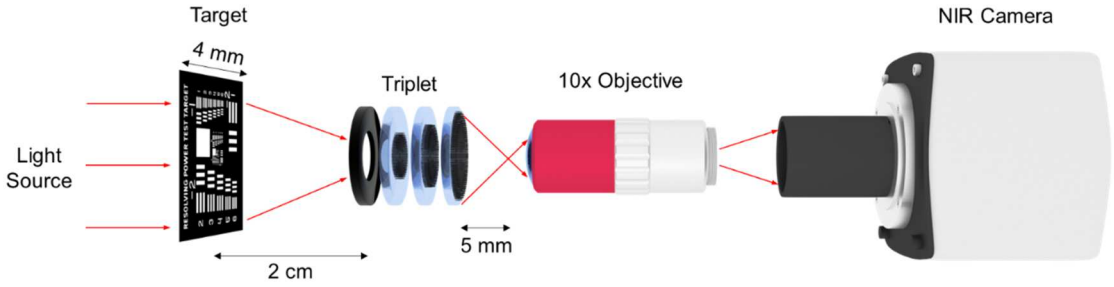

Figure 5.1S5: Imaging setup for characterizing the metalens triplet. For Fig. 4(a) in the main text, a narrowband diode laser (1550 nm) illuminates the US Airforce resolution target transparency (Thorlabs R1L1S1N) through a rotating diffuser to avoid speckles. For Fig 4(b) in the main text, the diode laser is replaced by a broadband halogen lamp.

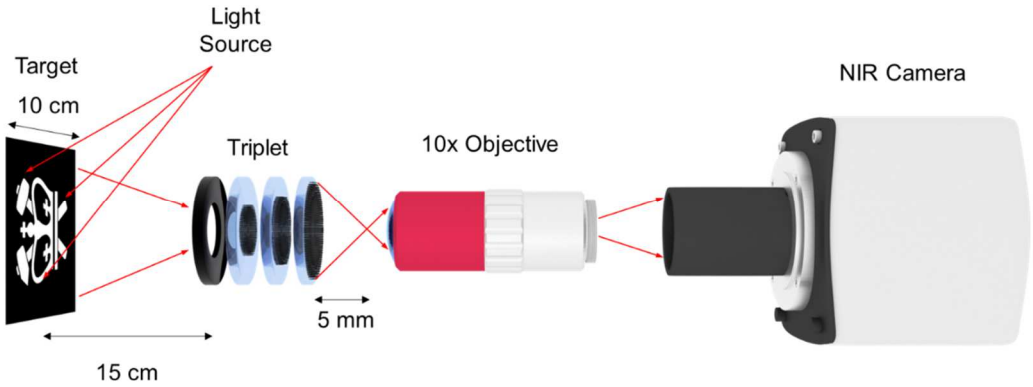

Figure 5.1S6: Imaging setup for characterizing the metalens triplet. For Fig. 4(a,b), a halogen lamp illuminates objects printed on a paper as shown in the figure. The metalens triplet captures the light reflected off of the paper target. The angular extent of the object is roughly equivalent to 40 degrees.

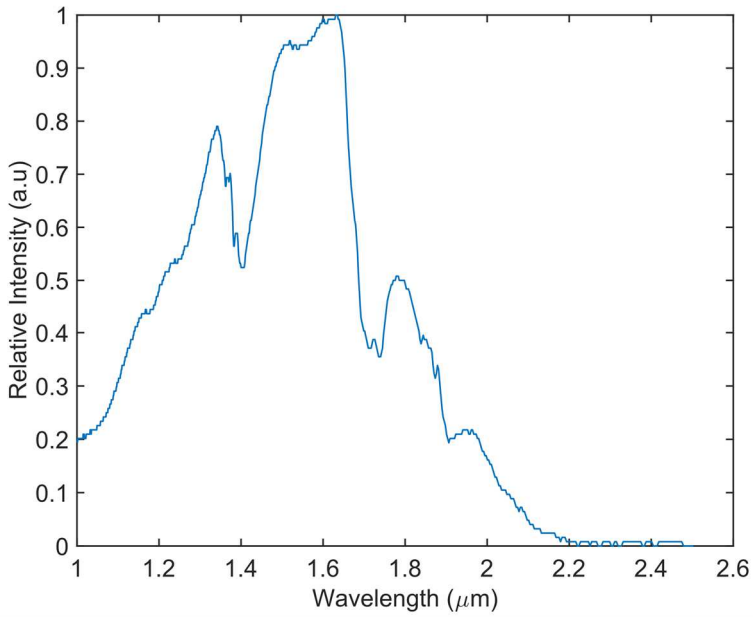

Figure 5.1S7: Halogen lamp spectrum. Fourier transform infrared spectroscopy measurement of the halogen lamp used to illuminate objects for imaging. Spectrum is normalized to peak intensity wavelength.

Metalens Triplet Fabrication.

500-μm fused quartz substrates are cleaned in acetone followed by isopropyl alcohol and deionized water bath and dried with nitrogen gun. Plasma enhanced physical vapor deposition (PECVD) is used to deposit Amorphous silicon (a-Si) films of thickness 1,400 nm at 200°C. Each meta-element of the triplet is defined using a JEOL JBX-6300FS electron beam lithography system on a double-layer resist (PMMA 495k A4 and 950A2) with a dose of 770 μC/cm^2 at a current of 200 pA on separate a-Si on quartz chips. A 20-nm layer of E-Spacer is spun on top of the double-layer resist to avoid the electron charging effect. After developing the resist in IPA:DI (3:1) for 2 minutes at 5°C, 20 nm of Aluminum Oxide is deposited using electron beam evaporation and lifted off in Remover 1165. The metasurface lens pattern is transferred to the Amorphous Silicon films by inductively coupled plasma etching in a mixture of SF_6 (40 sccm) and O_2 (16 sccm) at −100°C with ICP power of 800 W and RF power of 40 W. The middle meta-element is then encapsulated in silicon dioxide using PECVD.

Optical characterization.

For optical characterization of the fabricated metalens triplet, we used the setup depicted in Fig. 4a. The metalens triplet system are aligned together with 3 independent 3D stages using lithographically defined alignment marks. A wavelength tunable collimated laser beam obtained by passing a supercontinuum laser source (NKT SuperK Extreme) through a monochromator (Horiba iHR550) is incident on the input aperture of the metalens triplet. Light exiting the monochromator is coupled into a single mode fiber (Thorlabs P1-980A-FC) and then collimated using an adjustable aspheric fiber collimator (Thorlabs CFC-5X-B) with an anti-reflection coating for the 1,050-1,620 nm wavelength range. The angle of incident of the input laser beam can be changed by mounting the collimator on one end of a rotating swivel platform (Thorlabs PM4) with the triplet at the axis of rotation and the imaging optics on the other end. The light focused by the triplet is magnified by 100× objective (Mitutoyo Plan Apo NIR), a tube lens (Thorlabs AC254-200-C) of focal length 200 mm, and imaged using an InGaAs camera (Princeton Instruments Nirvana 640ST), which are mounted on a motorized stage. Metal nanostructures of known dimensions are imaged to calibrate

the magnification of our imaging system and any residual chromatic aberrations used for correction of measured data.

Transverse intensity distribution at various planes away from the triplets are imaged using the setup described above using the motorized stage. Such intensity distributions are measured at various wavelength using the monochromator grating angle. Thus, a 3D volume of intensity distribution is measured for each wavelength at normal incidence. A longitudinal 2D splice is taken from this dataset to produce Fig 4b. Similarly, focal planes of triplets are imaged at different wavelengths and angle of incidence using the rotation platform and keeping the motor position locked to the focal plane of the triplets. The result of this measurement is shown in Fig 4c.

For efficiency measurements of the metalenses, a flip-mirror and an iris are introduced before the InGaAs camera. The power transmitted through a metalens is measured by focusing the camera on the device plane and closing the iris to match the diameter of the metalens. The power is then passed to a power meter (Thorlabs SM05PD5A) using the flip mirror and a lens with 40 mm focal length. The incident power is measured by focusing the camera on an unpatterned region of the quartz substrate and recording the power with the iris set to the same diameter as the metalens. The ratio between transmitted and incident power defines transmission efficiency. To measure the focusing efficiency, the motor is first moved to the focal plane of the metalens and the iris is closed such that it corresponds to 3 to 5 times the FWHM of the focal spot. Then, the light is passed to the power meter. The ratio between measured focused power and incident power defines focusing efficiency.

Chapter 6: Conclusion and Outlook

Metasurfaces as a field has gained considerable interest due to its ability to provide unprecedented control of the optical wavefront. Using metasurfaces, both scalar and vector property of light can be engineered to realize optical functionalities that are not possible to achieve with conventional diffractive or refractive optical elements. Dielectric metasurfaces in particular have pushed the efficiencies of these novel devices to values that are acceptable for use in real world devices. Metasurfaces are ideal for use in compact optical systems where weight and size are constrained due to its flat form factor and subwavelength to near wavelength thickness. We therefore expect metasurfaces will increasingly find use in novel optical devices for applications in the areas such as machine vision, medical imaging and augmented/virtual reality.

There are however some limitations to this platform that may preclude its adoption in high end optical systems. In chapter 4, we derived a fundamental limit to the NA and diameter of a metalens that can be corrected for chromatic aberration. We showed that metalenses of diameters of 100 μm or smaller with low NA can be realized using dispersion engineering strategies. Other reports have reported similar limitations for bandwidth spanning the near-infrared or the visible wavelength range. However, even for miniature systems like cellphone cameras, diameters of about a millimeter are required. We therefore envision multielement designs that can push the diameters of the imaging systems. This opens up research avenues for exploring the degrees of freedom available in such multielement systems for realizing not only imaging systems but also novel multifunctional optical devices. In addition, metasurfaces can be utilized in conventional refractive optical systems to provide significantly better chromatic aberration correction than other optical elements [159]. We expect optical designers to incorporate similar strategies to optimize the performance of their systems or reduce its size.

Efficiency is another crucial figure of merit that metasurfaces need to improve upon to compete with state-of-the-art optical systems. For high NA optical devices, where the optical wavefront is bent at large angles, the efficiency of metasurface goes down significantly. Part of the

reason for this reduction in efficiency is the breaking down of local phase sampling assumption that is taken for granted when designing aperiodic metasurfaces. At such large angles, coupling effects between metaunits can dominate and the sampled phase might not be the same as single metaunit response. Similar breakdown of local phase approximation results in lowered efficiencies in dispersion engineered metasurfaces. It is computationally expensive to simulate all possible metaunits arrangements in aperiodic lattices to account for such coupling effects especially for very large metaunit libraries. We expect semi analytical methods like tight binding models or deep learning-based inference network could be used to significantly reduce the computational resources required to optimize such metasurface devices by accounting for coupling effects. Another computational approach called the inverse design [163–165] or adjoint method forgoes intuitive design framework and arrives at optimized metasurface design by gradient descent based optimization of all design parameters with only a forward and backward propagated simulation per step. This method has been used to design non-intuitive yet highly efficient high NA periodic metasurface grating devices [163]. We expect further development of this method directed towards optimizing aperiodic metasurfaces and utilizing the full 3D design space.

There are also several engineering challenges that need to be solved before metasurface based optical devices reach consumers. While fabrication of binary metasurfaces are compatible with conventional lithography techniques that have been developed by the silicon foundry industry for low cost mass manufacturing of computer and mobile chips, optical metasurface especially visible metasurfaces require high resolution lithography systems that have only been recently developed by the industry. As such tooling such foundries for high yield production of metasurface may require additional cost and development time. However, alternative fabrication techniques such as nanoimprint have been seen as promising avenues for realizing low cost metasurfaces.

Exploration of novel material platform is also crucial for development of highly efficient metasurfaces. Low loss high index dielectric materials can improve the efficiencies of metasurfaces [30] and we expect exploration novel material platform such as Aluminium Arsenide [166] for visible and high-index chalcogenide [167] materials for mid-infrared wavelengths. Opto-electronically active materials are perhaps even more desirable for

development of active metasurfaces. Such a metasurface based device, which can be actively modulated at high speed and can provide high resolution spatial light modulation is effectively the holy grail of this field. While several material platforms have been utilized to demonstrate [168,169] active modulation of optical wavefronts, we are far from realizing practical devices that can compete with conventional liquid crystal or digital mirror based spatial light modulators. We hope that continued research into fundamentals of metasurfaces and novel material platforms will allow for practical realization of such a device in the future.

Bibliography

1. C. Huygens, *Traité de la lumière* (A Leide : Chez Pierre vander Aa, marchand libraire, 1690).

2. N. Yu, P. Genevet, M. A. Kats, F. Aieta, J.-P. Tetienne, F. Capasso, and Z. Gaburro, "Light Propagation with Phase Discontinuities: Generalized Laws of Reflection and Refraction," Science **334**, 333–337 (2011).

3. N. Meinzer, W. L. Barnes, and I. R. Hooper, "Plasmonic meta-atoms and metasurfaces," Nat. Photonics **8**, 889–898 (2014).

4. S. Uda, *On the Wireless Beam of Short Electric Waves* (Institute of electrical engineers of Japan, 1927).

5. J. Huang, "Planar microstrip Yagi array antenna," in *Digest on Antennas and Propagation Society International Symposium* (1989), pp. 894–897 vol.2.

6. D. M. Pozar and T. A. Metzler, "Analysis of a reflectarray antenna using microstrip patches of variable size," Electron. Lett. **29**, 657–658 (1993).

7. P. Nayeri, F. Yang, and A. Z. Elsherbeni, *Reflectarray Antennas: Theory, Designs, and Applications*, 1 edition (Wiley-IEEE Press, 2018).

8. E. Carrasco and J. A. Encinar, "Reflectarray antennas: A review," 16 (n.d.).

9. P. R. West, S. Ishii, G. V. Naik, N. K. Emani, V. M. Shalaev, and A. Boltasseva, "Searching for better plasmonic materials," Laser Photonics Rev. **4**, 795–808 (2010).

10. D. K. Gramotnev and S. I. Bozhevolnyi, "Plasmonics beyond the diffraction limit," Nat. Photonics **4**, 83–91 (2010).

11. L. Huang, X. Chen, H. Mühlenbernd, G. Li, B. Bai, Q. Tan, G. Jin, T. Zentgraf, and S. Zhang, "Dispersionless Phase Discontinuities for Controlling Light Propagation," Nano Lett. **12**, 5750–5755 (2012).

12. Y.-W. Huang, W. T. Chen, W.-Y. Tsai, P. C. Wu, C.-M. Wang, G. Sun, and D. P. Tsai, "Aluminum Plasmonic Multicolor Meta-Hologram," Nano Lett. **15**, 3122–3127 (2015).

13. F. Aieta, P. Genevet, M. A. Kats, N. Yu, R. Blanchard, Z. Gaburro, and F. Capasso, "Aberration-Free Ultrathin Flat Lenses and Axicons at Telecom Wavelengths Based on Plasmonic Metasurfaces," Nano Lett. **12**, 4932–4936 (2012).

14. X. Ni, N. K. Emani, A. V. Kildishev, A. Boltasseva, and V. M. Shalaev, "Broadband Light Bending with Plasmonic Nanoantennas," Science **335**, 427–427 (2012).

15. X. Ni, A. V. Kildishev, and V. M. Shalaev, "Metasurface holograms for visible light," Nat. Commun. **4**, ncomms3807 (2013).

16. A. Pors, M. G. Nielsen, R. L. Eriksen, and S. I. Bozhevolnyi, "Broadband Focusing Flat Mirrors Based on Plasmonic Gradient Metasurfaces," Nano Lett. **13**, 829–834 (2013).

17. T. D. Corrigan, P. W. Kolb, A. B. Sushkov, H. D. Drew, D. C. Schmadel, and R. J. Phaneuf, "Optical plasmonic resonances in split-ring resonator structures: an improved LC model," Opt. Express **16**, 19850–19864 (2008).

18. M. W. Klein, C. Enkrich, M. Wegener, C. M. Soukoulis, and S. Linden, "Single-slit split-ring resonators at optical frequencies: limits of size scaling," Opt. Lett. **31**, 1259–1261 (2006).

19. D. R. Smith, J. B. Pendry, and M. C. K. Wiltshire, "Metamaterials and Negative Refractive Index," Science **305**, 788–792 (2004).

20. V. M. Shalaev, "Optical negative-index metamaterials," Nat. Photonics **1**, 41–48 (2007).

21. G. Zheng, H. Mühlenbernd, M. Kenney, G. Li, T. Zentgraf, and S. Zhang, "Metasurface holograms reaching 80% efficiency," Nat. Nanotechnol. **10**, 308–312 (2015).

22. S. Sun, K.-Y. Yang, C.-M. Wang, T.-K. Juan, W. T. Chen, C. Y. Liao, Q. He, S. Xiao, W.-T. Kung, G.-Y. Guo, L. Zhou, and D. P. Tsai, "High-Efficiency Broadband Anomalous Reflection by Gradient Meta-Surfaces," Nano Lett. **12**, 6223–6229 (2012).

23. P. Lalanne, S. Astilean, P. Chavel, E. Cambril, and H. Launois, "Blazed binary subwavelength gratings with efficiencies larger than those of conventional échelette gratings," Opt. Lett. **23**, 1081–1083 (1998).

24. P. Lalanne, S. Astilean, P. Chavel, E. Cambril, and H. Launois, "Design and fabrication of blazed binary diffractive elements with sampling periods smaller than the structural cutoff," JOSA A **16**, 1143–1156 (1999).

25. A. Arbabi, Y. Horie, M. Bagheri, and A. Faraon, "Dielectric metasurfaces for complete control of phase and polarization with subwavelength spatial resolution and high transmission," Nat. Nanotechnol. **10**, 937–943 (2015).

26. E. Arbabi, A. Arbabi, S. M. Kamali, Y. Horie, and A. Faraon, "High efficiency double-wavelength dielectric metasurface lenses with dichroic birefringent meta-atoms," Opt. Express **24**, 18468–18477 (2016).

27. P. Lalanne, "Waveguiding in blazed-binary diffractive elements," JOSA A **16**, 2517–2520 (1999).

28. D. Fattal, J. Li, Z. Peng, M. Fiorentino, and R. G. Beausoleil, "Flat dielectric grating reflectors with focusing abilities," Nat. Photonics **4**, 466–470 (2010).

29. A. Arbabi, Y. Horie, A. J. Ball, M. Bagheri, and A. Faraon, "Subwavelength-thick lenses with high numerical apertures and large efficiency based on high-contrast transmitarrays," Nat. Commun. **6**, 7069 (2015).

30. J. Yang and J. A. Fan, "Analysis of material selection on dielectric metasurface performance," Opt. Express **25**, 23899–23909 (2017).

31. P. Qiao, W. Yang, and C. J. Chang-Hasnain, "Recent advances in high-contrast metastructures, metasurfaces, and photonic crystals," Adv. Opt. Photonics **10**, 180–245 (2018).

32. M. Khorasaninejad, W. T. Chen, R. C. Devlin, J. Oh, A. Y. Zhu, and F. Capasso, "Metalenses at visible wavelengths: Diffraction-limited focusing and subwavelength resolution imaging," Science **352**, 1190–1194 (2016).

33. M. Khorasaninejad, A. Y. Zhu, C. Roques-Carmes, W. T. Chen, J. Oh, I. Mishra, R. C. Devlin, and F. Capasso, "Polarization-Insensitive Metalenses at Visible Wavelengths," Nano Lett. **16**, 7229–7234 (2016).

34. P. Lalanne and P. Chavel, "Metalenses at visible wavelengths: past, present, perspectives," Laser Photonics Rev. **11**, 1600295 (2017).

35. S. Gao, C.-S. Park, S.-S. Lee, and D.-Y. Choi, "A Highly Efficient Bifunctional Dielectric Metasurface Enabling Polarization-Tuned Focusing and Deflection for Visible Light," Adv. Opt. Mater. **7**, 1801337 (2019).

36. R. C. Devlin, M. Khorasaninejad, W. T. Chen, J. Oh, and F. Capasso, "Broadband high-efficiency dielectric metasurfaces for the visible spectrum," Proc. Natl. Acad. Sci. **113**, 10473–10478 (2016).

37. S. Pancharatnam, "Generalized theory of interference, and its applications. Part I. Coherent pencils," Proc. Indian Acad. Sci. Sect. A **44**, 247–262 (1956).

38. M. V. Berry, "The Adiabatic Phase and Pancharatnam's Phase for Polarized Light," J. Mod. Opt. **34**, 1401–1407 (1987).

39. Z. Bomzon, V. Kleiner, and E. Hasman, "Pancharatnam–Berry phase in space-variant polarization-state manipulations with subwavelength gratings," Opt. Lett. **26**, 1424–1426 (2001).

40. S. Xiao, J. Wang, F. Liu, S. Zhang, X. Yin, and J. Li, "Spin-dependent optics with metasurfaces," Nanophotonics **6**, 215–234 (2017).

41. R. C. Jones, "A New Calculus for the Treatment of Optical SystemsI. Description and Discussion of the Calculus," JOSA **31**, 488–493 (1941).

42. A. C. Overvig, S. Shrestha, S. C. Malek, M. Lu, A. Stein, C. Zheng, and N. Yu, "Dielectric Metasurfaces for Complete and Independent Control of Optical Amplitude and Phase," ArXiv190300578 Phys. (2019).

43. J. P. Balthasar Mueller, N. A. Rubin, R. C. Devlin, B. Groever, and F. Capasso, "Metasurface Polarization Optics: Independent Phase Control of Arbitrary Orthogonal States of Polarization," Phys. Rev. Lett. **118**, 113901 (2017).

44. R. C. Devlin, A. Ambrosio, N. A. Rubin, J. P. B. Mueller, and F. Capasso, "Arbitrary spin-to–orbital angular momentum conversion of light," Science **358**, 896–901 (2017).

45. A. E. H. Love, "I. The integration of the equations of propagation of electric waves," Philos. Trans. R. Soc. Lond. Ser. Contain. Pap. Math. Phys. Character **197**, 1–45 (1901).

46. M. Decker, I. Staude, M. Falkner, J. Dominguez, D. N. Neshev, I. Brener, T. Pertsch, and Y. S. Kivshar, "High-Efficiency Dielectric Huygens' Surfaces," Adv. Opt. Mater. **3**, 813–820 (2015).

47. C. Pfeiffer and A. Grbic, "Metamaterial Huygens' Surfaces: Tailoring Wave Fronts with Reflectionless Sheets," Phys. Rev. Lett. **110**, 197401 (2013).

48. C. Pfeiffer, N. K. Emani, A. M. Shaltout, A. Boltasseva, V. M. Shalaev, and A. Grbic, "Efficient Light Bending with Isotropic Metamaterial Huygens' Surfaces," Nano Lett. **14**, 2491–2497 (2014).

49. S. Shrestha, Y. Wang, A. C. Overvig, M. Lu, A. Stein, L. D. Negro, and N. Yu, "Indium Tin Oxide Broadband Metasurface Absorber," ACS Photonics **5**, 3526–3533 (2018).

50. N. I. Zheludev and Y. S. Kivshar, "From metamaterials to metadevices," Nat. Mater. **11**, 917–924 (2012).

51. N. Yu and F. Capasso, "Flat optics with designer metasurfaces," Nat. Mater. **13**, 139–150 (2014).

52. N. Mohammadi Estakhri and A. Alù, "Wave-front Transformation with Gradient Metasurfaces," Phys. Rev. X **6**, 041008 (2016).

53. M. Kim, J. Jeong, J. K. S. Poon, and G. V. Eleftheriades, "Vanadium-dioxide-assisted digital optical metasurfaces for dynamic wavefront engineering," JOSA B **33**, 980–988 (2016).

54. H.-T. Chen, W. J. Padilla, M. J. Cich, A. K. Azad, R. D. Averitt, and A. J. Taylor, "A metamaterial solid-state terahertz phase modulator," Nat. Photonics **3**, 148–151 (2009).

55. H.-T. Chen, W. J. Padilla, J. M. O. Zide, A. C. Gossard, A. J. Taylor, and R. D. Averitt, "Active terahertz metamaterial devices," Nature **444**, 597–600 (2006).

56. C. Wu, B. N. III, J. John, A. Milder, B. Zollars, S. Savoy, and G. Shvets, "Metamaterial-based integrated plasmonic absorber/emitter for solar thermo-photovoltaic systems," J. Opt. **14**, 024005 (2012).

57. J. Zhu, Z. Yu, G. F. Burkhard, C.-M. Hsu, S. T. Connor, Y. Xu, Q. Wang, M. McGehee, S. Fan, and Y. Cui, "Optical Absorption Enhancement in Amorphous Silicon Nanowire and Nanocone Arrays," Nano Lett. **9**, 279–282 (2009).

58. H. Wang, V. Prasad Sivan, A. Mitchell, G. Rosengarten, P. Phelan, and L. Wang, "Highly efficient selective metamaterial absorber for high-temperature solar thermal energy harvesting," Sol. Energy Mater. Sol. Cells **137**, 235–242 (2015).

59. J. J. Talghader, A. S. Gawarikar, and R. P. Shea, "Spectral selectivity in infrared thermal detection," Light Sci. Appl. **1**, e24 (2012).

60. N. I. Landy, C. M. Bingham, T. Tyler, N. Jokerst, D. R. Smith, and W. J. Padilla, "Design, theory, and measurement of a polarization-insensitive absorber for terahertz imaging," Phys. Rev. B **79**, 125104 (2009).

61. N. Liu, M. Mesch, T. Weiss, M. Hentschel, and H. Giessen, "Infrared Perfect Absorber and Its Application As Plasmonic Sensor," Nano Lett. **10**, 2342–2348 (2010).

62. W. Li and J. Valentine, "Metamaterial Perfect Absorber Based Hot Electron Photodetection," Nano Lett. **14**, 3510–3514 (2014).

63. P. N. Dyachenko, S. Molesky, A. Y. Petrov, M. Störmer, T. Krekeler, S. Lang, M. Ritter, Z. Jacob, and M. Eich, "Controlling thermal emission with refractory epsilon-near-zero metamaterials via topological transitions," Nat. Commun. **7**, 11809 (2016).

64. X. Liu, T. Tyler, T. Starr, A. F. Starr, N. M. Jokerst, and W. J. Padilla, "Taming the Blackbody with Infrared Metamaterials as Selective Thermal Emitters," Phys. Rev. Lett. **107**, 045901 (2011).

65. G. D'Aguanno, N. Mattiucci, A. Alù, C. Argyropoulos, J. V. Foreman, and M. J. Bloemer, "Thermal emission from a metamaterial wire medium slab," Opt. Express **20**, 9784–9789 (2012).

66. C. Fu and Z. M. Zhang, "Thermal radiative properties of metamaterials and other nanostructured materials: A review," Front. Energy Power Eng. China **3**, 11–26 (2009).

67. M. K. Hedayati, M. Javaherirahim, B. Mozooni, R. Abdelaziz, A. Tavassolizadeh, V. S. K. Chakravadhanula, V. Zaporojtchenko, T. Strunkus, F. Faupel, and M. Elbahri, "Design of a Perfect Black Absorber at Visible Frequencies Using Plasmonic Metamaterials," Adv. Mater. **23**, 5410–5414 (2011).

68. T. Cao, C. Wei, R. E. Simpson, L. Zhang, and M. J. Cryan, "Broadband Polarization-Independent Perfect Absorber Using a Phase-Change Metamaterial at Visible Frequencies," Sci. Rep. **4**, 3955 (2014).

69. H. Wang and L. Wang, "Perfect selective metamaterial solar absorbers," Opt. Express **21**, A1078–A1093 (2013).

70. X. Liu, T. Starr, A. F. Starr, and W. J. Padilla, "Infrared Spatial and Frequency Selective Metamaterial with Near-Unity Absorbance," Phys. Rev. Lett. **104**, 207403 (2010).

71. F. Ding, J. Dai, Y. Chen, J. Zhu, Y. Jin, and S. I. Bozhevolnyi, "Broadband near-infrared metamaterial absorbers utilizing highly lossy metals," Sci. Rep. **6**, 39445 (2016).

72. M. Diem, T. Koschny, and C. M. Soukoulis, "Wide-angle perfect absorber/thermal emitter in the terahertz regime," Phys. Rev. B **79**, 033101 (2009).

73. H. A. Atwater and A. Polman, "Plasmonics for improved photovoltaic devices," Nat. Mater. **9**, 205–213 (2010).

74. B. Li, J. Lin, J. Lu, X. Su, and J. Li, "Light absorption enhancement in thin-film solar cells by embedded lossless silica nanoparticles," J. Opt. **15**, 055005 (2013).

75. S. Carretero-Palacios, M. E. Calvo, and H. Míguez, "Absorption Enhancement in Organic–Inorganic Halide Perovskite Films with Embedded Plasmonic Gold Nanoparticles," J. Phys. Chem. C **119**, 18635–18640 (2015).

76. K. Tvingstedt, N.-K. Persson, O. Inganäs, A. Rahachou, and I. V. Zozoulenko, "Surface plasmon increase absorption in polymer photovoltaic cells," Appl. Phys. Lett. **91**, 113514 (2007).

77. F. Ding, Y. Jin, B. Li, H. Cheng, L. Mo, and S. He, "Ultrabroadband strong light absorption based on thin multilayered metamaterials," Laser Photonics Rev. **8**, 946–953 (2014).

78. Y. Cui, K. H. Fung, J. Xu, H. Ma, Y. Jin, S. He, and N. X. Fang, "Ultrabroadband Light Absorption by a Sawtooth Anisotropic Metamaterial Slab," Nano Lett. **12**, 1443–1447 (2012).

79. N. I. Landy, S. Sajuyigbe, J. J. Mock, D. R. Smith, and W. J. Padilla, "Perfect Metamaterial Absorber," Phys. Rev. Lett. **100**, 207402 (2008).

80. K. Aydin, V. E. Ferry, R. M. Briggs, and H. A. Atwater, "Broadband polarization-independent resonant light absorption using ultrathin plasmonic super absorbers," Nat. Commun. **2**, 517 (2011).

81. Y. Q. Ye, Y. Jin, and S. He, "Omnidirectional, polarization-insensitive and broadband thin absorber in the terahertz regime," JOSA B **27**, 498–504 (2010).

82. J. Mandal, D. Wang, A. C. Overvig, N. N. Shi, D. Paley, A. Zangiabadi, Q. Cheng, K. Barmak, N. Yu, and Y. Yang, "Scalable, “Dip-and-Dry” Fabrication of a Wide-Angle Plasmonic Selective Absorber for High-Efficiency Solar–Thermal Energy Conversion," Adv. Mater. **29**, 1702156 (2017).

83. B. Zhang, Y. Zhao, Q. Hao, B. Kiraly, I.-C. Khoo, S. Chen, and T. J. Huang, "Polarization-independent dual-band infrared perfect absorber based on a metal-dielectric-metal elliptical nanodisk array," Opt. Express **19**, 15221–15228 (2011).

84. Y. Cui, J. Xu, K. Hung Fung, Y. Jin, A. Kumar, S. He, and N. X. Fang, "A thin film broadband absorber based on multi-sized nanoantennas," Appl. Phys. Lett. **99**, 253101 (2011).

85. H. Xiong, J.-S. Hong, C.-M. Luo, and L.-L. Zhong, "An ultrathin and broadband metamaterial absorber using multi-layer structures," J. Appl. Phys. **114**, 064109 (2013).

86. D. Wen, H. Yang, Q. Ye, M. Li, L. Guo, and J. Zhang, "Broadband metamaterial absorber based on a multi-layer structure," Phys. Scr. **88**, 015402 (2013).

87. J. A. Bossard, L. Lin, S. Yun, L. Liu, D. H. Werner, and T. S. Mayer, "Near-Ideal Optical Metamaterial Absorbers with Super-Octave Bandwidth," ACS Nano **8**, 1517–1524 (2014).

88. A. Capretti, Y. Wang, N. Engheta, and L. D. Negro, "Enhanced third-harmonic generation in Si-compatible epsilon-near-zero indium tin oxide nanolayers," Opt. Lett. **40**, 1500–1503 (2015).

89. A. Capretti, Y. Wang, N. Engheta, and L. Dal Negro, "Comparative Study of Second-Harmonic Generation from Epsilon-Near-Zero Indium Tin Oxide and Titanium Nitride Nanolayers Excited in the Near-Infrared Spectral Range," ACS Photonics **2**, 1584–1591 (2015).

90. H. Zhao, Y. Wang, A. Capretti, L. D. Negro, and J. Klamkin, "Broadband Electroabsorption Modulators Design Based on Epsilon-Near-Zero Indium Tin Oxide," IEEE J. Sel. Top. Quantum Electron. **21**, 192–198 (2015).

91. S. H. Brewer and S. Franzen, "Optical properties of indium tin oxide and fluorine-doped tin oxide surfaces: correlation of reflectivity, skin depth, and plasmon frequency with conductivity," J. Alloys Compd. **338**, 73–79 (2002).

92. S. Franzen, "Surface Plasmon Polaritons and Screened Plasma Absorption in Indium Tin Oxide Compared to Silver and Gold," J. Phys. Chem. C **112**, 6027–6032 (2008).

93. Y. Wang, A. Capretti, and L. D. Negro, "Wide tuning of the optical and structural properties of alternative plasmonic materials," Opt. Mater. Express **5**, 2415–2430 (2015).

94. Y. Wang, A. C. Overvig, S. Shrestha, R. Zhang, R. Wang, N. Yu, and L. D. Negro, "Tunability of indium tin oxide materials for mid-infrared plasmonics applications," Opt. Mater. Express **7**, 2727–2739 (2017).

95. J. Yoon, M. Zhou, M. A. Badsha, T. Y. Kim, Y. C. Jun, and C. K. Hwangbo, "Broadband Epsilon-Near-Zero Perfect Absorption in the Near-Infrared," Sci. Rep. **5**, 12788 (2015).

96. M. H. Javani and M. I. Stockman, "Real and Imaginary Properties of Epsilon-Near-Zero Materials," Phys. Rev. Lett. **117**, 107404 (2016).

97. A. Yariv and P. Yeh, *Photonics: Optical Electronics in Modern Communications*, 6 edition (Oxford University Press, 2006).

98. H.-T. Chen, "Interference theory of metamaterial perfect absorbers," Opt. Express **20**, 7165–7172 (2012).

99. E. Arbabi, A. Arbabi, S. M. Kamali, Y. Horie, and A. Faraon, "Multiwavelength metasurfaces through spatial multiplexing," Sci. Rep. **6**, srep32803 (2016).

100. B. Wang, F. Dong, Q.-T. Li, D. Yang, C. Sun, J. Chen, Z. Song, L. Xu, W. Chu, Y.-F. Xiao, Q. Gong, and Y. Li, "Visible-Frequency Dielectric Metasurfaces for Multiwavelength Achromatic and Highly Dispersive Holograms," Nano Lett. **16**, 5235–5240 (2016).

101. X. Li, L. Chen, Y. Li, X. Zhang, M. Pu, Z. Zhao, X. Ma, Y. Wang, M. Hong, and X. Luo, "Multicolor 3D meta-holography by broadband plasmonic modulation," Sci. Adv. **2**, e1601102 (2016).

102. S. M. Kamali, E. Arbabi, A. Arbabi, Y. Horie, M. Faraji-Dana, and A. Faraon, "Angle-Multiplexed Metasurfaces: Encoding Independent Wavefronts in a Single Metasurface under Different Illumination Angles," Phys. Rev. X **7**, 041056 (2017).

103. B. Wang, F. Dong, D. Yang, Z. Song, L. Xu, W. Chu, Q. Gong, and Y. Li, "Polarization-controlled color-tunable holograms with dielectric metasurfaces," Optica **4**, 1368–1371 (2017).

104. Z. Shi, M. Khorasaninejad, Y.-W. Huang, C. Roques-Carmes, A. Y. Zhu, W. T. Chen, V. Sanjeev, Z.-W. Ding, M. Tamagnone, K. Chaudhary, R. C. Devlin, C.-W. Qiu, and F. Capasso, "Single-Layer Metasurface with Controllable Multiwavelength Functions," Nano Lett. **18**, 2420–2427 (2018).

105. J. M. Geary, *Introduction to Lens Design: With Practical ZEMAX Examples* (Willmann-Bell, 2002).

106. D. Lin, P. Fan, E. Hasman, and M. L. Brongersma, "Dielectric gradient metasurface optical elements," Science **345**, 298–302 (2014).

107. H. Tamura, T. Unakami, J. He, Y. Miyamoto, and K. Nakagawa, "Highly uniform holographic microtrap arrays for single atom trapping using a feedback optimization of in-trap fluorescence measurements," Opt. Express **24**, 8132–8141 (2016).

108. Y. Shechtman, L. E. Weiss, A. S. Backer, S. J. Sahl, and W. E. Moerner, "Precise Three-Dimensional Scan-Free Multiple-Particle Tracking over Large Axial Ranges with Tetrapod Point Spread Functions," Nano Lett. **15**, 4194–4199 (2015).

109. B. H. Fong, J. S. Colburn, J. J. Ottusch, J. L. Visher, and D. F. Sievenpiper, "Scalar and Tensor Holographic Artificial Impedance Surfaces," IEEE Trans. Antennas Propag. **58**, 3212–3221 (2010).

110. C. L. Holloway, E. F. Kuester, J. A. Gordon, J. O'Hara, J. Booth, and D. R. Smith, "An Overview of the Theory and Applications of Metasurfaces: The Two-Dimensional Equivalents of Metamaterials," IEEE Antennas Propag. Mag. **54**, 10–35 (2012).

111. A. V. Kildishev, A. Boltasseva, and V. M. Shalaev, "Planar photonics with metasurfaces," Science **339**, 1232009 (2013).

112. S. Jahani and Z. Jacob, "All-dielectric metamaterials," Nat. Nanotechnol. **11**, 23–36 (2016).

113. A. E. Krasnok, A. E. Miroshnichenko, P. A. Belov, and Y. S. Kivshar, "All-dielectric optical nanoantennas," Opt. Express **20**, 20599–20604 (2012).

114. S. Sun, Q. He, S. Xiao, Q. Xu, X. Li, and L. Zhou, "Gradient-index meta-surfaces as a bridge linking propagating waves and surface waves," Nat. Mater. **11**, 426–431 (2012).

115. F. Qin, L. Ding, L. Zhang, F. Monticone, C. C. Chum, J. Deng, S. Mei, Y. Li, J. Teng, M. Hong, S. Zhang, A. Alù, and C.-W. Qiu, "Hybrid bilayer plasmonic metasurface efficiently manipulates visible light," Sci. Adv. **2**, e1501168 (2016).

116. X. Ding, F. Monticone, K. Zhang, L. Zhang, D. Gao, S. N. Burokur, A. de Lustrac, Q. Wu, C.-W. Qiu, and A. Alù, "Ultrathin Pancharatnam–Berry Metasurface with Maximal Cross-Polarization Efficiency," Adv. Mater. **27**, 1195–1200 (2015).

117. N. Yu, F. Aieta, P. Genevet, M. A. Kats, Z. Gaburro, and F. Capasso, "A Broadband, Background-Free Quarter-Wave Plate Based on Plasmonic Metasurfaces," Nano Lett. **12**, 6328–6333 (2012).

118. M. Pu, X. Li, X. Ma, Y. Wang, Z. Zhao, C. Wang, C. Hu, P. Gao, C. Huang, H. Ren, X. Li, F. Qin, J. Yang, M. Gu, M. Hong, and X. Luo, "Catenary optics for achromatic generation of perfect optical angular momentum," Sci. Adv. **1**, e1500396 (2015).

119. R. C. Devlin, A. Ambrosio, D. Wintz, S. L. Oscurato, A. Y. Zhu, M. Khorasaninejad, J. Oh, P. Maddalena, and F. Capasso, "Spin-to-orbital angular momentum conversion in dielectric metasurfaces," Opt. Express **25**, 377–393 (2017).

120. E. Maguid, M. Yannai, A. Faerman, I. Yulevich, V. Kleiner, and E. Hasman, "Disorder-induced optical transition from spin Hall to random Rashba effect," Science **358**, 1411–1415 (2017).

121. N. Kundtz and D. R. Smith, "Extreme-angle broadband metamaterial lens," Nat. Mater. **9**, 129–132 (2010).

122. B. Memarzadeh and H. Mosallaei, "Array of planar plasmonic scatterers functioning as light concentrator," Opt. Lett. **36**, 2569–2571 (2011).

123. X. Ni, S. Ishii, A. V. Kildishev, and V. M. Shalaev, "Ultra-thin, planar, Babinet-inverted plasmonic metalenses," Light Sci. Appl. **2**, lsa201328 (2013).

124. W. X. Jiang, C.-W. Qiu, T. C. Han, Q. Cheng, H. F. Ma, S. Zhang, and T. J. Cui, "Broadband All-Dielectric Magnifying Lens for Far-Field High-Resolution Imaging," Adv. Mater. **25**, 6963–6968 (2013).

125. S. W. Kim, K. J. Yee, M. Abashin, L. Pang, and Y. Fainman, "Composite dielectric metasurfaces for phase control of vector field," Opt. Lett. **40**, 2453–2456 (2015).

126. A. Arbabi, R. M. Briggs, Y. Horie, M. Bagheri, and A. Faraon, "Efficient dielectric metasurface collimating lenses for mid-infrared quantum cascade lasers," Opt. Express **23**, 33310–33317 (2015).

127. A. Zhan, S. Colburn, R. Trivedi, T. K. Fryett, C. M. Dodson, and A. Majumdar, "Low-Contrast Dielectric Metasurface Optics," ACS Photonics **3**, 209–214 (2016).

128. A. Arbabi, E. Arbabi, S. M. Kamali, Y. Horie, S. Han, and A. Faraon, "Miniature optical planar camera based on a wide-angle metasurface doublet corrected for monochromatic aberrations," Nat. Commun. **7**, 13682 (2016).

129. B. Groever, W. T. Chen, and F. Capasso, "Meta-Lens Doublet in the Visible Region," Nano Lett. **17**, 4902–4907 (2017).

130. F. Aieta, M. A. Kats, P. Genevet, and F. Capasso, "Multiwavelength achromatic metasurfaces by dispersive phase compensation," Science **347**, 1342–1345 (2015).

131. E. Arbabi, A. Arbabi, S. M. Kamali, Y. Horie, and A. Faraon, "Multiwavelength polarization-insensitive lenses based on dielectric metasurfaces with meta-molecules," Optica **3**, 628–633 (2016).

132. Z. Zhao, M. Pu, H. Gao, J. Jin, X. Li, X. Ma, Y. Wang, P. Gao, and X. Luo, "Multispectral optical metasurfaces enabled by achromatic phase transition," Sci. Rep. **5**, srep15781 (2015).
133. O. Avayu, E. Almeida, Y. Prior, and T. Ellenbogen, "Composite functional metasurfaces for multispectral achromatic optics," Nat. Commun. **8**, 14992 (2017).

134. M. Khorasaninejad, Z. Shi, A. Y. Zhu, W. T. Chen, V. Sanjeev, A. Zaidi, and F. Capasso, "Achromatic Metalens over 60 nm Bandwidth in the Visible and Metalens with Reverse Chromatic Dispersion," Nano Lett. **17**, 1819–1824 (2017).

135. E. Arbabi, A. Arbabi, S. M. Kamali, Y. Horie, and A. Faraon, "Controlling the sign of chromatic dispersion in diffractive optics with dielectric metasurfaces," Optica **4**, 625–632 (2017).

136. S. Wang, P. C. Wu, V.-C. Su, Y.-C. Lai, C. H. Chu, J.-W. Chen, S.-H. Lu, J. Chen, B. Xu, C.-H. Kuan, T. Li, S. Zhu, and D. P. Tsai, "Broadband achromatic optical metasurface devices," Nat. Commun. **8**, 187 (2017).

137. S. Wang, P. C. Wu, V.-C. Su, Y.-C. Lai, M.-K. Chen, H. Y. Kuo, B. H. Chen, Y. H. Chen, T.-T. Huang, J.-H. Wang, R.-M. Lin, C.-H. Kuan, T. Li, Z. Wang, S. Zhu, and D. P. Tsai, "A broadband achromatic metalens in the visible," Nat. Nanotechnol. **13**, 227–232 (2018).

138. W. T. Chen, A. Y. Zhu, V. Sanjeev, M. Khorasaninejad, Z. Shi, E. Lee, and F. Capasso, "A broadband achromatic metalens for focusing and imaging in the visible," Nat. Nanotechnol. **13**, 220–226 (2018).

139. S. Shrestha, A. Overvig, and N. Yu, "Broadband achromatic metasurface lenses," in *2017 Conference on Lasers and Electro-Optics (CLEO)* (2017), pp. 1–2.

140. M. Born and E. Wolf, *Principles of Optics: Electromagnetic Theory of Propagation, Interference and Diffraction of Light* (Cambridge University, 1999).

141. J. D. Joannopoulos, S. G. Johnson, J. N. Winn, and R. D. Meade, *Photonic Crystals*, Second (2008).

142. M. Principe, M. Consales, A. Micco, A. Crescitelli, G. Castaldi, E. Esposito, V. La Ferrara, A. Cutolo, V. Galdi, and A. Cusano, "Optical fiber meta-tips," Light Sci. Appl. **6**, e16226 (2017).

143. L. Li, I. Bayn, M. Lu, C.-Y. Nam, T. Schröder, A. Stein, N. C. Harris, and D. Englund, "Nanofabrication on unconventional substrates using transferred hard masks," Sci. Rep. **5**, 7802 (2015).

144. Z. Huang, N. Geyer, P. Werner, J. de Boor, and U. Gösele, "Metal-Assisted Chemical Etching of Silicon: A Review," Adv. Mater. **23**, 285–308 (2011).

145. Easton, Roger, "Optics of Imaging Systems-Course Notes for 1051-733," (2012).

146. "Comparison of Optical Aberrations | Edmund Optics," https://www.edmundoptics.com/resources/application-notes/optics/comparison-of-optical-aberrations/.

147. F. A. Vera-Díaz and N. Doble, "The Human Eye and Adaptive Optics," Top. Adapt. Opt. (2012).

148. P. Genevet, F. Capasso, F. Aieta, M. Khorasaninejad, and R. Devlin, "Recent advances in planar optics: from plasmonic to dielectric metasurfaces," Optica **4**, 139–152 (2017).

149. L. Wang, S. Kruk, H. Tang, T. Li, I. Kravchenko, D. N. Neshev, and Y. S. Kivshar, "Grayscale transparent metasurface holograms," Optica **3**, 1504–1505 (2016).

150. S. M. Kamali, E. Arbabi, A. Arbabi, and A. Faraon, "A review of dielectric optical metasurfaces for wavefront control," Nanophotonics **7**, 1041–1068 (2018).

151. F. Yesilkoy, E. R. Arvelo, Y. Jahani, M. Liu, A. Tittl, V. Cevher, Y. Kivshar, and H. Altug, "Ultrasensitive hyperspectral imaging and biodetection enabled by dielectric metasurfaces," Nat. Photonics **13**, 390–396 (2019).

152. A. Arbabi, E. Arbabi, Y. Horie, S. M. Kamali, and A. Faraon, "Planar metasurface retroreflector," Nat. Photonics **11**, 415–420 (2017).

153. N. A. Rubin, G. D'Aversa, P. Chevalier, Z. Shi, W. T. Chen, and F. Capasso, "Matrix Fourier optics enables a compact full-Stokes polarization camera," Science **365**, eaax1839 (2019).

154. G.-Y. Lee, J.-Y. Hong, S. Hwang, S. Moon, H. Kang, S. Jeon, H. Kim, J.-H. Jeong, and B. Lee, "Metasurface eyepiece for augmented reality," Nat. Commun. **9**, (2018).

155. A. Y. Zhu, W. T. Chen, J. Sisler, K. M. A. Yousef, E. Lee, Y.-W. Huang, C.-W. Qiu, and F. Capasso, "Compact Aberration-Corrected Spectrometers in the Visible Using Dispersion-Tailored Metasurfaces," Adv. Opt. Mater. **7**, 1801144 (2019).

156. R. J. Lin, V.-C. Su, S. Wang, M. K. Chen, T. L. Chung, Y. H. Chen, H. Y. Kuo, J.-W. Chen, J. Chen, Y.-T. Huang, J.-H. Wang, C. H. Chu, P. C. Wu, T. Li, Z. Wang, S. Zhu, and D. P. Tsai, "Achromatic metalens array for full-colour light-field imaging," Nat. Nanotechnol. **14**, 227–231 (2019).

157. P. Hartmann, *Optical Glass* (SPIE Press, 2014).

158. T. Stone and N. George, "Hybrid diffractive-refractive lenses and achromats," Appl. Opt. **27**, 2960–2971 (1988).

159. W. T. Chen, A. Y. Zhu, J. Sisler, Y.-W. Huang, K. M. A. Yousef, E. Lee, C.-W. Qiu, and F. Capasso, "Broadband Achromatic Metasurface-Refractive Optics," Nano Lett. **18**, 7801–7808 (2018).

160. S. Shrestha, A. C. Overvig, M. Lu, A. Stein, and N. Yu, "Broadband achromatic dielectric metalenses," Light Sci. Appl. **7**, 1–11 (2018).

161. E. Arbabi, A. Arbabi, S. M. Kamali, Y. Horie, M. Faraji-Dana, and A. Faraon, "MEMS-tunable dielectric metasurface lens," Nat. Commun. **9**, 1–9 (2018).

162. Y. Zhou, I. I. Kravchenko, H. Wang, J. R. Nolen, G. Gu, and J. Valentine, "Multilayer Noninteracting Dielectric Metasurfaces for Multiwavelength Metaoptics," Nano Lett. **18**, 7529–7537 (2018).

163. D. Sell, J. Yang, S. Doshay, and J. A. Fan, "Periodic Dielectric Metasurfaces with High-Efficiency, Multiwavelength Functionalities," Adv. Opt. Mater. **5**, 1700645 (2017).

164. D. Sell, J. Yang, S. Doshay, R. Yang, and J. A. Fan, "Large-Angle, Multifunctional Metagratings Based on Freeform Multimode Geometries," Nano Lett. **17**, 3752–3757 (2017).

165. S. Molesky, Z. Lin, A. Y. Piggott, W. Jin, J. Vucković, and A. W. Rodriguez, "Inverse design in nanophotonics," Nat. Photonics **12**, 659–670 (2018).

166. A. D. Rakić and M. L. Majewski, "Modeling the optical dielectric function of GaAs and AlAs: Extension of Adachi's model," J. Appl. Phys. **80**, 5909–5914 (1996).

167. L. Zhang, J. Ding, H. Zheng, S. An, H. Lin, B. Zheng, Q. Du, G. Yin, J. Michon, Y. Zhang, Z. Fang, M. Y. Shalaginov, L. Deng, T. Gu, H. Zhang, and J. Hu, "Ultra-thin high-efficiency mid-infrared transmissive Huygens meta-optics," Nat. Commun. **9**, 1–9 (2018).

168. Y.-W. Huang, H. W. H. Lee, R. Sokhoyan, R. A. Pala, K. Thyagarajan, S. Han, D. P. Tsai, and H. A. Atwater, "Gate-Tunable Conducting Oxide Metasurfaces," Nano Lett. **16**, 5319–5325 (2016).

169. A. Forouzmand, M. M. Salary, S. G. Kafaie, R. Sokhoyan, H. A. Atwater, and H. Mosallaei, "Tunable all-dielectric metasurface for phase modulation of the reflected and transmitted light via permittivity tuning of indium tin oxide," Nanophotonics **8**, 415–427 (2019).

Appendix

Published Content and Contribution

- **Sajan Shrestha,** Adam C. Overvig, Ming Lu, Aaron Stein, and Nanfang Yu. "*Broadband achromatic dielectric metalenses*." Light: Science and Applications, Vol 7, no. 85 (2018). [link]
- **Sajan Shrestha**, Yu Wang, Adam C. Overvig, Ming Lu, Aaron Stein, Luca Dal Negro, and Nanfang Yu. "*Indium tin oxide broadband metasurface absorber*." ACS Photonics, Vol 5, no. 9 (2018). [link]
- Adam C. Overvig, **Sajan Shrestha**, Stephanie C. Malek, Ming Lu, Aaron Stein, and Nanfang Yu. "*Dielectric metasurfaces for complete and independent control of optical amplitude and phase*". [link]
- **Sajan Shrestha,** Adam C. Overvig, Ming Lu, Aaron Stein, and Nanfang Yu. "*Multi-element metasurface system for imaging in the near-infrared*". (Manuscript in preparation)
- **Sajan Shrestha,** Adam C. Overvig, Stephanie C. Malek, and Nanfang Yu. "*Multi-color amplitude and phase metasurface doublet hologram*". (Manuscript in preparation)
- Adam C. Overvig, Stephanie C. Malek, Michael J. Carter, **Sajan Shrestha**, and Nanfang Yu. "*Selection rules for symmetry-protected bound states in the continuum*". [link]
- Adam C. Overvig, **Sajan Shrestha,** and Nanfang Yu. "*Dimerized high contrast gratings*." Nanophotonics, Vol. 7, no. 6 (2018). [link]
- Zhaoyi Li, Myoung-Hwan Kim, Cheng Wang, Zhaohong Han, **Sajan Shrestha**, Adam C. Overvig, Ming Lu, Aaron Stein, Aunradha Agarwal, Marko Loncar, and Nanfang Yu. "*Controlling propagation and coupling of waveguide modes using phase-gradient metasurfaces*." Nature Nanotechnology, Vol. 12, no. 7 (2017). [link]
- Zhenda Xie, Tian Zhong, **Sajan Shrestha**, XinAn Xu, Junlin Liang, Yan-Xiao Gong, Joshua C. Bienfang, Alessandro Restelli, Jeffrey H. Shapiro, Franco N. C. Wong and Chee Wei Wong, "*Harnessing high-dimensional hyperentanglement through a biphoton frequency comb*", Nature Photonics,Vol. 9, 536 (2015). [link]
- Yu Wang, Adam C. Overvig, **Sajan Shrestha**, Ran Zhang, Ren Wang, Nanfang Yu, and Luca Dal Negro, "*Tunability of indium tin oxide materials for mid-infrared plasmonics applications*",Optics Material Express, Vol. 7,8 (2017). [link]
- Wesley A. Britton, Ran Zhang, Sajan Shrestha, Yuyao Chen, Nanfang Yu, and Luca Dal Negro, "Indium silicon oxide thin films for infrared metaphotonics",Applied Physics Letters, 114, 161105 (2019). [link]